Ultrafast carrier and structural dynamics in graphite detected via attosecond soft X-ray absorption spectroscopy

Nicola Di Palo

February 21, 2020

...A Mamma e Papà,
Perchè, senza saperne quasi nulla,
Ci hanno sempre creduto più di tutti!

Abstract

Understanding most of the physical and chemical phenomena determining the world around us requires the possibility to interrogate their main characters on their natural scale in space and time. The insulating or conductive behavior of matter, its magnetic properties or the nature of chemical bonds are dependent by the nuclear and electronic structure of the atoms, molecules or solids considered. Hence, tools are needed to probe electrons and nuclei directly at the atomic scale with a temporal resolution allowing the observation of electron dynamics (on the attosecond-to-femtosecond timescale) and structural dynamics (on the femtosecond-to-picosecond timescale) in real-time.

Attosecond science offers unique opportunities to investigate electronic and structural dynamics at the heart of important processes in atomic, molecular and solid-state physics. The generation of attosecond bursts of light, in the form of trains of pulses or isolated pulses, has been achieved on table-top sources by exploiting the high-order harmonic generation (HHG) process. The photons constituting the attosecond emission have energies that range from the extreme ultra-violet (XUV) up to the soft X-ray (SXR) region of the spectrum, allowing to interrogate the electronic structure of the probed material directly at the level of the inner electronic shells. Because of this property of accessing the characteristic electronic structure of the elements constituting the target, XUV and, especially, SXR spectroscopy are considered element-specific techniques. Attosecond pulses have already proven to be able to observe ultrafast phenomena in atoms, molecules or solids previously inaccessible.

In this thesis, the application of time-resolved X-ray absorption fine-structure (XAFS) spectroscopy using attosecond SXR pulses to the study of carrier and structural dynamics in graphite is reported. In Chap. 1, an introduction to the field of attoscience and the presentation of the state of the art of ultrafast dy-

namics in graphite are given. The established technique to generate attosecond pulses is described and a review of the most significant application of attosecond pulses to the study of electron dynamics is presented. The electronic and structural properties of graphite are then discussed, highlighting some of the most representative experiments detecting electron and lattice dynamics.

The experimental setup developed at ICFO in the group of Prof. Dr. Jens Biegert and used for this Ph.D. thesis project is described in detail in Chap. 2. The system needed for the generation, propagation, and detection of the attosecond SXR radiation is presented. The performances of the SXR source in terms of spectral tunability, photon flux and stability are discussed. The implementation of an IR pump - SXR probe scheme is reported, allowing beams' recombination in both collinear and non-collinear fashion. To conclude, the results of an attosecond streaking experiment are presented, through which a temporal characterization of the HHG emission has been achieved.

A discussion on the spectroscopic capabilities of XAFS technique to interrogate the electronic and lattice structure of the observed material is presented in Chap. 3. The potential of this technique has been demonstrated with an experimental investigation of a graphite thin film, with the results showing the possibility to probe the first unoccupied electronic bands and the characteristic distances defining the lattice structure.

Finally, the XAFS capabilities have been exploited in a time-resolved experimental study of graphite to observe light-induced carrier and lattice dynamics, presented in Chap. 4. The interpretation of the experimental data reveals insights on the ultrafast interaction of the pump laser field with charge carriers and on the effects of carrier-carrier and carrier-phonon scattering following photoexcitation.

Acknowledgments

If you are now reading this piece of paper, this means that I finally made it. So, the first person that probably deserves a big thank you is simply myself, BRAVO NICOLA! But at the same time, it is important to remember that in this 5-year journey I was never alone and that the help and guidance of several people deserve to be acknowledged.

As a start, I want to sincerely thank my supervisor, Prof. Jens Biegert. The possibility he gave me to join his group has allowed me to work in a unique laboratory where high-quality, cutting-edge research is daily carried out, immersed in a highly-motivating, international environment, which surely helped me a lot in growing up as a researcher, but also as a person. I hope we agree on the fact that, even with lots of difficulties, we finally got very nice results to be proud of, fruit of hard work but also of you always believing in this project.

For the lucky ones who had the chance to see my lab, you easily realized that working there cannot be a one-person job. The team of people who hardly worked to get the results of this thesis is usually called the *Beamline team*, but I rather prefer *HHG gang*! And so, thanks to Seth, Barbara and Iker, who helped me a lot at the beginning in trying to understand how to run such a big machine. Thanks to the people who put a lot of efforts to have the experiments running and producing results: Daniel and the music-dependent laser operations; Themis and the two years or more spent talking about hexagonal structures of carbon atoms from every point of view (hopefully we finally understood something!); Stefano, mio fratello minore (vogl verè comm fai mo...); Maurizio, mio fratello maggiore (potrai sempre chiamare per decidere cosa fare a cena, no worries). And of course, I thank also the last ones who joined the HHG gang, Hung-Wei, Ying-Hao and Adam.

I want to thank the rest of the AUO group too, because I found always important to have an enjoyable atmosphere when coming out of the lab, when going out for afterworks or when drinking Patxaran at the group retreat. So, in a random order, thanks to Julius, Ugaitz, Aurelien, Xinyao, Blanca, Florian, Luke, Ben, Matthias, Daniel, Idoia, Noslen, Michael, Christian, Joana, Tiago, Gonçalo, Hugo, Tsuneto, Mick, Michele (alla fine è tutta colpa/merito tuo!), Lenard, Biplob, Antonio, Tobias, Kasra, Moni, Irina, Sergio.

And, besides the people from my group, here at ICFO I had the possibility to meet a lot of crazy, funny, interesting faces who made this journey simply better. A very big grazie to I Uagliuttoni: Alessandro, anche se na volta eri più amico ma io tvb sempre; Sergione, perchè dopo tanti icfobbus, caffettini e lamentele pure ce l'abbiamo fatta; grazie ai Marchi (Manzoni e Pagliazzi), a Ivan e a Emanuele. And then, in random order, thanks to Martina, Stefano Duranti e Grava, Emilio, Angelo, Nello, Nadine, Carlotta, Iñigo, Iacopo, Cesar, Auxi, Andrea, Peppe, Alex (Elbelga), Nicola, Alex, Stella, Bernardo, Maria. ICFO is a very nice place also because of all the people helping/working for you: I am very thankful to all the workshops, Carlos, Lluis and Nuria, el Cafè de la Llum, the Frontdesk, the HR office.

Llevar a cabo un doctorado no es facil, sobretodo si al salir del curro no hay posibilidades de estar bien y desconectar. Esto para mi ha sido siempre posible gracias a tod@s l@s amig@s que han estado a mi lado, a la familia que he elegido para estos años. Muchas gracias a Emanuele (dai giochi, alla musica, alla politica), Sareta (mi primera amiguita española), Nicolò (potevamo giocare di più a basket!), Belen (para la compañia y hospitalidad), Giorgio (grazie per la stanza, da lì tutto in discesa), Michela (grazie per l'energia), Michele (e le tante stimolanti discussioni), Maurizia (e lo stile), Isa (ciao sorellì), Giovanna (e la freschezza), Natalia (e la dolcezza e tranquillità), Lorenzo (e le birrette), Margherita (keep on dancin'), Gerardo (quando mi insegni Ableton?), Stefano (e i carichi a briscola non giocati), Serena (tante cose, ma quei dolci...), Vincenzo (anche se poi scompari, tvb), Francesco (keep on rockin'), Roberta (e il balletto della sfera), Gianvito (keep on drummin'), Stefania (bentornata a Barcellona, peccato che ora me ne vado io), Fabio (e la sana invidia per i tuoi viaggi/progetti), Miriana (nessuno gioca meglio di noi), Caterina (perchè ridi sempre e ridere fa bene).

Muchas gracias a l@s compañer@s de piso que me han aguantado estos 5 años, viendome salir y volver a cualquier hora y con mil diferentes humores.

Muchas gracias a Michela, Fabio, Olga (y nuestras cenas de queso y vino), Fulvia, Enriqueta, Bernardo y Ramon (nuestro profe de historia favorito). El piset de Rector Triadò ha siempre sido y serà un lugar bonito donde volver y encontrarse a gusto gracias a vosotr@s.

Si Barcelona me ha entrado tanto en el corazón, se debe tambien a las personas de aquì que he tenido la suerte de conocer. Muchisimas gracias a todas las Cultus y a los Barriaders, para todas las actividades y el tiempo de calidad pasado juntos.

Grazie alla grande famiglia di amici che ho a Mondragone. Anche se potevate venire a trovarmi molto di più, poter tornare a casa e rivedervi tutti, sempre, fa bene al cuore.

Grazie ai Poissoniani, perchè 'sta cazzata di fa Fisica ce l'abbiamo in comune, e perchè siete e sarete sempre là.

Grazie a tutta la mia famiglia, quella vera, e in particolare ad Antonia, mamma e papà, perchè sono sempre stati i miei primi sostenitori.

Y, en fin, muchisimas gracias a Marta, compañera de vida y fuente inagotable de curiosidad, alegria y amor. Tener la suerte de tenerte al lado en estos años me ha facilitado y alegrado la vida, constituyendo un gran apoyo siempre presente. Te espero en Milan, para seguir con el totambtu.

Contents

Chapter 1

Introduction

This introductory chapter contains an overview of the two different fields that the work presented in this thesis aims at bridging: the generation and application of attosecond X-ray pulses to the study of electron and structural dynamics in graphite. The chapter is divided into two parts, each describing one of these two research areas. First, the field of attoscience is presented, describing the scientific and technological revolution that started after the observation of the first generation of attosecond pulses. The general approach employed for the generation of such short pulses is discussed and a summary of the most significant results achieved by the application of attosecond pulses to time-resolved studies of ultrafast dynamics is reported. The second half focuses instead on the state of the art of the electronic and structural dynamics observed in graphite. The fascinating properties of this material are presented and the most important time-resolved studies of light-induced dynamics involving both the electron and the lattice system are discussed.

1.1 Attoscience

The development of light sources capable to deliver laser pulses of femtosecond (fs) duration opened the way to the widespread use of time-resolved experimental techniques to study the evolution of physical and chemical phenomena in nature. The resulting advances are elegantly summarized in a review article by Zewail [1], describing in detail how the possibility to unravel fundamental chemical and physical processes is related to the development of experimental techniques able to probe them on their natural timescale. Femtosecond-resolved methods have proven already to be able to monitor rotational and vibrational properties of molecular and solid-state targets, following in real-time processes like bond breaking and formation, passage through conical intersections or phonon excitation in crystals. These experimental techniques are in continuous evolution and have become a standard feature of any physics or chemistry lab aimed to study structural dynamics.

The electronic and lattice configurations of the material are responsible for the shape of the potential energy ruling both the electronic and atomic motion: changes in this configuration induced by electron dynamics will affect the structural properties of the molecule or the crystal under observation. While fs-resolved experiments can follow the electron-induced structural dynamics, catching the electron motion in real-time requires the use of experimental techniques with higher temporal resolution. Electron motion can take place on a sub-fs timescale: as an example, in a classical picture, the time needed for an electron to orbit around the hydrogen atom is 150 attoseconds (as). For visible or infrared (IR) light sources, the ultimate limit for pulse compression resides in the optical cycle duration of the central wavelength of the laser, which ranges in the few-fs regime for visible light (at 800 nm it corresponds to 2.6 fs). Even if visible laser pulses carrying electric field with sub-fs structure have been synthesized [2], lasers working at higher frequencies extending in the extreme ultra-violet (XUV)/ X-ray regime are needed to realize sub-fs pulses.

The possibility to engineer laser sources delivering high-intensity pulses thanks to the chirped-pulse amplification (CPA) technique (for which Donna Strickland and Gerard Mourou received the Nobel Prize in 2018 [3]) allowed to study light-matter interaction at previously unreachable intensity values (in the range of $10^{13} - 10^{14}\,\mathrm{W/cm^2}$). By focusing such intense laser pulses on noble gas targets, the first observation of harmonics of the laser frequency of very high order was observed for the first time in the late 1980s, reaching the UV-XUV region (the maximum photon energy of $\sim 80\,\mathrm{eV}$ was detected) [4, 5]. Since then, this frequency up-conversion non-linear process today known as High-order Harmonic Generation (HHG) has been intensively studied from both a theoretical and experimental point of view in the 1990s and brought to the demonstration of the emission of the first light pulses of attosecond pulse duration in 2001 [6, 7].

These breakthroughs launched a new research field called Attoscience which reached incredible results in the generation of ultrashort bursts of light of attosecond duration and their application to the study of electron dynamics in the matter, as resumed in many review articles [8, 9, 10, 11, 12]. The process of HHG is presented in Sec. 1.1.1, discussing how it can generate pulses of attosecond duration ranging in the XUV - X-ray energy range. The most important results obtained with the application of attosecond pulses to resolved electron dynamics are reported in Sec. 1.1.2, with particular attention to the experiments conducted on solid-state materials.

1.1.1 High Harmonic Generation

The high harmonic generation process is a complex nonlinear phenomenon which is the object of research studies even after several decades after its discovery. In a nutshell, the process consists of the highly nonperturbative interaction of a high-intensity laser pulse, usually ranging in the IR photon energy region, with a target material, typically an inert gas contained in a gas cell or waveguide or streaming out of a gas jet. The strong-field interaction originating the HHG process is elegantly interpreted in terms of the semi-classical treatment known as the 3-step model [13, 14], represented in Fig. 1.1. In the first step, the high field amplitude occurring in the proximity of each field crest of the linearly-polarized laser driver distorts the potential barrier seen by the electron, resulting in a tunneling ionization event that releases an electron wave-packet in the continuum. In these conditions, the electric field exerts a force on the ejected electron, which is accelerated away from its parent ion along the field polarization direction until the field changes in sign, accelerating the electron back towards the originating ion (step 2). Finally, in the third step, the returning electron recombines with its parent ion with the subsequent release of the excess kinetic energy acquired with the field acceleration as light bursts with photon energy in the XUV - X-ray region and same linear polarization of the laser driver. The highly nonlinear dependence of the instant of initial ionization event on the electric field of the laser driver confines the electron ejection to short time intervals near the maximum of the optical cycle. The result of this temporal confinement is that XUV/SXR photons are produced in short bursts with a duration that is a small fraction of the optical cycle of the driver laser.

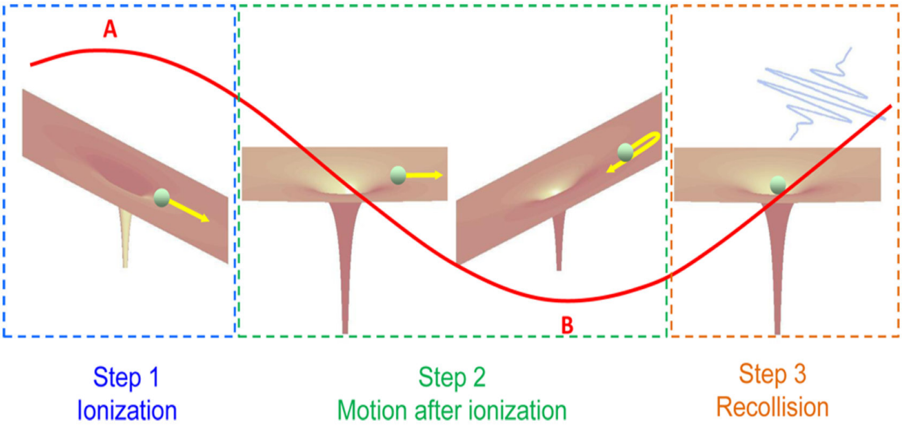

Figure 1.1: Schematics of the three-step model for HHG. In step 1, electrons are emitted through tunnel ionization occurring in the proximity of a field crest (for example, at the A point). The driving field accelerates the free electrons away and then back towards their parent ions (step 2), where recombination is possible leading to the emission of attosecond bursts of XUV-SXR photons (step3, around the B point). Reprinted with permission from [15]. Copyright (2017) American Chemical Society.

Ponderomotive scaling of HHG process

The upper limit to the frequency that can be generated via HHG process in gases (called cutoff energy) is determined by the amount of kinetic energy acquired by the electron in the second step, hence related to the laser driver parameters. An expression for the cutoff energy can be derived analytically from the quantum-mechanical model of HHG [16], in agreement with several experimental observations:

$$E_{cutoff} = IP + 3.17\,U_P \tag{1.1}$$

where IP is the ionization potential of the gas and U_P is the ponderomotive energy of the ejected electrons under the electric field force, described (in atomic units) by $U_P = I_L/4\omega_L^2$, where I_L and ω_L are respectively the intensity and the central frequency of the driving laser. Typical intensities to achieve HHG are on the order of $10^{13} - 10^{14}\,\mathrm{W/cm^2}$, which for the case of 800 nm laser results in cutoff energies of $\sim 30\,\mathrm{eV}$ in Xenon or $\sim 100 - 150\,\mathrm{eV}$ in Neon. Further increasing the laser intensity to extend the cutoff energy can unfavorably affect the phase-matching process (deeply described in the work of Balcou and coauthors [17, 18]) and reduce the recombination probability due to the excursion experienced by the electrons in the strong electric field. Hence, the strategy to extend the HHG spectrum to the SXR region is to drive the process with laser drivers working at longer wavelengths.

The recent developments in the realization of intense and tunable ultrafast sources operating in the short-wavelength IR (SWIR, $0.9 - 2.5\,\mu$m) spectral region opened the way to the investigation of HHG process beyond the popular 800 nm case. After the first demonstration of the cutoff energy extension reported by Shan et al. [19], many groups have exploited SWIR sources to produce HHG extending to the SXR region [20]. However, the scaling of the HHG cutoff energy for SWIR drivers has always been accompanied by the unfavorable scaling of the efficiency of the HHG process. For these wavelengths, the flight time of the electron before recombination is longer, resulting in a larger spatial spread of the electron wavepacket hence lowering the recombination probability and lower HHG flux (a theoretical investigation of the wavelength scaling of the HHG efficiency is found in [21, 22]). On the other hand, the energy dispersion of the HHG emission in time (induced by the property that different electron flight times correspond to different kinetic energies) is also expected to vary with the driver wavelength. This quantity is called attochirp and theoretical calculations [23] and experimental observations [24] report a λ^{-1} scaling, suggesting that SWIR-driven HHG can generate shorter attosecond pulses respect to the 800 nm case.

A general breakthrough overcoming the unfavorable phase-matching was demonstrated by the pioneering work of my group using a sub-2-cycle, $1.85\,\mu$m laser driver, reporting the generation of SXR radiation up to the oxygen K-edge (543 eV) [25, 26, 27]. The low HHG flux obtained for laser drivers at these wavelengths was overcome by achieving phase-matching at very high pressures of gas for the generation [27] (the setup used for HHG and the spectral characterization of its emission are reported in Sec. 2.2, 2.2.1 and 2.2.2). Following this work, several demonstrations of SXR radiation generated via HHG with SWIR laser drivers have been reported [28, 29, 30, 31]. A further extension of the cutoff energy above the oxygen K-edge has been reported by Popmintchev et al., obtained by focusing $3.9\,\mu$m laser pulses in a hollow-core fiber (HCF) filled with high pressure of Helium, producing HHG emission up to 1.6 keV [32], however producing a lower flux with respect to the above-mentioned cases.

Attosecond pulse train vs Isolated attosecond pulse

The HHG process is initiated for each half-cycle of the electric field resulting in a field amplitude able to trigger the tunneling ionization step. As a consequence, multiple HHG emissions can be obtained with a single pulse of the laser driver, usually referred to as an attosecond pulse train (APT), with two consecutive emissions separated by half the optical cycle of the laser driver. The interference between the different pulses contained in the APT generates the characteristic spectrum of the HHG emission, consisting of a discrete series of peaks positioned at odd multiples of the frequency of the driving laser until the cutoff region, a continuum spectrum corresponding to the contribution of the most intense half-cycle. APTs have been employed in several interferometry experiments to study electron dynamics [33, 34], but offer a limited amount of applications for pump-probe investigations, where generally the system is investigated with a pair of individual pulses.

The general approach to generate an isolated attosecond pulse (IAP) is to isolate one single emission event per each laser shot from the HHG process. This can be achieved by applying a gate to the process in either the spectral or temporal domain. In the amplitude gating scheme, by means of reflective/transmissive optics, the continuum produced in the cutoff region of a stable HHG spectrum can be isolated, resulting in the isolated emission of the most intense half-cycle [7, 35]. For an efficient application, it requires nearly-single-cycle laser drivers with good CEP stability and the use of proper XUV-SXR optics, which are not always available. In the temporal gating, the drop in HHG efficiency occurring for nonlinear laser driver polarization (electron trajectories follow the ellipticity of the electric field, reducing the recombination probability) is used to obtain HHG emission by a single half-cycle. Examples of this approach are the polarization gating [36, 37, 38] or double-optical gating techniques [39], which differ in the way the generating laser field is engineered (the combination of two circularly-polarized fields with controllable delay).

Another approach implying a gate in the time domain is the so-called ionization gating scheme. Here, by means of a few-cycle, high-intensity laser driver, a nearly-total ionization of the generating medium can be achieved within the leading edge of the driving pulse, with possible confinement to a single half-cycle. The intensity is such that the phase-matching conditions for the HHG process are varying in time over the duration of the laser driver pulse. While this scheme has been discussed and demonstrated in several applications for isolated XUV pulse generation [40, 41], the extension of this scheme to the SXR range was investigated for the first time by our group in the work of Teichmann et al. [27]. The higher gas pressure values needed for long-wavelength-driven HHG required the study of phase-matching conditions for this new regime.

Using the expressions for the phase-matching of the HHG process defined in [18], Teichmann and coauthors calculated numerically the dependence of the phase-mismatch for generating HHG in Helium and Neon at different photon energy in space and time, as a function of time (within the pulse duration) and space (around the focal plane). An example is reported in figure 1.2, where the case of HHG in Helium generating 500 eV radiation is considered. The colormap defines the on-axis phase-mismatch, while the black circle defines the time-space region where pulse intensity is enough to generate 500 eV radiation according to the cutoff law. Results show how the temporal window for good phase-matching becomes narrower for increasing pressure, achieving confinement to a single half-cycle for pressures above 4 bar. Similar results have been obtained for photon energies down to 300 eV and for Neon as generating medium, supporting the existence of a very narrow temporal window providing the condition for the emission of a single attosecond burst of soft X-ray radiation, corresponding to a broadband SXR continuum. The setup to perform HHG in these conditions is widely described in 2.2, 2.2.2, while more details regarding the numerical simulations can be found in [27].

Other strategies to generate IAP are the attosecond lighthouse technique and the two-color field HHG. In the attosecond lighthouse, firstly proposed by Vincenti and Quéré [42], the spatio-temporal coupling occurring in ultrashort laser pulses is exploited to separate different HHG emissions. In particular, if the laser driver is affected by a pulse-front tilt introduced by a dispersive optics at an angle, each attosecond pulse in the train is emitted along a slightly different direction corresponding to the instantaneous direction of propagation of the driving field at the instant of emission. Then, spatial filtering in the far-field allows the isolation of single attosecond pulses [43], like in the work reported by Silva et al. from our group [26]. The idea behind using a two-color field for HHG is to manipulate electron trajectories by superposition of electric fields at different wavelengths. By combining an 800 nm driver with its second-harmonic [44] or a SWIR component, both in the few-cycle [45] or multi-cycle regime[46].

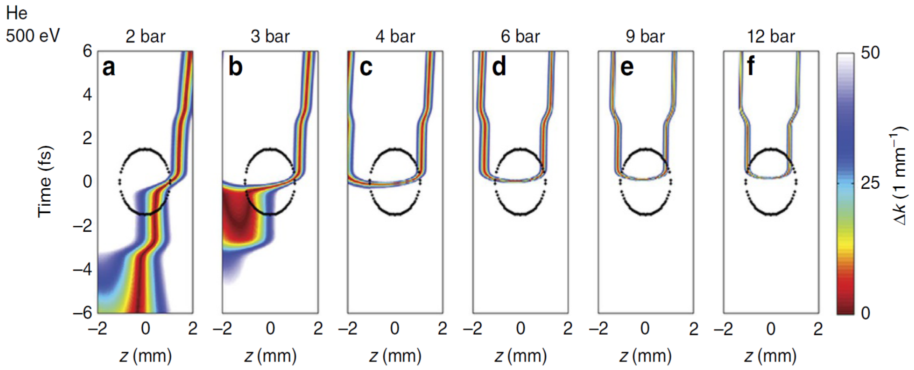

Figure 1.2: Calculated on-axis phase mismatch as a function of propagation position and time within the pulse for 500 eV radiation generated in helium. Laser parameters are: 12 fs of pulse duration, 54 μm of beam waist, 0.5 PW/cm^2 of laser intensity. Dark red indicates good phase-matching and the black oval area denotes the z–t space with field strength sufficient to generate 500 eV radiation. Reprinted with permission from [27]. Copyright © 2016, Springer Nature.

Temporal characterization of HHG emission

Standard methods for temporal characterization of visible-IR optical pulses rely on the possibility to exploit a non-linear interaction with a crystal (i.e. autocorrelation, frequency-resolved optical gating (FROG)). Hence, extending these techniques to the XUV-SXR range requires pulse energies able to produce measurable non-linear signals, making the application of such methods challenging. First, pulse energies obtained with HHG are low (on the order of pJ/nJ) compared to optical laser sources. Second, it is not easy (if not impossible) to find transparent non-linear media for the XUV-SXR photon energy range, which are highly absorbed in any kind of material.

In 2001 two experimental methods have been proposed and demonstrated to temporally characterize the HHG emission: RABBITT (Reconstruction of Attosecond Beating By Interference of Two-photon Transitions) for APTs [6] and Attosecond Streaking for IAPs [7, 47]. The first one is the established method nowadays to characterize in time an APT: the photoelectron distribution produced by ionization of a gas target induced by the APT is dressed by a weak IR field, synchronized in phase and time with the APT. The analysis of the interference pattern produced by the two-photon transitions (XUV-SXR ± IR) on the recorded spectra permits to reconstruct the spectral phase of the APT over the measured photon energy range.

As in the case of RABBITT, the Attosecond Streaking technique used to characterize IAPs also relies on an IR-dressed XUV - SXR photoionization measurement on a gas target, recorded varying the time delay between the two pulses. The photoelectron pulse is assumed to be a replica (shifted in energy by the ionization potential) of the photon pulse, obtained via single-photon absorption. The IR streaking field intensity is higher compared to the RABBITT case (here on the order of $10^{12} - 10^{13}\mathrm{W/cm^2}$) and modulates the kinetic energy spectrum by adding a contribution to the electron momentum proportional to the IR vector potential. The spectrogram obtained recording photoelectron spectra as a function of the delay between IR and XUV - SXR pulses is described by

$$F(\boldsymbol{v},\tau) = \left| \int_{\infty}^{\infty} \boldsymbol{E}_X(t-\tau)\cdot \boldsymbol{d}[\boldsymbol{v}+\boldsymbol{A}_L(t)]\, e^{i\Phi_G(v,t)}\, e^{i(v^2/2+I_P)}\, dt \right|^2 \tag{1.2}$$

where $\boldsymbol{E}_X$ is the electric field of the attosecond pulse; $\boldsymbol{d}(\boldsymbol{v})$ is the dipole transition matrix element from the ground state to the continuum state; $\boldsymbol{A}_L(t)$ is the vector potential of the IR field; $v^2/2$ is the electron kinetic energy in atomic units; I_P is the ionization potential and $\Phi_G(v,t)$ is the quantum phase acquired by the electron during the interaction with the IR field. Mairesse and Quéré [48] suggested interpreting the streaking spectrogram as a FROG trace, meaning as the spectrogram obtained with a FROG measurement, expressed by

$$F(\omega,\tau) = \left| \int_{\infty}^{\infty} E(t-\tau) G(t) e^{i\omega\tau} dt \right|^2 \tag{1.3}$$

where $G(t)$ is the (amplitude or phase) gate function used to measured the complex field $E(t)$. The method introduced by Mairesse and Quéré, called FROGCRAB (FROG for Complete Reconstruction of Attosecond Bursts), includes the approximations needed to justify the analogy between 1.2 and 1.3 (i.e. central-momentum approximation). The streaking trace can be then processed with numerical algorithm solving the phase-retrieval problem (like the principal component generalized projection algorithm (PCGPA)) to reconstruct amplitude and phase of the complex XUV-SXR electric field (firstly demonstrated in [38]) and of the IR streaking field (as demonstrated in [49]). Another possibility to reconstruct the XUV-SXR electric field is offered by the Ptychographic reconstruction method [50], which relaxes some of the constraints needed for

FROGCRAB, resulting in a faster reconstruction. Finally, a streaking characterization method employing weak perturbative IR field has been proposed called PROOF (Phase Retrieval by Omega Oscillation Filtering) [51], suggesting a superior sensitivity for the case of ultra-broadband attosecond pulses.

While Attosecond Streaking is nowadays a well-established technique for IAPs in the XUV regime, the extension to the SXR range requires facing several challenges, resulting in the fact that only a few works can be found in literature at date [28, 52, 53]. The HHG flux can easily be orders of magnitude lower in the SXR range, which together with lower ionization cross-section for this energy region makes the characterization a lengthy process. The IR pulse used for generating SXR is in general longer due to longer wavelengths used for the HHG drivers, requiring to scan a longer delay range in the experiment. What probably is the most challenging condition to fulfill is to find a gas target in which the photoelectron spectrum produced via ionization constitutes a replica of the photon spectrum (i.e. electrons are ionized from mainly one single shell), which can be difficult to satisfy for the ultra-broadband SXR spectra produced with long-wavelength-driven HHG. In section 2.4, our approach to temporally characterize the SXR IAP is described and the results discussed.

1.1.2 Attosecond-resolved ultrafast dynamics

Attosecond pulses resulting from the HHG process represent an ideal tool to follow ultrafast dynamics in real-time. The possibility to induce or probe electron or structural changes with sub-fs resolution is accompanied by the possibility to interrogate the target from the high lying valence electronic states in the XUV region down to core-shell energy level using X-ray photons. Examples of attosecond pump - attosecond probe experiments have only been reported using APTs [54], limited by the low intensity of attosecond pulses achieved with the HHG process. For this reason, pump-probe experiments with an IAP or an APT are performed synchronizing it with a more intense visible-IR few-cycle pulse, usually a replica of the laser pulse driving the HHG process. The temporal resolution of the experiment, given by the cross-correlation between pump and probe pulses, is then limited by the duration of IR pump pulse ($3 - 5\,\text{fs}$) unless the IR pump is a CEP-stable pulse, resulting in a reproducible electric field that can induce fast dynamics on the sub-fs time scale. In this section, an overview of the most significant experiments involving attosecond pulses is presented, with particular attention to transient absorption (TA) measurements on solid-state target for their analogy to the experimental results reported in this dissertation.

The first pump-probe experiment involving a single attosecond pulse has been reported by Drescher et al. [55], where the lifetime of the 3d hole in Krypton created by XUV ionization has been measured. Using the attosecond streaking technique, a lifetime of 7.9 fs is determined, governed by the Auger recombination process following the ionization. Time-resolved charged-particle spectroscopy with attosecond pulses has produced impressive results on the study of electron dynamics on both gas-phase and solid-state targets. Light-induced electron tunneling in Neon atoms has been resolved by capturing multi-electron excitation and relaxation with sub-fs resolution [56]. Electron localization during a dissociation process initiated by XUV molecular photoionization in H_2 and D_2 has been followed with attosecond resolution by analyzing the velocity and angular distribution of the photofragments [57]. A study of IR strong-field ionization of an XUV-ionized phenylalanine molecule allowed to resolved an ultrafast hole migration process, modulating the yield of the immonium dication with 4.3 fs oscillation period [58]. Attosecond delays between electrons coming from different energetic levels have been observed in photoemission from atoms and metal surfaces, employing both IAP [59, 60, 61] and APTs [62, 63, 64].

Another method that has proven to be able to access sub-fs electron dynamics in molecular and solid-state targets is the so-called high harmonic spectroscopy (HHS). This technique, consisting of analyzing the HHG emission to extract information on the generating medium, has been reported the first time by Itatani et al. [65]. By performing HHG measurements in laser-aligned N_2 molecules, the 3D tomographic reconstruction of the highest occupied orbitals contributing to the HHG process is reported. HHS method does not imply the typical pump-probe scheme, but several works have demonstrated how sub-fs electron dynamics can be extracted from these measurements [66, 67]. In the case of a solid-state target, the first observation of HHG has been reported by Ghimire et al. in [68], where harmonics of an IR driver have been measured in a ZnO crystal extending beyond the band edge with a cutoff energy that linearly scales with the laser intensity. Following this first observation, several studies have been published on this topic, nicely reviewed in [69], showing how HHG in solids is related to inter- and intra-band carrier motion taking place on sub-fs timescales. HHS applied to solid-state targets may hold promise to access information on the electronic band structure and to probe driven ultrafast carrier dynamics at petahertz speed (sub-fs timescale).

Finally, TA measurements have been performed with attosecond pulses in the XUV-SXR range to study electron dynamics in many different materials. The typical scheme involves a few-cycle IR pulse initiating dynamics in the target, which are then probed by recording the changes in XUV-SXR absorption. Compared to charged-particle spectroscopy, electronic transitions result in absorption edges at specific photon energies determined by their electronic energy structure, with XUV-SXR photons accessing the inner-shell levels of the target elements. This property makes XUV-SXR absorption an element-specific technique, which allows the unambiguous and simultaneous detection of electronic transitions from different energetic levels or different elements composing the probed material. The X-ray absorption technique and its properties are widely described in Chap. 3.

Attosecond transient absorption in solids

The most interesting results obtained by attosecond-resolved TA experiments in solid-state targets have been nicely reviewed in [70] and can be grouped in two categories: first, the non-linear response of carriers to strong-field pump pulse; second, the material response following pump-induced carrier excitation in the linear regime. Up to date, because of the number of available sources, these applications have been realized using mostly attosecond XUV sources, able to access mainly the M- or L-edges of several solid-state samples. In this section, some of these works are presented and the extension of these applications to attosecond SXR sources is discussed.

In the non-linear interaction regime, the strong electric field of the IR pump pulse directly interacts with the electrons inside the material at the optical-cycle timescale. A comprehensive review of strong-field phenomena due to non-linear interaction of intense laser pulses with electrons in solids has been recently published by Kruchinin et al. [71]. The first investigation of this non-linear interaction has been reported by Schultze et al. [72] in a SiO_2 thin film, pumped with a few-cycle 1.55 eV pulse and probed with an XUV IAP at the $L_{2,3}$ edge (transitions from the 2p states of silicon). The material is dielectric with a 9 eV band-gap, hence no carrier injection from the valence band (VB) to the conduction band (CB) is expected. The experiment shows a strong modulation of the absorption at the $L_{2,3}$ edge oscillating at twice the IR frequency and appearing during the temporal overlap of the two pulses. The effect has been interpreted in terms of Wannier-Stark localization: a strong electric field creates highlylocalized electronic states at lattice sites, leading to a band shift proportional to the field strength, mapped by the modulation of the absorption edge. The oscillations at twice the laser frequency confirm the non-linear nature of the interaction. An experiment carried out with the same setup on pure Si reported a different result [73]. In this case, the 3.2 eV band-gap allows non-linear carrier injection, which signal has been observed at the $L_{2,3}$ edge over $\sim$ 100 fs time range. By zooming into the rise time of the transient signal, a step-like structure synchronized with the IR electric field is revealed, suggesting tunneling ionization as carrier injection mechanism, as already observed in atomic targets [56], and supported by a Keldysh parameter of 0.5.

The IR pump - XUV probe scheme has been then applied to different cases of nonlinear field-carrier interaction, investigating different pump intensity ranges or different classes of materials. Mashiko and coauthors [74] resolved the three-photon absorption mechanism in GaN (3.35 eV band-gap), producing a modulation of the spectrum at three times the pump laser frequency(0.86 fs) and constituting the first observation of petahertz carrier motion in solids. In GaAs, where the band-gap is bridged by absorption of a single photon at 800 nm, Schlaepfer et al. found the injection of carriers in CB to be described by a transient feature spread over the band-gap region and the bottom of the CB oscillating at twice the pump frequency [75]. DFT simulations revealed the role of inter- and intra-band currents in GaAs, with the latter dominating the observed transient signal. Finally, in conditions where the XUV photons are probing regions of the band structure where no carriers are injected, Lucchini et al. probed the ultrafast modification of the electronic bands induced by the strong IR field, explained in terms of the dynamical Franz-Keldysh effect[76].

To study the response of the material following the excitation of carriers from VB to CB, a linear pumping regime is desirable in order to rule out laser-induced modifications of the material properties and focus on the generation and evolution of carrier population. To study these phenomena in real-time the attosecond resolution is not strictly needed (temporal resolution is given by the femtosecond duration of the pump pulse) but the broadband spectrum carried by IAPs or APTs ranging in the XUV-SXR region allows the probing of a wide range of the electronic band structure. A clear example of this application is the work published by Zürch et al., investigating carrier and structural dynamics in nanocrystalline Ge thin films [77]. An XUV IAP probes absorption changes at the Ge M-edge induced by the creation of electron and hole distributions respectively in CB and VB. An iterative numerical fit routine allows them to disentangle pure state-blocking signals (the presence of an electron/hole blocks/allows XUV-induced electronic transitions) from carrier-induced edge shift and broadening, interpreted in terms of band-gap renormalization, a well-known effect in semiconductor physics. The high spectral resolution of the experiment helped to follow the evolution of electron and hole populations through different valleys of the band structure.

Besides the evolution of the excited electron and hole population, several ultrafast phenomena involving both the electronic and lattice degree of freedom have been resolved using attosecond XUV pulses. The laser-induced impulsive coherent excitation of phonon modes in crystals has been studied in two recent works, respectively on Bi [78] and $LiBH_4$ [79], where the phonon excitation produces modulations of the XUV absorption, from which the phonon frequency can be extracted via time-domain analysis. A charge transfer mechanism following photoexcitation leading to the formation of polarons was detected by Carneiro et al. in haematite (α-Fe_2O_3) [80]. The evolution of a system undergoing a photoinduced phase transition, like VO_2, has been investigated by Jagel and coworkers in [81], where XUV TA measurements revealed an underlying process more complicated than a purely-phononic (vibrational periods are on the order of 100 fs) or purely-electronic effect (the period related to the plasma frequency is 4 fs).

In conclusion, it is important to highlight that while a wide variety of studies of attosecond-resolved dynamics in different materials have been reported using XUV pulses, very few examples employing attosecond X-ray pulses are present to date. On one side, two sources generating femtosecond SXR pulses via HHG reaching the carbon K-edge (284 eV) have been used to study molecular dynamics. Attar et al. investigated an electrocyclic ring-opening reaction in cyclohexadiene following absorption of UV light by monitoring changes in absorption at the carbon K-edge [29]. The dissociative dynamics of CF_4 and SF_6 following laser-induced ionization have been studied by Pertot et al. by following transient SXR absorption at both carbon K-edge and sulfur L-edges ($180 - 240$ eV) [82]. The only one study of attosecond-resolved dynamics in solids using attosecond SXR sources is the work we realized in our group studying ultrafast carrier motion in a transition-metal dichalcogenide (TiS_2) [83]. A few-cycle IR pulse promotes carriers from VB to CB through a direct band-gap of 0.23 eV, while the system is probed by an SXR ultra-broadband attosecond pulse spanning over the water window region (from the carbon to the oxygen K-edges, $284 - 543$ eV). An oscillating signal at twice the IR laser frequency is detected at the bottom of the CB, probed by SXR absorption at the Ti L-edge ($458 - 464\,\mathrm{eV}$) and interpreted, through the help of numerical simulations, as laser-driven intra-band carrier motion. This work and the one presented in this thesis (4) aim at opening the way to the application of attosecond pulses to study electron and structural dynamics to the SXR region, hence exploiting all the advantages given by X-ray spectroscopy (discussed in details in Chap. 3).

1.2 Ultrafast dynamics in graphite: state of the art

The crystalline structure of carbon atoms known as graphite (shown in Fig. 1.3b) is the result of the sp^2 (trigonal) hybridization of carbon's orbital s, p$_x$ and p$_y$, while the remaining p$_z$ is oriented perpendicularly to the plane defined by the sp^2 orbitals [84]. The three-dimensional structure consists of a vertical series of planar layers (called graphene), arranged in the so-called AB stacking configuration. In the graphene layer, carbon atoms are arranged in a hexagonal pattern at a distance of 1.42 Å from each other and they are connected by the strong covalent bonds resulting from the sp^2 hybridization and denominated σ. Consecutive graphene layers are separated by a distance of 3.35 Å and kept together by the weak van der Waals force produced by the delocalized π orbitals (related to the atomic p$_z$ orbitals), oriented perpendicularly to the graphene layers [85]. If the AB stacking is conserved for long-range distances, the crystal structure is usually denominated highly-oriented pyrolitic graphite (HOPG), while amorphous graphite refers to graphite crystals where the AB stacking is conserved only for short distances. The nature of the chemical bonds is responsible for the different intra- and inter-layer properties of graphite: the covalent σ bonds produce a metallic behavior within the graphene layer, while the van der Waals force makes graphite a poor electrical and thermal conductor perpendicular to the layers.

The electronic band structure produced by graphite's lattice structure and carbon's electronic configuration is reported in 1.3a as the result of DFT calculation performed with the Quantum Espresso package [86]. Each carbon atom has four electrons in the valence shell and the crystalline unit cell is formed by four atoms. The 16 electrons per unit cell are generating 16 bands, of which 12 are σ-bands and 4 are π-bands. For the σ-bands, 6 have a bonding char-

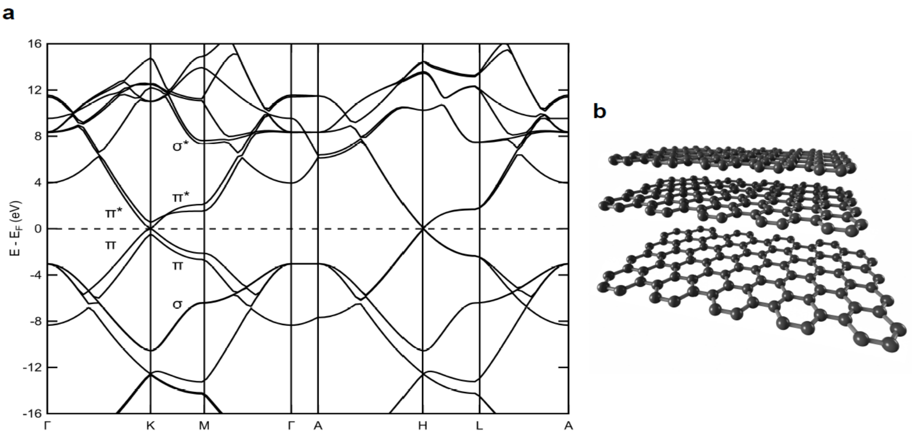

Figure 1.3: Electronic band and crystalline structure of graphite. a) presents the band structure of graphite calculated with the DFT package Quantum Espresso. The main contribution to both valence (VB) and conduction bands (CB) are reported in terms of π (VB) and π^* (CB) bands, originated by the carbon p_z orbitals and of σ (VB) and σ^* (CB) bands, results of the sp^2 hybridization. In b) the crystalline structure is shown: a vertical stack of graphene layers kept together by weak van der Waals forces, while the hexagonal in-plane structure is the result of the sp^2 hybridization of carbon atoms.

acter and 6 anti-bonding, with the two groups separated by an energy gap of $\sim 5\,\text{eV}$. The π-bands lie between the σ-bands and form the top of the VB and the bottom of the CB (as indicated in 1.3a). Only 8 of the 16 bands are filled, resulting in a Fermi level (the energy of the highest occupied electronic state) lying in between the 4 π-bands. The nearly-zero energy band-gap (40 meV [87], confirmed by DFT calculations) opening at the K point of the reciprocal lattice and the overlap of the highest valence π-bands at the Brillouin zone edges make graphite a semimetal material. The band-gap is not present in single-layer graphene because of a degeneracy argument, removed in graphite by the AB vertical stacking. The position of the Fermi level can be manipulated to be in the VB or CB by controlling the carrier doping [88], the sample temperature [89] or by applying an electrical voltage [90].

The most attracting properties of graphite and graphene, which make them some of the most studied solid-state materials of the last decades, all derive from the band dispersion in the proximity of the K point of the reciprocal lattice (see band structure in 1.3a). The π-bands at both the top of the VB and the bottom of the CB exhibit an almost-linear dispersion (linear for the gapless graphene), meaning that electrons are described by a linear relationship between energy and momentum, hence behaving like massless Dirac fermions [86, 91, 92]. This property of the electronic band structure gives rise to a wide variety of unique phenomena characterizing the optical and electronic properties of graphite. Quantum integer and fractional Hall effect [93], high conductivity, and carrier mobility and near-ballistic transport at room temperature [92, 94], broadband optical absorption from the far-IR up to the ultraviolet region [95], saturable absorption are examples of graphite's extraordinary properties. The miniaturization of graphite thin film (down to the single layer) has opened the way to a wide range of possibility in the field of optoelectronics (photovoltaic devices, light-emitting devices, photodetectors, terahertz devices, etc.), which have nowadays become of ordinary use in technological applications [96, 92]. Finally, the metallic nature of graphite within the graphene layer makes it a good thermal conductor along the plane, while it becomes an insulator in the perpendicular direction [97]. The in-plane lattice geometry is responsible for strong coupling between the electronic and vibrational degrees of freedom, determining the dominating energy decay channel following photoexcitation, as deeply described in Sec. 1.2.1 and 1.2.2.

With the advent of femtosecond lasers and the establishment of pump-probe techniques, a new world of possibilities opened up for the study of light-induced dynamics in the matter. Graphite and graphene became the object of a wide variety of experimental investigations to study the interaction with a laser pulse and the mechanisms through which the deposited energy is dissipated. Through the use of different experimental techniques, several attempts have been made to describe the excitation of charge carriers from VB to CB and the phenomena ruling the decay channels, involving both carriers and lattice. An overview of the most important results in terms of carrier and lattice dynamics are presented respectively in Sec. 1.2.1 and 1.2.2. The close analogy between optical, electronic and thermal properties of graphite and graphene is the reason why this overview contains experiments conducted on both materials.

1.2.1 Carrier dynamics

In static conditions, graphite is considered a semimetal because of its nearly-degenerate band structure at the K point, producing a band-gap of $\sim 40\,\mathrm{meV}$ (see Fig. 1.3a). Modification of the Fermi edge position through carrier doping [88], temperature [89] or by applying an external electrical voltage [90] can create electron and hole pockets conferring graphite a metal-like behavior. The shape of the π and π^* bands allows optical absorption in a wide range going from the far-IR up to the UV range. Absorption of photons at these frequencies will promote electrons from π (VB) to π^* (CB) band, leaving a concentration of holes in the π (VB) band. The evolution of these photoexcited charge carrier distributions has been and still is the object of study of several time-resolved investigations.

The evolution of the carrier distributions in graphite takes place on a timescale shorter than 1 ps, which translates in the need of experimental techniques with femtosecond temporal resolution. The first pump-probe investigation with sub-picosecond resolution was carried out by Seibert et al. ([98]) in 1990. Using an optical pump-probe setup employing 50 fs pulses, they reported the saturation of pump light absorption and interpreted the result in terms of a state filling process (usually referred to as state- or Pauli-blocking) producing a hot dense electron plasma in the π^* band. By monitoring the change in optical absorption, they concluded that a carrier thermalization process takes place after photoexcitation on a timescale faster than 50 fs (hence limited by the temporal resolution of the technique) followed by a subsequent slower cooling process involving carrier-phonon scattering. They finally found a dependence of the characteristic time of the carrier-phonon scattering process on pump fluence and probe wavelength, suggesting a connection to the electronic states involved in the process. The excited carrier lifetime and its dependence on the electronic energy state have been studied in graphite both theoretically [99] and experimentally [100]. Results are showing that the scattering rate (the inverse of carrier lifetime) does not depend quadratically on the energy (relative to the Fermi edge) as expected for a 3D gas of interacting electrons according to Landau's theory [101]. Scattering rate data rather follows the shape of the band structure (namely the density of states (DOS)) and presents singularities for energies close to the critical points of graphite's band structure (in this case, at the M point of the reciprocal lattice).

Kampfrath et al. [102] were among the first to discuss the coupling of the excited electron distribution to phonon modes. By analyzing the transient dielectric function measured with time-resolved THz spectroscopy, they detected an increase in absorption at frequencies higher than 15 THz at 500 fs after photoexcitation. They modeled the observed changes introducing the coupling of optical phonons (frequencies higher than 15 THz) to electronic transitions, resulting in the best fit to the transient dielectric function data. Finally, they estimated that after 500 fs most of the excitation energy of the electronic system (90%) is transferred to these optical phonons, which are then denominated strongly-coupled optical phonons (SCOPs) because of the strong effect on electronic properties at these timescales. Only with the use of shorter laser pulses (< 10 fs), like in the case of the experiment carried out by Breusing and coworkers [103], better insight on the thermalization processes was given. The higher temporal resolution allowed the identification of a first ultrafast decay of 13 fs, assigned to carrier-carrier thermalization, accompanied by a slower one of about 100 fs and interpreted as carrier-phonon scattering. The broadband spectrum provided by the < 10 fs pulses has been used to verify that the decay time decreases for increasing probe energies (i.e. electrons further away from the Dirac point, in line with [100]), see Fig. 1.4a,b. Imposing a Fermi-Dirac (FD) distribution to the measured data revealed the creation of electron and hole distributions with different chemical potentials recovering the equilibrium in less than a picosecond.

After the general physical picture following $\pi - \pi^*$ photoexcitation was established (carrier-carrier thermalization after tens of fs, carrier-SCOPs thermalization on few hundreds of fs timescale), two main research directions developed with a focus on carrier dynamics. The first aimed at understanding the formation of the out-of-equilibrium electron distribution and its evolution in terms of carrier thermalization before the scattering with the optical phonons takes place. The second mainly focused on trying to understand which mechanisms are dominating carrier-carrier scattering processes, responsible for the ultrafast energy and momentum redistribution of the photoexcited carriers. Most of the studies have been extended to the more popular case of graphene: in general, the interpretation of these processes can be applied to both graphite and graphene because of their almost identical band structure.

The electronic system is described by a FD statistical distribution if in conditions of thermodynamic equilibrium, which is safe to assume in absence of any pump pulse (the same probe pulse can move the electronic system towards out-of-equilibrium conditions, but this effect is not considered here). The prob-

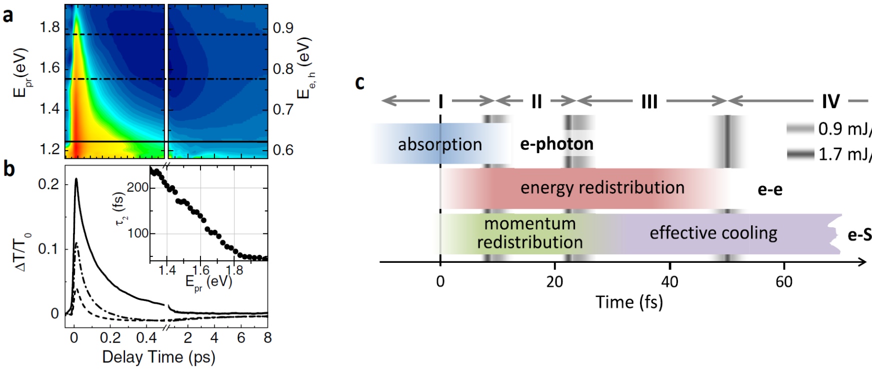

Figure 1.4: Ultrafast carrier dynamics in graphite following $\pi - \pi^*$ excitation. a) Spectrally resolved differential transmission (DT) as function of time delay and probe photon energy E_{pr}. b) DT for $E_{pr} = 1.24\,$eV (solid), $1.55\,$eV (dash-dotted) and $1.77\,$eV (dashed). Inset: Decay time τ_2 vs E_{pr}. Reprinted with permission from [103]. Copyright (2009) by the American Physical Society. c) Stages of thermalization and characteristic timescales of energy and momentum exchange processes. Time markers separating the stages result from the evaluation of the experimental data for $F = 0.9$ and $F = 1.7\,$mJ/cm^2. Reprinted with permission from [104]. Copyright (2018) by the American Physical Society.

ability distribution is described by

$$FD(E, T_e, \mu_e) = \{\exp[(E - \mu_e)/k_B T_e] + 1\}^{-1} \tag{1.4}$$

where k_B is the Boltzmann constant, T_e is the temperature of the electronic system, μ_e is the chemical potential and E the electron energy (same can be written for the holes, with an inverted sign for the probability distribution). The photoexcitation process creates carrier distributions out of equilibrium, for which the FD statistics is not valid anymore. Subsequently, a carrier thermalization process is initiated to restore an equilibrium state, which happens to be at a higher temperature compared to the initial state (a hot electron gas has been created). Finally, the system loses energy going back to a low-temperature state by carrier-carrier and carrier-phonon scattering. In the work of Stange et al. [105], a detailed description of the numerical methods to extract important parameters like carrier temperature and chemical potential from time-resolved angularly-resolved photoemission spectroscopy (ARPES) data is presented. The transient electronic temperature is then fitted with the so-called three-temperature model (3TM, explained in detail in Sec. 4.2.5) describing the energy exchange between the carrier, the SCOPs and the lattice thermodynamic systems, confirming the fast and strong coupling of the electronic excitation to optical phonons. By pushing the temporal resolution of time-resolved ARPES to $\sim 10\,\mathrm{fs}$ with the use of few-fs pulses, Rohde and coauthors [104] identify the timescales of the different steps bringing to the formation of the hot electron gas and its further decay, see Fig. 1.4c. After 8 fs most of the pump pulse is already absorbed, creating an anisotropic electron distribution in both energy and momentum. The momentum distribution is fastly redistributed via carrier-carrier interaction at around 22 fs, while the electronic system is internally fully thermalized (i.e. also energetically redistributed) only at 50 fs after the pump arrival. The main channel for energetic redistribution is the scattering with SCOPs, starting earlier than 50 fs and lasting for several tens of fs.

In order to shed light on the carrier-carrier scattering mechanisms taking place on the first tens of fs after photoexcitation, Winzer, Malic, and coworkers [106, 107, 108, 109] introduced a theoretical background considering different carrier-carrier interactions, with particular attention to Auger processes. These processes (called Auger Heating (AH) and its counterpart Impact Ionization (II), see Sec. 4.2.2) involve either the annihilation or creation of an electron-hole pair along with, respectively, the energy gain or loss by a third electron. Their calculations show that, under certain circumstances, carrier multiplication takes place in graphene and graphite, resulting in the generation of more carriers in CB (or VB, the same argument can be extended to holes) than the ones generated by pump-light absorption, hence making these materials appealing for optoelectronics applications [96]. Experimental proofs are found for graphene in the works from Brida et al. [110] and Gierz et al. [111], reporting the detection of carrier multiplication in graphene under certain pump pulse and time resolution conditions (see Fig. 1.5), while still no evidence has been reported for graphite. The topic of carrier multiplication will be described in detail in Sec. 4.2.2 together with the presentation of our results.

1.2.2 Lattice dynamics

In the previous section, a list of important works on carrier dynamics in graphite has been presented. Here the attention is moved to dynamics involving the lattice degrees of freedom. Starting from the condition that the excited carrier

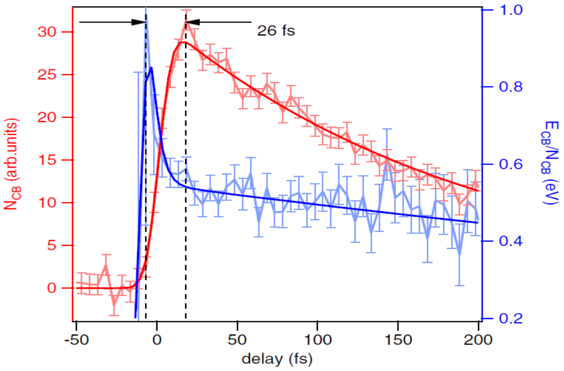

Figure 1.5: Direct evidence for impact ionization in graphene. Comparison between the temporal evolution of the total number of carriers in conduction band (N_{CB}, light red) and their average kinetic energy (E_{CB}/N_{CB}, light blue). Reprinted with permission from [111]. Copyright (2015) by the American Physical Society.

distribution dissipates most of the acquired energy into the carrier-SCOPs scattering channel [102], a list of the experimental works elucidating the nature of the vibrational dynamics involved is presented.

For graphite, the vibrational properties are mostly dictated by the hexagonal symmetry of the graphene layers, the result of the strong covalent bonds produced by the sp^2 hybridization (1.3b). The interatomic force inside the graphene layer is stronger than the van der Waals force acting between different layers: for this reason, graphite, graphene and carbon-based structures (i.e. nanoribbons, nanotubes) share the same lattice properties. The phonon band dispersion of graphite (shown in Fig. 1.6 as the result of DFT calculations) and the identification of the atomic displacements produced by the main phonon modes in real space are present in the work of Maultzsch et al. and Mohr and coauthors [112, 113]. Through inelastic x-ray scattering and by comparison with available DFT calculations, they mapped the phonon band dispersion over the main crystallographic directions, identifying several acoustic bands and three main optical bands, one longitudinal and two transverse, with energies in the range of $150 - 200\,\mathrm{meV}$.

A different type of characterization of the vibrational properties of graphite

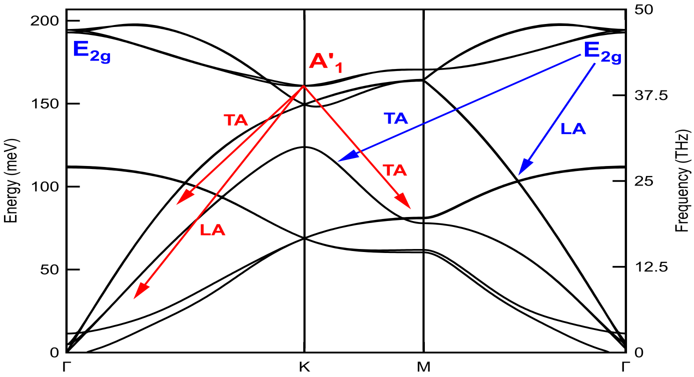

Figure 1.6: Phonon band dispersion of graphite obtained with DFT calculations. The optical modes that strongly couple to the electronic excitation, the E_{2g} and A'_1 mode, are highlighted, together with the main decay channels involving interaction with lower-frequency phonons (TA stays for transverse-acoustic, LA for longitudinal-acoustic) identified by Stern et al. in [114]). The overestimation of the A'_1 mode frequency (corresponding to 35 THz based on literature [113, 112]), is due to inaccuracy of set of parameters used for DFT calculations.

and graphene is provided by studies of Raman spectroscopy [115, 116]. Light can interact with the crystal via Raman scattering only for vibrational modes (so-called Raman-active modes) satisfying the selection rules: the susceptibility tensor ruling the non-linear interaction with the laser field must have off-diagonal terms (mode is not fully-symmetric). For the case of HOPG, there are two different Raman-active modes, both situated at the Γ point of the phonon band structure: the E_{2g2} optical mode (47 THz), completely inside the graphene plane, and the E_{2g1} acoustic mode (1.3 THz), also known as shearing mode, where the graphene planes slide against each other (for mode visualization, see [117, 113, 115]). The Raman peak corresponding to the E_{2g2} mode is usually called G-peak. The Raman spectra of HOPG presents a second peak at higher energies (75 THz), usually called the 2D peak: it is originated by a two-phonon excitation of the fully-symmetric A'_1 mode at the K point of the reciprocal lattice, not active for single-phonon Raman excitation. For the case of multicrystalline graphite, the increased disorder reduces the symmetry of the A'_1 mode and a third Raman peak appears, corresponding to the single excitation of the A_1' optical phonon at 37 THz. For the rest of the manuscript, the E_{2g2} mode will be referred to as E_{2g}, while the E_{2g1} mode will be called the shearing mode.

Phonon excitation in graphite can be achieved through electron-phonon coupling (EPC) following $\pi - \pi^*$ electronic excitation (as described in the previous section) or by coherent interaction of an ultrashort laser pulse with the vibrational modes of the crystal. In the former case, the process is initiated by a scattering event, resulting in an incoherent excitation of phonon modes satisfying energy and momentum conservation. In the latter case, if the laser's pulse duration is shorter than the vibrational period of the phonons, the laser field can coherently excite phonons in the crystal. The excitation takes place through Impulsive Stimulated Raman Scattering (ISRS) for Raman-active modes, while fully-symmetric modes can be excited according to the Displacive Excitation of Coherent Phonons (DECP) mechanism if the laser is in resonance with electronic excitation. A detailed discussion about ISRS and DECP is reported in Sec. 4.2.6 or can be found in [118, 119, 120].

The coherent excitation of the shearing mode in graphite was reported for the first time by Mishina and co-authors [117]: the interaction of a 130 fs pump laser with the sample coherently excites the Raman-active mode, which modulates the transient reflectivity signal detected in the experiment. The frequency of the shearing mode is found to be independent of the carrier excitation, while it redshifts for increasing lattice temperature. With the same experimental setup but involving shorter laser pulses (< 10 fs), Ishioka et al. some years after revealed the coherent excitation of the E_{2g} optical phonon mode along with the shearing mode [121]. The increased temporal resolution allowed them to follow the dynamics of the E_{2g} mode, which frequency changes in less than 1 ps after photoexcitation. They interpret these changes by stating that the E_{2g} is involved in the strong EPC following photoexcitation: the dynamics of excited carriers influence the phonon dispersion at the Γ point, where a Kohn anomaly is present. A Kohn anomaly is a discontinuity in the derivative of the dispersion relation that occurs at certain high symmetry points, proper of metallic materials and in general system with strong EPC, like graphite. Similar conclusions were found by Yan and co-workers using time-resolved Raman spectroscopy [122]: the dynamics of the E_{2g} mode were studied, evolving in time with a decay constant of ~ 2 ps. With a different experimental approach (ultrafast core electron energy-loss spectroscopy), van der Veen et al. [123] studied the electronic and structural dynamics of graphite with femtosecond and nanosecond temporal resolution. An electron pulse is interacting with the target as in the case of ultrafast electron diffraction (UED), but instead of analyzing the resulting diffraction pattern, the transmitted electrons are energy-dispersed by means of an electron spectrometer. In this case, energies above 100 eV were considered, to access core-shell electronic transitions the same way XAFS spectroscopy does. Their results indicate that the modification of the carbon-carbon distances (as a result of the EPC) can affect the shape of the electronic band structure on the ps time scale, producing an effect similar to band-gap renormalization in semiconductors.

A deeper insight on which modes are actually participating in the strong EPC is found in the works of Yang, Chatelain and Stern [124, 125, 114]. In the work of Yang et al., by the combination of time-resolved ARPES and Raman spectroscopy, beside the coupling to the E_{2g} mode already presented in [121] a new decay channel is proposed involving first the excitation of optical phonon modes at the K point, suggesting a relation to the A_1' mode. UED is instead the experimental technique used in the works of Chatelain and Stern. By measuring the pump-induced changes on the scattering intensity at different peaks of the reciprocal lattice, transient data shed light on the different phonon modes involved in the EPC and their dynamics. Chatelain et al. confirmed the incoherent excitation of the E_{2g} and A_1' optical modes via the strong coupling following $\pi - \pi^*$ excitation. At later times, they detected on top of the incoherent transient signal the coherent excitation of two low-frequency acoustic phonon modes: the shearing mode, as for [117, 121] and the so-called breathing mode, corresponding to an expansion of the interlayer distance plus an oscillation at 0.2 THz. As a consequence of the excitation of the breathing mode, the interlayer distance resulted to be modified by ~ 0.1Å, at least one order of magnitude larger than other vibrational amplitudes in graphite. Finally, Stern et al. followed the same approach of [125], but rather focusing on the decay of the incoherently excited E_{2g} and A_1' optical mode. A decay on the $1-2$ ps time scale was found consisting of two-phonon excitation at half the initial frequency and opposite wave-vector: the top part of the acoustic branches along both ΓK and ΓM starts to be populated until further decay takes place towards the lower-frequency region.

1.3 Conclusions

In this introductory chapter, two research fields have been presented constituting the background from which my Ph.D. project developed. On one side, the field of attoscience providing the possibility to generate ultrashort light pulses in the XUV-SXR photon energy range and to exploit them to study atomic-scale electron dynamics in real time. On the other side, the unique electronic and thermal properties of graphite, resulting in extremely interesting carrier and structural dynamics taking place on a ultrafast timescale.

The emergence of attosecond science constituted a technological and scientific revolution which allowed to go beyond the limits set by the use of femtosecond lasers in studying ultrafast phenomena. The possibility to generate sub-fs light bursts, both in the shape of isolated pulses or of pulse trains, with photon energies in the XUV-SXR range allowed the use of new methods to investigate electron dynamics in atoms, molecules and solids. By means of transient XUV-SXR absorption or photoemission spectroscopy, phenomena like tunneling ionization, charge localization and migration, bond breaking have been observed with sub-fs resolution.

Most of the extraordinary properties of graphite are consequences of the almost-linear dispersion of the electronic band structure around the Fermi level in the proximity of the K-point of the reciprocal lattice. The nearly-metallic behavior of the single 2D layers, called graphene, is responsible for graphite's electronic properties, like high conductivity and high carrier mobility. These properties, together with a broadband optical absorption from the IR to the UV range, do not strongly depend on the thickness of the material, making graphite suitable for implementation in optoelectronic devices.

Despite several experimental works have been reported on both carrier and structural dynamics in graphite, there are few open questions which have not been addressed yet, mainly related to the limitations of the experimental techniques used. The ultrafast response of carriers to an intense electric field carried by a laser pulse has never been investigated. While the evolution of the excited electron distribution in conduction band has been intensively studied, at date no real investigation has been reported on the evolution of the hole distribution produced in the VB after photoexcitation. The analysis of the mechanisms ruling the ultrafast carrier-carrier scattering is only available for the case of graphene, while it is still debated whether the results apply to the case of graphite too. Finally, an experimental study able to directly observe dynamics involving both carrier and lattice degrees of freedom all at once is still lacking: the strong electron-phonon coupling has always been indirectly inferred by looking at physical quantities related to either the electron or the lattice system. With the work presented in this thesis, we aim at answering these open questions.

Chapter 2

Beamline for attosecond SXR spectroscopy

This chapter contains a detailed description of the experimental setup built to produce isolated attosecond soft X-ray (SXR) pulses and to realize time-resolved XAFS experiments using an IR pump - SXR probe scheme.

In Sec. 2.1, a brief presentation of the laser system used to drive the high-harmonic generation (HHG) process is provided, with a particular emphasis on the HHG process driven in ionization-gating conditions and exploiting the ponderomotive scaling of the emitted photon energy.

In Sec. 2.2, the scheme implemented for HHG is presented, together with a description of how the SXR radiation is propagated and detected along the beamline. Characterization of the SXR source in terms of stability and flux will be presented together with its spectral tunability in the SXR range from below 200 eV up to 550 eV, covering the so-called water window spectral region. Finally, the results of the temporal characterization of the isolated attosecond pulses (IAP) will be discussed.

The chapter ends with a description of the IR pump - SXR probe scheme implemented for time-resolved XAFS studies in Sec. 2.3. The different pumping schemes implemented will be presented together with the procedure to determine the spatio-temporal overlap between the pump and the probe pulses.

2.1 Laser system

As explained in Sec. 1.1.1, the main ingredients that a laser system must have in order to drive the HHG process are: high pulse intensity (ranging in the $10^{14}\,\mathrm{W/cm^2}$ range), short pulse duration (usually down to the few-optical-cycle level), control on the CEP and in general good stability performance, which are needed to achieve good spectral stability of the HHG output. In addition to this, to extend the HHG spectrum to the SXR region the quadratic dependence of the cutoff energy on the laser wavelength has to be exploited, resulting in the need of a laser system working at wavelengths longer than the output of commercially available Titanium:Sapphire (Ti:Sa) laser systems. To satisfy all these conditions, the laser architecture consists of a multi-mJ femtosecond Ti:Sa system which output is used as a seed for a high-energy optical parametric amplification (OPA) stage used for wavelength conversion. Finally, a pulse compression scheme is implemented before entering the Attosecond beamline. A detailed explanation of the laser system can be found in [126].

The Ti:Sa system is composed of two chirped-pulse amplification (CPA) stages, namely a regenerative amplifier cavity followed by a multi-pass booster, both partially home-built, and a pulse compressor (see the sketch reported in Fig. 2.1). The 80 MHz, 15 fs femtosecond output of the oscillator is firstly modulated in amplitude and phase by an acousto-optic programmable dispersive filter (Dazzler, Fastlite) for spectral shaping and then temporally stretched to about 200 ps before entering the two stages for CPA. The first stage is a cryogenically-cooled regenerative amplifier cavity working at 1 kHz repetition rate in which the pulse energy is brought from the nJ up to $2 - 2.5\,\mathrm{mJ}$ level, where the effect of gain narrowing is mitigated by the spectral shaping induced by the Dazzler.

The cavity output is then propagated to the next stage, consisting of a multipass booster amplifier, still cryogenically-cooled, where amplification up to $10 - 11\,\mathrm{mJ}$ is achieved. In both amplification stages, the crystals are pumped with high-power diode lasers (respectively 20 and 50 W), for which heating effects like thermal lensing are not negligible. The high-power cryogenic system (Cryomech) connected to both crystals ensures the handling of the high power deposited, resulting in high-quality spatial properties of the output beam, key ingredient for efficient non-linear wavelength mixing. The final stage of the Ti:Sa system is the pulse compressor, where a pair of reflective gratings are used to recompress the pulses to 40 fs pulse duration.

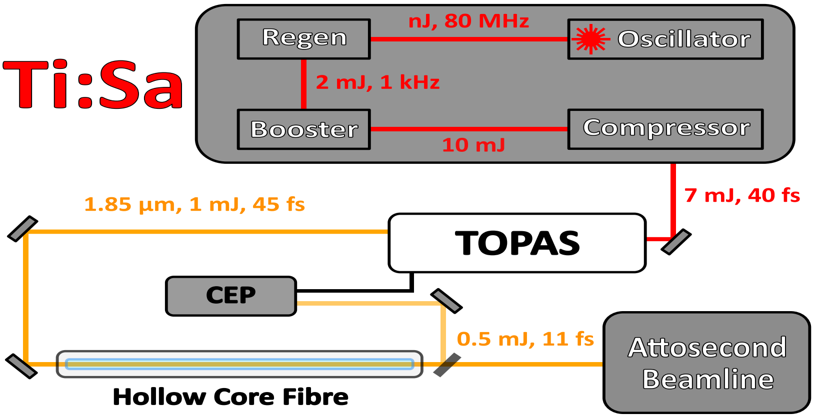

Figure 2.1: Schematics of the laser system, from the Ti:Sa part up to the entrance of the Attosecond Beamline. Listed after each step are some key laser parameters, like pulse energy or temporal duration. At the output of the hollow-core fiber (HCF), the dichroic filter (RG1000, Schott) is represented, used both for pulse compression and for the CEP f-2f interferometer.

The output of the Ti:Sa system is propagated up to the beginning of the second part, where it enters a commercial set of OPA stages (HE-TOPAS, Light Conversion) to downconvert the 800 nm output to longer wavelengths. In the first stage, the 800 nm seed is combined non-collinearly in a beta barium borate crystal (BBO) with a white-light continuum generated in a yttrium-aluminum-garnet (YAG) to amplify its 1.3 μm component. In the second stage, the 1.3 μm pulse is used as the signal and it is further amplified by the 800 nm seed in a collinear OPA in a BBO crystal, resulting in the creation of an idler centered at 1.85 μm. It is very important to stress that the 1.85 μm component is inherently CEP-stable, being the idler of the OPA process in which the random phase component carried by the two other pulses gets canceled out. The final stage is a non-collinear OPA stage, again in BBO, where the main portion of the input 800 nm seed (almost 90%) is used to boost the amplification of the idler, resulting in a final output of 1 mJ at 1.85 μm, slightly stretched towards 45 fs because of propagation through OPA crystals. Together with the idler, the output also contains the leftover 800 nm seed and the signal at 1.3 μm, both spatially separated from the idler because of the non-collinear angle in the last stage.

After creating high-energy pulses at SWIR wavelengths, they are post-compressed down to the few-optical-cycle regime thanks to self-phase modulation (SPM) achieved in glass HCF, a standard scheme for high-energy pulses firstly proposed by Nisoli et al. [127] for 800 nm light sources and then adapted to the SWIR [128]. Coupling the laser into a glass capillary of few-hundred-μm inner diameter (ID) filled with a noble gas (usually Argon or Neon, depending on pulse energies involved), the propagation of high-intensity pulses allows SPM to take place and a multi-octave-spanning spectrum can be generated, while more than 50% of input light can be coupled. In our case, using a HCF with 300 μm ID filled with 1 bar of Argon, spectra like the one in Fig. (see 2.2 below) can be generated, supporting Fourier-transform limit of less than 10 fs, with around 550 μJ of pulse energy at the output.

The broad 1.85 μm pulses are then propagated through a bulk piece of glass, namely a 2 mm IR filter (RG1000, Schott), to partially compensate the remaining spectral phase. After the filter, pulses have been temporally characterized with a home-built second-harmonic frequency-resolved optical gating (SH-FROG) setup [129], measuring a pulse duration of 11.2 fs (see Fig. 2.2), which at this wavelength correspond to slightly less than two optical cycles ($T_{1.85\mu m} = 6.17$ fs).

I have already mentioned while describing the TOPAS setup, that the 1.85 μm pulse is CEP-stable being the idler of the OPA process. If on one side this property excludes random shot-to-shot fluctuations, CEP stability can be deteriorated by environmental conditions affecting the pulse propagation in the long term. As already said in Sec. 1.1.1 and as it will be shown in the next one, the HHG spectrum heavily depends on the CEP value [27], especially in the cutoff region, so it would be impossible to acquire meaningful spectroscopic data with a spectrum that drifts over time. To overcome this issue, an f-2f interferometer was implemented in our setup exploiting the multi-octave-spanning spectrum, using the reflection of the RG1000 filter after the HCF. This reflection contains the blue tail of the spectrum below 1000 nm together with a small portion of the main part of the spectrum because of Fresnel losses. It is this second part that, once frequency-doubled in a BBO, produces a spectrum that overlaps with the blue tail of the fundamental, resulting in spectral fringes measured on a spectrometer. Through a feedback loop directly acting on a delay stage inside the

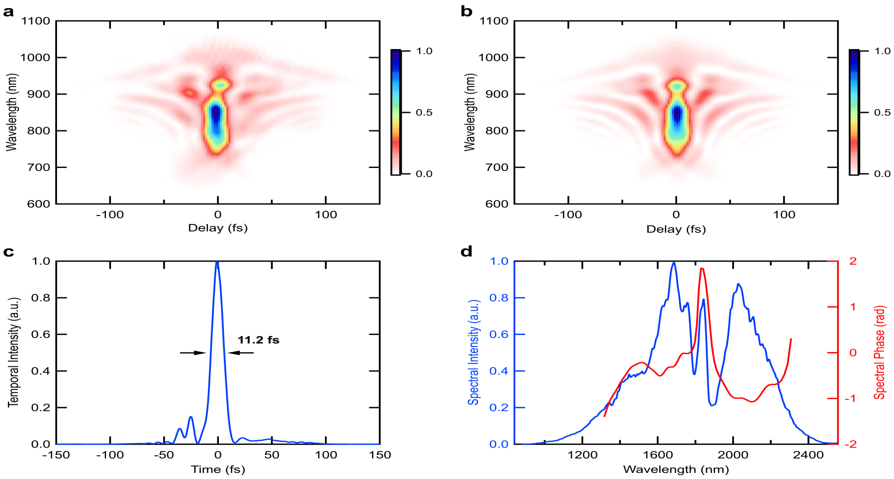

Figure 2.2: Spectral and temporal characterization of 1.85 μm pulse, measured at the input of the attosecond beamline. a) Measured SH-FROG trace, while b) presents its reconstruction using the PCGPA phase retrieval algorithm, in good agreement with the experimental one. In c) there is the retrieved temporal profile of the pulse. Finally, the measured spectrum is shown in d).

second stage of the TOPAS we are able to lock the CEP to a given relative value and doing so we can balance slow drifts. Using the feedback loop, we are able to go from around 300 mrads of CEP root-mean-square down to $<$ 100 mrads [25] and to keep it over the long time windows needed to do pump-probe experiments in these conditions.

2.2 HHG setup for attosecond SXR pulses

In Sec. 1.1.1 and 1.1.2 the process of HHG was presented, describing the different approaches used to generate IAP and to produce radiation in the SXR region. Here the experimental setup is presented, where a few-optical-cycle, 1.85 μm laser driver is chosen to generate IAPs spanning over the water window spectral region in the high-pressure, ionization-gating regime, as described in 1.1.1.

One key ingredient of each experimental setup built to work with XUV or X-ray light is the vacuum technology, as these types of radiation would propagate on incredibly short distances (on the order of mm) before being completely absorbed. For this reason, at the end of our optical table a thin fused-silica window ($400\,\mu$m thick, with anti-reflective coating for the broad $1.85\,\mu$m spectrum, glued on a metallic tube) separates the table, at atmospheric pressure, from the *Generation chamber*, as we usually refer to the vacuum chamber where the HHG process takes place (see Fig. 2.3 at the end of the section). In this chamber, by means of a mechanical booster pump (Leybold, $650\,\mathrm{m}^3/\mathrm{h}$), a pressure level of 10^{-4} mbar is maintained in static condition, while pressure can be kept to the mbar level when high gas pressure (around 12 bar) is used for generation. Due to the high capacity of the vacuum pump, it is possible to connect this chamber to the rest of the beamline without the use of any physical separator.

Once the laser beam is in the chamber, silver flat mirrors (Layertec, enhanced reflectivity around $1.85\,\mu$m) are used to guide it until the final concave silver mirror (Layertec, 200 mm radius of curvature), which focuses the beam into the gas cell. A motorized iris is also inserted on the beam path and used in the HHG optimization process to fine adjust the spatial properties of the beam and hence the phase-matching. At the focal plane, beam size of $50\,\mu$m full-width-half-maximum (FWHM) is obtained, which results in peak intensity of about $5 \cdot 10^{14}\,\mathrm{W/cm}^2$, range needed to achieve the ionization gating regime.

The design of the gas cell used to reach high pressure for HHG while keeping the ambient pressure in the chamber sustainable for the vacuum pumps has been the object of careful study and constitutes the core of the whole vacuum system (more details can be found in [130]). In addition, the remaining gas in the vicinity of the generation point will reabsorb the SXR radiation when the pressure becomes substantially higher than the mbar level. The final geometry consists of a stainless steel tube with 1.5 mm outer diameter and 0.5 mm inner diameter where 2 aligned holes of $200\,\mu$m diameter have been fabricated via laser drilling in order to accommodate the laser beam. Gas is injected from the bottom, where the gas cell is connected to a high-pressure gas line, and it can only stream through the small side holes, producing at the center a region of high pressure suitable for the interaction with the laser pulses.

Usual optimal pressures for HHG phase-matching with Helium are on the order of $10 - 12$ bar, for which we measure an ambient pressure in the rest of the chamber of around 10 mbar. This value is highly dependent on the vacuum pump performance and on the gas cell hole size (it scales with the fourth power of the radius). The high-intensity of the laser pulse can easily ablate stainless steel and, despite a careful alignment protocol, the hole quality deteriorates with time on a timescale of 2-3 months, after which usually the ambient pressure and the phase-matching backing pressure rise. Monitoring these pressure values while doing HHG helps us to diagnose the gas cell quality.

The interaction of high-pressure gas density with the few-cycle, high-intensity laser pulse translates in the generation of IAP with a spectrum reaching up to 550 eV when Helium is used (the cutoff energy is 160 eV in Argon, while it extends up to 400 eV using Neon). However, the optimization of the process requires the sensitive alignment of the laser beam through the gas cell (up to the end of the beamline) together with the control of macroscopic parameters like gas pressure, gas cell position along beam propagation and CEP (see sec. 2.2.2 to visualize their effect on the HHG spectrum).

Phase-matching conditions for these parameters ensure that there is only a short temporal window in which high-harmonics are efficiently generated, resulting in one (efficient) emission usually corresponding to the most-intense half-optical cycle. A detailed study for the phase-matching conditions of the HHG process with our parameters is presented in [131, 27], while experimental proofs come from attosecond lighthouse and attosecond streaking experiments [26, 52]. The results of the streaking measurements will be presented in sec. 2.4.

2.2.1 SXR propagation and detection

At the exit of the gas cell, the generated SXR beam will co-propagate with the IR driver along the same path, even though the beams have very different divergence. The two beams co-propagate together inside the *Differential pumping chamber* until entering the next one, called *Mirror chamber* (see Fig. 2.3), where pressure values are on the order of $10^{-6} - 10^{-7}$ mbar. At the beginning of this chamber, a motorized wheel gives the possibility to insert a thin metallic filter on the beam path to block the remaining IR driver while transmitting the SXR beam. Filters have thicknesses of $100 - 200$ nm and are chosen according to the spectral region needed for applications. In the water window spectral range, a common choice is to use either tin (Sn) or aluminum (Al) filters, for which transmission ranges between $50 - 70\%$ over the bandwidth of the HHG

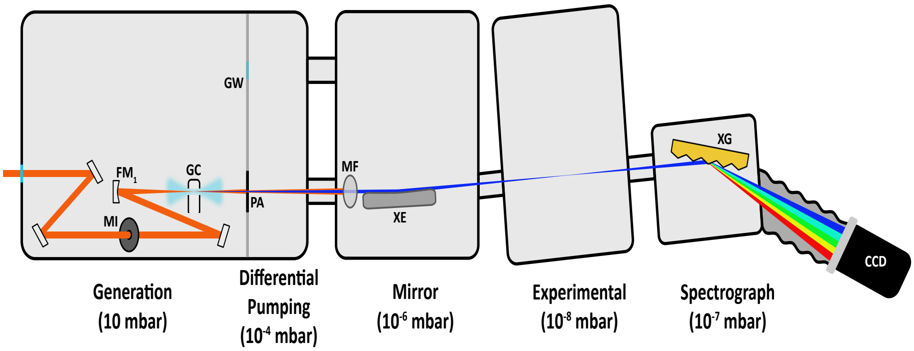

Figure 2.3: Setup for generation, propagation and detection of SXR attosecond pulses. A motorized iris (MI) is used to fine tune the beam profile after the beam is focused in the gas cell (GC) with the focusing mirror (FM$_1$). The pumping aperture (PA) and the glass window (GW) regulate the gas flow between the generation chamber and the rest of the beamline. The remaining IR is blocked at the metallic filter (MF) right before the ellipsoidal mirror (XE), used to refocus the SXR beam. Finally, the grating (XG) and the camera (CCD) allow the detection of SXR light at the end of the beamline. Pressure values obtained when HHG gas is flowing are indicated at the bottom of each chamber.

spectrum. Other filters, like carbon or titanium, are mainly used for the spectral calibration of the home-built spectrograph, due to their clear absorption edges at respectively 284 and 454 eV.

After the filter, the diverging SXR beam hits an ellipsoidal mirror, sitting 1.4 m after the HHG gas cell, and re-imaging the generation spot after 0.7 m with a magnification factor of 0.5. The mirror (Carl Zeiss Laser Optics) is coated with platinum with a final surface roughness of < 0.5 nm rms and is aligned to reflect the SXR at grazing incidence, namely 2°, to reduce the losses. The ellipsoidal mirror sits on a 6-axis hexapod positioner to achieve fine control of all translational and rotational degrees of freedom.

The reflection of the ellipsoidal mirror enters the next chamber, named *Experimental chamber*, designed such that the image plane of the ellipsoidal mirror coincides with its center. Here is where the sample is placed, mounted on a sample holder and moved with a 4-axis (3 translation + 1 rotation) linear positioner (Smaract) with sub-μm precision. A knife-edge measurement of the SXR beam revealed a spot size in focus of 12 μm FWHM (taken as the average of the beam radii on x- and y-axis, see Fig. 2.4), optimized for ellipsoidal mirror alignment. This chamber can reach vacuum levels down to $10^{-8} - 10^{-9}$ mbar and it has been used in the past also for charged-particle spectroscopy, like in the attosecond streaking measurement, reported in Sec. 2.4.

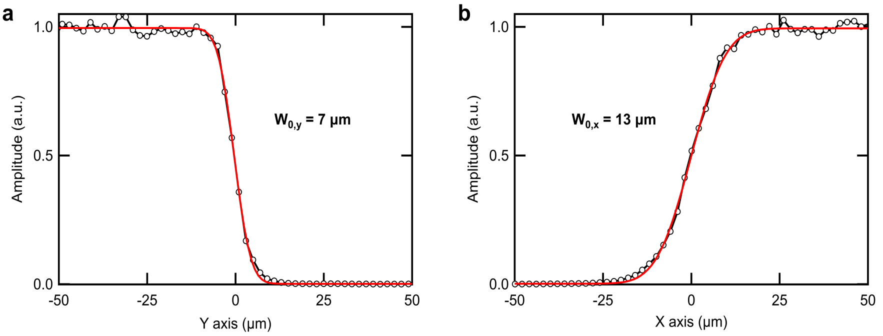

Figure 2.4: Knife-edge characterization of the SXR beam size at the sample plane in the experimental chamber. Vertical (a) and horizontal (b) cut in the transverse plane are presented, together with a fit using the error function, from which the beam radius w_0 can be extracted. The SXR beam FWHM is then calculated assuming the average of the radii and considering the relation $FWHM \simeq 1.18 \cdot w_0$. The slight astigmatism can be related to a minor ellipsoidal mirror misalignment.

Detection of the SXR radiation is performed via a home-built spectrograph, as sketched in Fig. 2.3. The experimental chamber is connected to a small vacuum chamber containing a flat-field, aberration-corrected, gold-coated, reflecting concave grating (2400 lines/mm, Hitachi High Technologies America, Inc.), which disperses the different wavelengths in the horizontal plane. The first diffraction order is detected by a cooled charged-coupled device (CCD) camera (PIXIS-XO, Princeton Instruments, $-75\,^{\circ}$C), connected to the grating chamber with a metallic bellow. The camera is positioned at the focal plane of the grating in order to re-image in the horizontal plane the focal spot of the experimental chamber. Nominal resolving power of the spectrograph is

${}^{E}/_{dE} = 1000$, which translates in a maximum spectral resolution of about 0.3 eV at 300 eV.

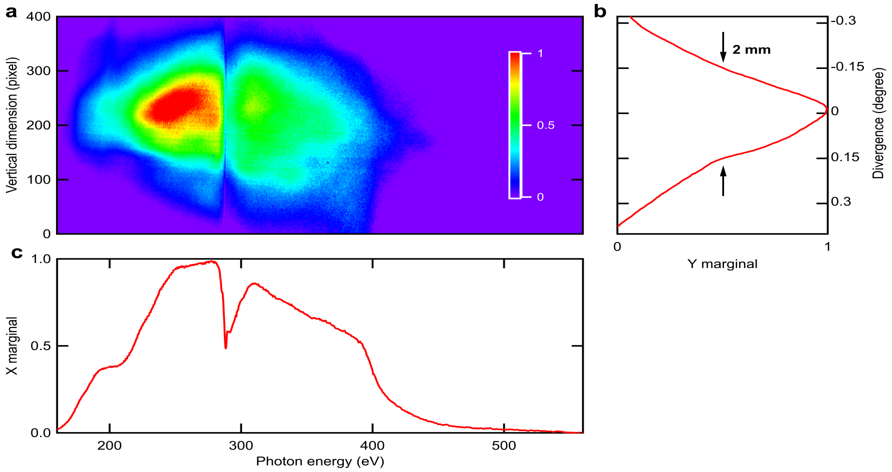

Figure 2.5: Detection of HHG spectrum generated in helium. a) shows the average of 20 2D spectra, each one obtained with 40 seconds integration time, optimized for flux at the carbon K-edge. b) Integration along the horizontal direction gives information about vertical beam size, where divergence has been calculated using the distance between the SXR and CCD plane of 472 mm. c) To obtain the SXR spectrum, integration along the vertical dimension is performed, revealing a broadband spectrum around the 284 eV, where clear carbon contamination is detected.

To estimate the flux of the SXR source, the number of detected counts on the CCD (see Fig. 2.5) can be converted to the number of photons considering that the operational regime produces 1 electron/count and that 3.7 eV are needed to generate an electron. This operation allows calculating the number of detected photons/second/eV, reported in Fig. 2.6a for spectra optimized in three different conditions, namely at the carbon K-edge (284 eV), nitrogen K-edge (410 eV) and titanium $L_{2,3}$-edge $(458-464\,\text{eV})$. To calculate the number of photons delivered to the sample, it is needed to take into account the response of the optical components seen by the SXR beam. The CCD camera has a detection efficiency directly related to the response of the silicon chip and ranges between $40-60\%$ for our bandwidth. The reflection from the SXR grating is only $\sim 1.5\%$, reducing consistently the number of detected photons. Finally, the transmission through an aluminum filter must be considered, blocking $\sim 50\%$ of the photons. Considering the spectrum corresponding to the red curve in 2.6a, the total number of photons per second impinging on the sample is $1.6 \cdot 10^7$ ph/s. This number can be finally translated into SXR pulse energy considering the relation $E = h\nu N_{ph}$: the result is a pulse energy of $0.6\,\mathrm{pJ}$ at the sample plane, corresponding to a fluence of $84\,\mathrm{nJ/cm^2}$.

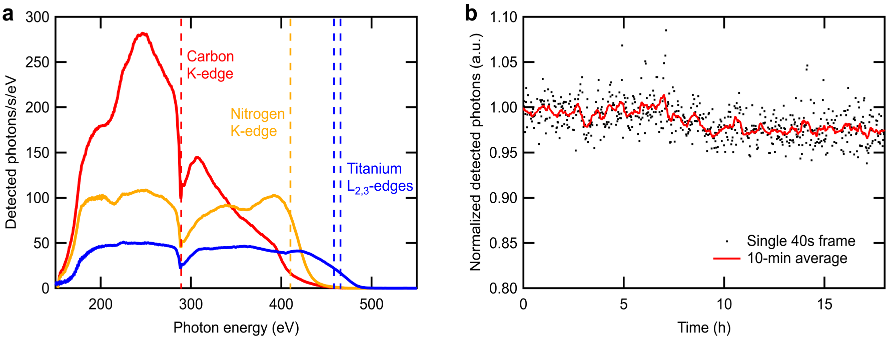

Figure 2.6: Flux and stability of the SXR source. a) The number of detected photons/s/eV is reported for spectra optimized for three different absorption edges, indicated on the figure. All spectra are taken with an aluminum filter and are the average of 15 spectra of 40 s integration time each. b) The long-term stability of the source is estimated calculating the variation of the total number of detected photons during one of the experimental campaign on graphite reported in Chap. 4.

One important feature that a light source must have for spectroscopic applications is stability. The capability to detect small signals, whatever is its nature, relies on the possibility to acquire data for long experimental times with a reproducible spectrum. The HHG process is non-linearly dependent on the laser intensity, resulting in amplification of any possible intensity fluctuations coming from the laser side. In addition, HHG spectral instability can also come from fluctuations of other parameters, like pressure or CEP. This is why we carefully monitor laser intensity, CEP and gas pressure while working with SXR beam. To evaluate the stability over the measurement time needed for experiments, one can consider the evolution of total detected SXR counts and define it as the long-term stability of the source; an example of such analysis is presented in Fig. 2.6b.

2.2.2 Spectral tunability across the water window

In the previous section, the setup to perform HHG has been presented, from the geometrical details of the generation up to the handling of the SXR radiation. Here the spectral characterization of the SXR source is reported, emphasizing the capability to tailor the spectrum according to experimental needs.

Besides the mutual alignment of laser beam and gas cell, the efficiency of the HHG process depends on its phase-matching condition, containing several contributions as indicated in [17, 18]. The relation for the phase-mismatch wavevector $\Delta k = k_{q\omega} - qk_{\omega}$ can be written as:

$$\begin{aligned} \Delta k &\approx q \cdot [\Delta k_{geo} + \Delta k_{disp}] + \Delta k_{dip}, && (2.1)\\ \Delta k_{geo} &= \nabla \Phi_{Gouy} = \nabla(-arctan(z/z_R)), && (2.2)\\ \Delta k_{disp} &\approx -P \cdot [(1-\eta) \cdot 2\pi \Delta n/\lambda_0 - \eta N_{atm} r_e \lambda_0], && (2.3)\\ \Delta k_{dip} &\approx -\nabla[U_P \cdot (t_r(q\omega) - t_b(q\omega))]. && (2.4) \end{aligned}$$

The geometric term Δk_{geo} is related to the Gouy phase term, which depends on the position along the propagation axis (here called z) and the Rayleigh length $z_R = \pi w_0^2/\lambda_0$, where w_0 is the beam radius at focus and λ_0 is the driving laser wavelength. The dispersive term Δk_{disp} depends on the gas pressure P, the ionization fraction η, the classical electron radius r_e, the density of atoms at atmospheric pressure N_{atm} and Δn, which is the refractive index change between the driving laser and harmonics wavelength. Finally, the dipole term Δk_{dip} depends on the ponderomotive energy of the driving laser field, U_P, and the electron times of birth t_b and recombination t_r for the HHG process.

The control of macroscopic parameters in the laboratory like the gas cell position z, the gas pressure P or the CEP, determining the electric field amplitude triggering the HHG process, is crucial to achieve phase-matching and generate the desired SXR flux. It is important to stress that these parameters are not totally uncorrelated: the desired HHG performances cannot be obtained by simply optimizing separately the variables one after the other. Nevertheless, it is interesting to observe how the spectrum depends on these quantities and how this can be used to tailor it according to the experiment. This being said, in the following section we present the single-variable dependence of the HHG spectrum on CEP, pressure and z position.

The dependence on the CEP is probably the most intuitive: changing the relative phase between the electric field and the pulse envelope translates in varying the electric field amplitude, with a periodicity of π. If the ionization gating scheme is used in combination with a few-cycle laser pulse, with the CEP we can move from a condition of isolated attoescond pulse emission to a train containing two pulses (see the Argon case in [52] for a clear example). The effect on the spectrum is known as half-cycle cutoff and it produces a strong modulation of the spectrum together with a shift of the cutoff energy, in our case up to 10%, as it can be observed in Fig. 2.7 or [27].

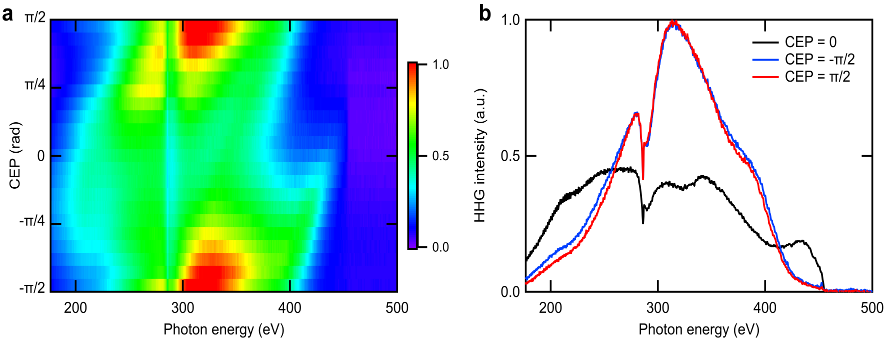

Figure 2.7: Impact of the CEP on HHG spectrum. a) SXR spectra generated in helium as function of CEP, each corresponding to 100 seconds integration time. The sharp cut above 450 eV is due to the L-edge of the titanium filter used for the measurement. The effect has a periodicity of π and allows to tune the HHG flux over a broad energy range, as clearly shown in b) where spectra for 3 extreme cases have been selected.

The gas pressure and the gas cell z-position are connected to microscopic quantities ruling the phase-matching of the process, as indicated in the equations above. Their effect on the generated spectrum is stronger than the one produced by the CEP, as it can be observed in Fig. 2.8. The pressure has in general a strong effect on the HHG flux and it usually presents a saturation point, i.e. a pressure value after which the flux decreases instead of increasing. On the other side, the dependence on the z-position mainly modifies the shape of the spectrum, which can be moved around the whole water window energy region. The combination of these two parameters allows a proper optimization of photon flux for a broad range of energies, hence for multiple spectroscopic applications.

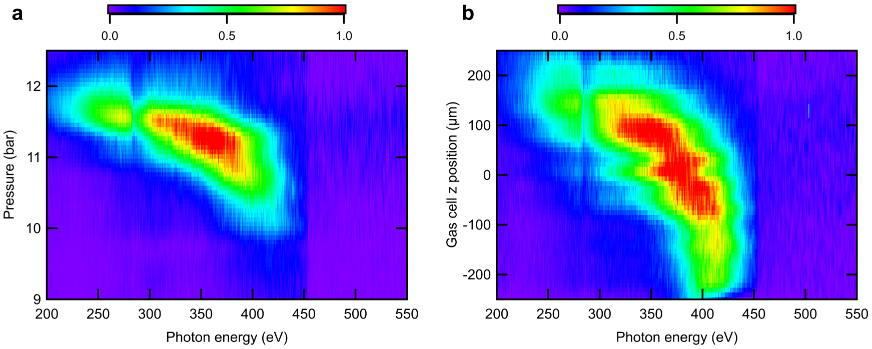

Figure 2.8: Spectral tunability of SXR spectrum with gas cell pressure and z position. In a) the z position is kept fixed while the pressure scanned, revealing a relatively narrow window in which phase-matching is achieved. b) If pressure is kept fixed and the gas cell moved along the beam propagation axis, the spectrum can be smoothly tuned from higher to lower energies. All spectra were recorded with 40 seconds integration time and a titanium filter to block the IR driver.

2.3 IR pump - SXR probe scheme

After describing in detail in the previous section the setup for generation, propagation, and detection of SXR attosecond pulses, here the propagation and characterization of a second laser beam is presented, which will constitute the pump pulse for all the pump-probe experiments here reported.

During my Ph.D., I worked with two different geometries for the pump-probe scheme. The collinear setup, using the same $1.85\,\mu$m exploited as driver pulse for HHG as a pump, has been exploited for the attosecond streaking experiment (2.4) and is presented in Sec. 2.3.1. The second implementation implies a small-angle non-collinear geometry and it has been used for the whole experimental campaign on graphite presented in 4.1. For this second setup, the $1.85\,\mu$m pulse or its second harmonic constitute the pump pulse, respectively reported in Sec. 2.3.1 and 2.3.2.

For both the different geometries used, the setup consists of a Mach-Zender interferometer, starting at the beginning of the beamline with a beam splitter whose transmission always constitutes the HHG laser driver while its reflection is arranged to be the pump pulse. The recombination of pump and probe takes place further along the beamline, either in the mirror or directly the experimental chamber, as it will be shown in the next sections.

2.3.1 CEP-stable, $1.85\,\mu$m pump

Two different experiments have been carried out with the pump pulse being a replica of the CEP-stable, $1.85\,\mu$m laser pulse used for HHG driver: attosecond streaking (2.4) and time-resolved XAFS (4.1). Due to the different detection scheme, two different geometries have been implemented for these experiments, with pros and cons that will be described in this section.

For the attosecond streaking experiment, the commonly used collinear setup was chosen, represented in Fig. 2.9. The first optical element in the chamber is the beamsplitter, which constitutes the beginning of a Mach-Zender interferometer where the pump and probe beams follow the two separate arms. The pump beam is first sent to the delay-line stage, used to control and scan the time delay between the two pulses, then propagated up to the mirror chamber (with the least amount of optics to reduce losses). At the end of this chamber, the two beams recombine with the use of a 45^o holey-mirror (2 mm hole size). The pump beam, after hitting a concave mirror used for focusing the beam on the sample, is reflected by the holey-mirror, being perfectly centered respect to the hole. The SXR beam instead simply propagates through the hole, where the small divergence of these wavelengths ensures having no beam clipping. After the holey-mirror, the two beams co-propagate up to the sample, which in this case is a gas (Krypton, see Sec. 2.4) streaming out of a metallic nozzle.

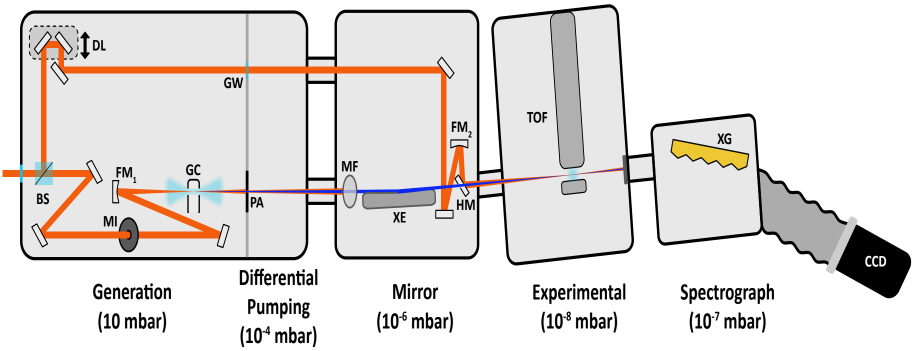

Figure 2.9: Collinear scheme for $1.85\,\mu$m pump - SXR probe, used for the attosecond streaking experiment. The reflection of the beam splitter (BS) constitutes the pump beam, synchronized with the probe by means of a delay-line stage (DL). The pump beam is propagated up to mirror chamber, where it is reflected by the focusing mirror (FM$_2$) and finally by the holey mirror (HM), where it recombines with the SXR beam. Both beams travel together up to the interaction region, where the photoelectrons are detected by a time-of-flight (TOF) spectrometer.

The main advantage of this setup is that, once the collinearity is ensured over a distance at least as large as the beam path between the holey mirror and the sample, the result is a perfect spatial overlap and the absence of any temporal smearing effect coming from the angle between the two beams. On the other hand, using the holey-mirror to reflect the pump produces two main undesired effects: the first is that the central (most energetic) part of the beam is lost in the hole, reducing consistently the pump pulse energy, which can be critical for experiment like streaking where pump intensity is a key parameter for a good characterization. The second is that the reflected beam has a doughnut shape in the far-field, which can limit the spot size at focus and add spatial aberrations.

For pump-probe spectroscopy, any detected signal not related to the probe, as the background signal coming from the pump, constitutes contamination that has to be reduced to the minimum possible. For the case of streaking, for the intensity achieved on the pump pulse (on the order of $10^{11}\,\mathrm{W/cm^2}$), the photoelectron detection always turned out to be pump-background-free.

When switching to time-resolved XAFS measurements, where the transmitted SXR spectrum is detected on the cooled CCD camera, the suppression of pump background (scattered pump photons hitting the camera) turned out to be more complicated. Even the insertion of movable slits and an additional metallic filter was not enough to shield the camera from undesired pump light, with the effect becoming worse when moving the pump central wavelength towards the visible (because of the higher sensitivity of the silicon detector). This constitutes the main reason behind the choice of a non-collinear setup.

For this scheme (see Fig. 2.10), a 90-degree periscope is inserted at the beginning to flip the polarization from p to s (related to experiment in graphite, presented in 4). After the delay-line stage, the beam enters a reflective telescope, which doubles the beam size and provides a focus along the way, exploited for the $0.8\,\mu$m pump case as explained in the next section. The beam then propagates up to the mirror chamber where a thin CaF_2 lens (f=500 mm) is used as a focusing element and the last mirror, slightly displaced respect to the SXR beam path, steers the beam to achieve spatial overlap directly at the sample plane in the experimental chamber, where the interferometer is closed. The angle between pump and probe is the minimum possible given the beam sizes and amounts to $1.5^o \pm 0.5^o$.

Thanks to this angle, at the end of the experimental chamber the beams are separated enough in the horizontal plane such that the combination of a movable slit and a metallic filter reduces the pump background almost to zero, which allowed us to perform experiments with high pump intensity. The drawback is the presence of the effect of temporal smearing introduced by the angle which could wash out fast dynamics in a pump-probe experiments. For our experimental conditions, considering the measured FWHM beam sizes for pump ($D = 50\,\mu$m) and probe ($d = 12\,\mu$m), the induced temporal smearing can be estimated according to the formula

$$t_{smear} \simeq \frac{d sin\alpha}{c} = \frac{(12 \cdot 10^{-6}) \cdot (sin 1.5^o)}{(3 \cdot 10^8)} \approx 1fs. \tag{2.5}$$

The estimation provided by the formula can be considered as the worse case scenario for linear interaction of the pump pulse with the sample, while the case of nonlinear interactions would relax this condition. The temporal and spectral characterization of the pump pulse for both schemes is presented in Fig. 2.11. The spectrum is slightly modified respect to the one used for HHG, due to the

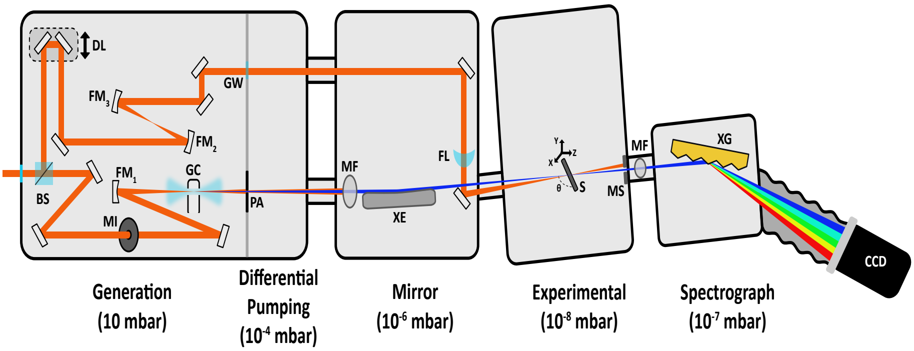

Figure 2.10: Non-collinear scheme for $1.85\,\mu$m pump - SXR probe, used for time-resolved XAFS experiments. In contrast to the collinear case, the pump beam is expanded with a telescope (FM_2 and FM_3) and then focused with a lens (FL) into the experimental chamber, where it recombines with the SXR directly on the sample. After the interaction, a movable slit (MS) and a metallic filter (MF) are used to shield the spectrograph from residual pump light.

coating of the different optics used. The pulse duration changes from 11.2 to 12.5 fs, difference due to the propagation of the pump pulse through thin pieces of CaF_2 glass, i.e. a window between generation and differential pumping chamber and the focusing lens.

2.3.2 CEP-stable, $0.8\,\mu$m pump

In time-resolved spectroscopy, a common practice is to vary pump pulse parameters (i.e. pulse intensity, photon energy, etc.) and study their influence on the observed dynamics. With the aim of adding tunability to the pump wavelength, a second-harmonic generation (SHG) stage was designed and implemented to be inserted into the path, at will, as reported in Fig. 2.12.

There are only a few differences with respect to the $1.85\,\mu$m pump case. In between the expanding telescope constituted by FM_2 and FM_3, a BBO crystal ($200\,\mu$m thickness) near the focus is used to generate the second harmonic of the $1.85\,\mu$m pulse, then two dichroic mirrors are used in reflection to separate the SH from the fundamental. The phase-matching condition of the SH process

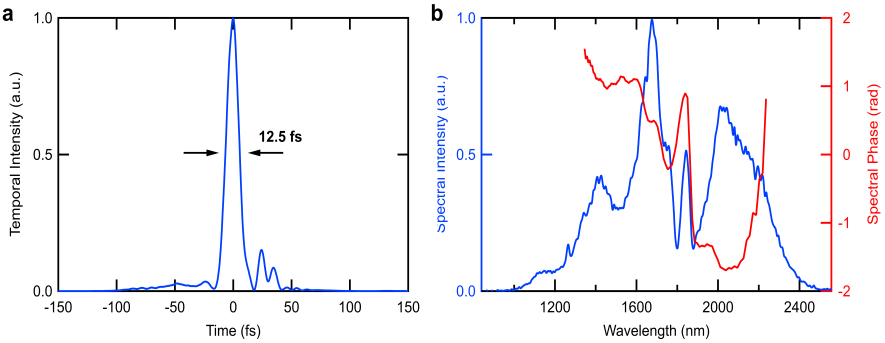

Figure 2.11: Temporal (a) and spectral (b) characterization of the 1.85 μm pump pulse. Due to the propagation along the beamline, the pump pulse results to be slightly longer than the HHG driver, shown in Fig. 2.2.

has been tuned to maximize the SH pulse energy, resulting in the spectrum presented in Fig. 2.13. Instead of the initial periscope, a waveplate is used after the dichroic mirrors to make sure the beam is s-polarized.

To compensate the dispersion added by the BBO crystal and the waveplate, a pair of chirped mirrors (Layertec, $-40\,\text{fs}^2$/reflection) is used, with four total reflections, to achieve a final pulse duration of 15 fs (see Fig. 2.13). Finally, the focusing lens used for the 1.85 μm pump beam path is replaced with a 15^o, silver-coated, off-axis parabola (f=500 mm, Edmund Optics), because of the higher dispersion provided by the CaF_2 lens for these wavelengths compared to the 1.85 μm case.

2.3.3 Spatio-temporal overlap

In this section, the protocol to ensure the spatio-temporal overlap of pump and probe is presented, distinguishing the two different cases of attosecond streaking and time-resolved XAFS experiments. To detect the overlap of two beams of very different wavelength (μm vs. nm scale) and intensities (μJ vs. pJ level) can be challenging and, in this case, it should take place completely in vacuum. It is for this reason that to verify the spatio-temporal overlap, the SXR beam is replaced by the remaining IR driver transmitted along the beamline in absence

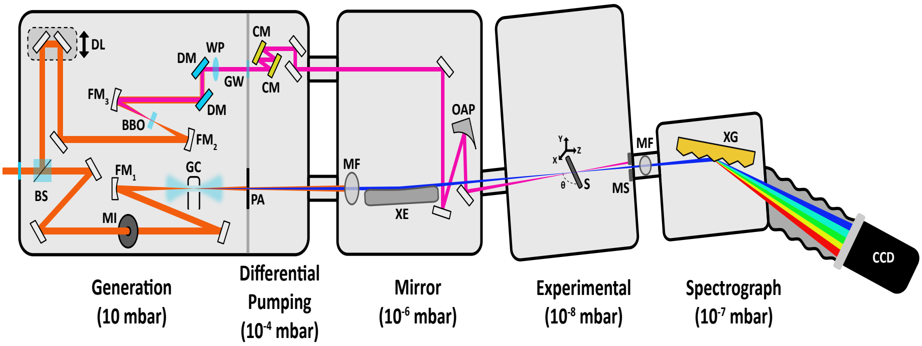

Figure 2.12: Non-collinear scheme for $0.8\,\mu$m pump - SXR probe, used for time-resolved XAFS experiments. The telescope placed in the generation chamber produces a focus used for SHG in a BBO crystal, which component is isolated by means of dichroic mirrors (DMs). Polarization is set by a waveplate (WP) and pulse is again compressed with 4 bounces on chirped mirrors (CMs). Finally, an off-axis parabolic mirror (OAP) replaces the lens as focusing element before the recombination with the SXR probe.

of metallic filters on the probe path.

For the case of attosecond streaking, collinearity between the two beams needs to be enforced. Using a movable pick-off mirror placed after the gas nozzle, the two IR beams are sent outside the vacuum chamber through a glass window to a home-built imaging system. With the help of an IR beam profiler (WincamD, DataRay) and moving two motorized mirrors placed along the pump beam path, the collinearity of the two beams is established. The coarse temporal overlap is obtained via spectral and spatial linear interferometry between the two beams. For higher resolution overlap detection, the available intensities for both IR pulses ($10^{10} - 10^{11}\,\mathrm{W/cm^2}$) don't allow using strong-field ionization-based cross-correlation methods on a gas target. For this reason, photoemission-based in-situ IR-IR cross-correlation on the metallic nozzle is rather used, recording photoelectron spectra with the TOF electron spectrometer as a function of the time delay, ensuring the zero delay determination with sub-fs precision. Even if the photoelectron signals produced by the two IR beams have very different amplitudes, the cross-correlation trace exhibit high-visibility fringes (see Fig.

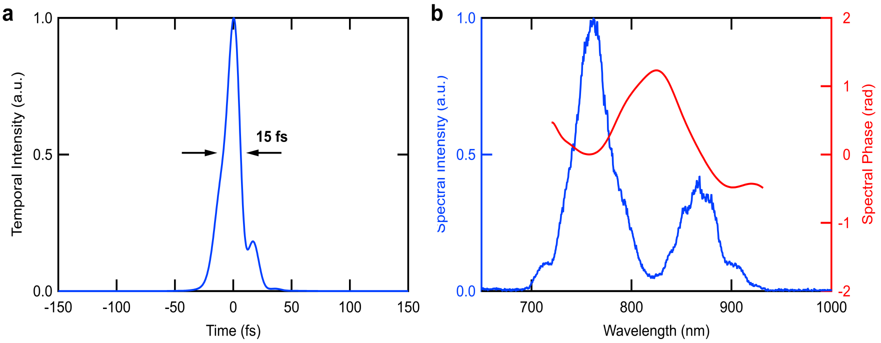

Figure 2.13: Temporal (a) and spectral (b) characterization of the 0.8 μm pump pulse. Optimizing SHG for pulse energy produces a double-peak spectrum with a center-of-mass wavelength around 0.8 μm.

2.14 below) and ensure the presence of spatio-temporal overlap at the exact plane where the experiment will take place. The delay stage position for which the maximum cross-correlation signal is obtained is considered as the time zero for the experiment.

For the time-resolved XAFS measurements, the non-collinear setup required a different approach. The spatial overlap needs to be verified at the exact plane of the sample we want to probe because any offset would translate in a temporal shift of the overlap position. For this reason, on the same sample holder where the target is mounted a 50 μm nickel pinhole and a thin BBO crystal (20 μm) are placed. The pinhole is used to get spatial overlap: it is centered on the SXR beam after signal optimization and, by means of motorized mirrors, the pump beam is steered to have maximum transmission through it. Finally, the two IR beams are sent to the BBO and, thanks to the non-collinear angle, the sum-frequency generation (SFG) signal between the pump and probe is detected in the imaging system. Again, this cross-correlation signal is recorded, the profile is fitted with a Lorentzian function and the delay value corresponding to the center of the Lorentzian distribution is chosen as time zero for the experiment (see Fig. 2.14).

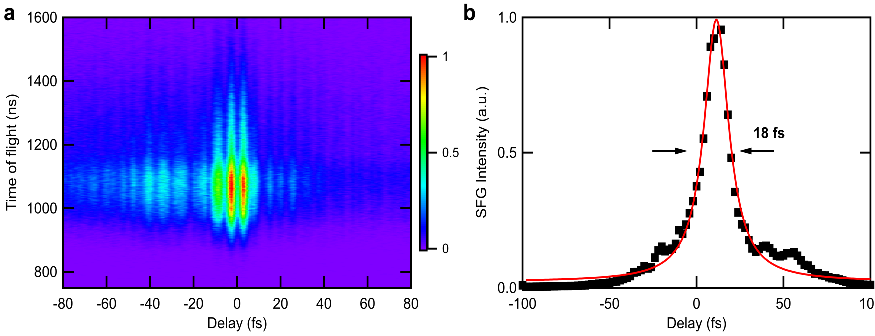

Figure 2.14: Detection of spatio-temporal overlap for the two different experiment of streaking and time-resolved XAFS. a) For the case of the cross-correlation between IR pump and IR probe on the needle tip, time zero for the experiment is chosen as the delay value showing the stronger modulation (here corresponding to the minimum between the two peaks). b) The obtained SFG signal is fitted with a Lorentzian, which center is chosen as time zero for the experiment.

2.4 Temporal characterization: Attosecond Streaking

In Sec. 1.1.2 the general approach used in attoscience for temporal characterization of IAP was introduced, namely the attosecond streaking technique. The experimental setup realized to perform such a measurement is presented in Sec. 2.3, while here the results are reported.

It is interesting to observe that at the time the measurement was performed (2014/2015), while the technique was well established in the attoscience community for XUV photon energies, no temporal characterization was reported for attosecond pulses in the SXR region. At present, the work still constitutes the experimental proof of IAP with the highest average photon energy (bandwidth centered around the carbon K-edge at 284 eV) ever reported [52], even if other works have been published later showing spectra reaching the SXR region [28, 53]. For the two mentioned cases, pulse durations around 50 as have been extracted with retrieval algorithms (PROOF for [28], a modified version of FROGCRAB for [53]). However, a recent publication highlighted inaccuracies of these methods for applications to broadband SXR attosecond pulses [132].

Attosecond streaking experiments in the SXR region become more complicated due to a number of factors (compared to the XUV case, see [52, 132]) like:

- HHG flux for sources operating at SXR photon energies is generally lower compared to the XUV energy range; same applies for photoionization cross-sections in this energy range, which are at least one order of magnitude lower compared to the XUV case, resulting in considerably longer integration times for data acquisition;
- difficulty in finding for the whole IAP bandwidth a gas target which photoelectrons are coming (mainly) from a single orbital to constitute a replica of the photon spectrum. Helium would solve the problem, but presents a very low ionization cross-section compared to other gases;
- a longer optical cycle (and pulse duration) for the IR driver compared to the 800 nm case, extending the time delay range needed for the measurement.

For the spectrum obtained with HHG in Neon (see Fig. 2.15a), the best gas target to generate the photoelectron replica of the spectrum turned out to be Krypton. Its ionization cross-section in the energy range of interest shows a 3d shell contribution at least one order of magnitude higher than the other ones. The detection gas streams out of a gas nozzle placed at the center of the experimental chamber and aligned respect to the beams and to a TOF spectrometer (Stefan Kaesdorf) used to detect the photoelectrons. Spatio-temporal overlap between the pulses is detected using the leftover IR driver from the HHG process instead of the SXR pulse, using an IR-IR cross-correlation method as described in Sec. 2.3.3. Combination of several filters and analysis of the photoion spectrum has been used to ensure the nature of the photoelectron signal, excluding any contamination from secondary emissions (e.g. Auger processes).

The recorded streaking trace is shown in Fig. 2.15. Step size for the delay axis is 600 *as* and integration time per each spectrum is 10 minutes, resulting in a total acquisition time of about 10 hours over which high spectral and CEP stability are required. The IR streaking intensity corresponds to $3.2 \cdot 10^{11}\,\mathrm{W/cm^2}$, which translates into a electric field amplitude of $0.15\,\mathrm{V/Å}$ and a ponderomotive energy of 0.1 eV (spectral and temporal information are indicated in Fig.

2.10). Clearly visible is the modulation due to the presence of the IR field, able to shift the spectrum of about 50 eV moving from a maximum to a minimum of the vector potential. The absence of any spectral modulation and of any contribution delayed in time by half a period (like in the case of HHG in Argon, shown in [52]) allows us to conclude that the SXR pulses are isolated.

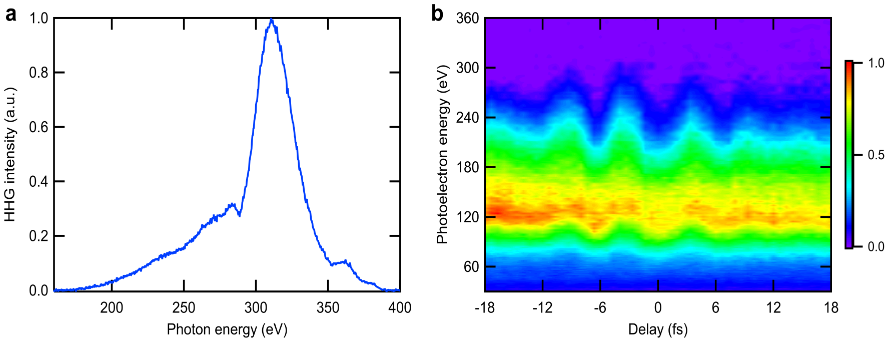

Figure 2.15: Attosecond streaking characterization of water-window IAP. The spectrum of HHG in Neon is shown in a), where the center-of-mass of the spectrum lies above the carbon K-edge. b) Measured streaking trace, where the photoelectron spectrum is modulated by the presence of the IR laser field (the shift is proportional to the square of the laser vector potential).

For the reconstruction of the SXR electric field, several attempts have been made with different retrieval algorithms: FROGCRAB, PROOF, Ptychography. Here the results obtained with FROGCRAB are discussed, but the same problems have been found in the analysis using the other methods. The FROGCRAB algorithm [48] has been used, as for the most of the streaking experiments found in literature, conscious about the fact that it was never tested on broadband SXR attosecond pulses. The reconstruction, no matter which interpolation or filtering method is used, always returns a pulse duration of $20-25$ as, very close to the Fourier transform limit of the spectrum of 15 as [52]. To explain such short pulse duration, some phase compensation mechanism must take place to reduce the intrinsic spectral phase coming from the HHG process itself, known as attochirp. For this reason, all the possible sources of phase have been evaluated (see [52] for more details), but none of them is comparable to the semi-classical estimation of the attochirp for our condition of 2500 as^2. This spectral phase, applied to the spectrum, would produce a pulse with a duration of about 320 as. We conclude that the solution of the retrieval is not robust, a consequence of the limitations of the algorithm for these experimental conditions.

To test the capabilities of the FROGCRAB method for the reconstruction of broadband SXR pulses, we turned to numerical simulations. Through the use of the definition of the spectrogram, based on the so-called strong-field approximation [48], it is possible to simulate streaking traces and then use the algorithm to retrieve the simulated complex SXR electric field. The main results of this numerical investigation are:

- The streaking intensity used ($3.2 \cdot 10^{11}$ W/cm^2) is too low for the bandwidth of our pulse, for which only values above $1 \cdot 10^{12}$ W/cm^2 are able to return a sensible number for the pulse duration.

- At a given streaking intensity, the accuracy of the retrieval lowers for increasing bandwidth (for intensities on the order of 10^{11} W/cm^2 the retrieval starts to deviate for bandwidth above 60 eV, considerably far from the $\sim$ 150 eV bandwidth of our SXR pulse). This is a consequence of the central-momentum approximation, for which the central energy must be larger than the bandwidth, which doesn't apply to our case (central energy of 250 eV is comparable to the bandwidth of 150 eV).

- Low signal-to-noise ratio (limited by the long integration time) and finite energy resolution (related to the instrumental resolution of the TOF spectrometer and connected to the temporal resolution by the sampling criterion $\delta\tau\delta E = \frac{2\pi\hbar}{eN}$, with N number of points) contribute to lowering the accuracy of the reconstruction.

During the last year, a new retrieval algorithm has been introduced by the group of prof. C.D. Lin [132]. To prove its improved accuracy compared to other existing methods, the new retrieval algorithm has been tested with our streaking measurement and the other two experiments reported for SXR pulses [28, 53]. The main difference with respect to the other methods relies in the verification of the goodness of the guessed solution: the algorithm doesn't try to minimize the differences between the spectrograms $S(E,\tau)$ but it rather compares their autocorrelation, defined as $Q(\tau_1,\tau_2) = \int_0^\infty S(E,\tau_1)S(E,\tau_2)dE$. They showed how this quantity is more sensitive to the spectral phase all over the bandwidth, resulting in a more accurate retrieval of the spectral phase for broadband SXR pulses. The application of this new method to our measurement assigned a pulse duration of 165 as to the SXR pulse generated in Neon.

This new algorithm opens new possibilities for attosecond pulse characterization even for the extreme conditions of our ultrabroad spectra. Improving the detection of photoelectron spectra to increase energy resolution and detection efficiency, increasing streaking intensity by means of different focusing geometry or simply higher laser output, together with the application of this new algorithm, will make the characterization of the HHG radiation reliable and feasible on reasonable timescales even for lower HHG flux, like in the case of generation in Helium.

2.5 Conclusions

A complete setup for the realization of femtosecond IR pump - attosecond SXR probe transient absorption (TA) spectroscopy experiments has been presented in this chapter, constituting the experimental tool allowing the time-resolved investigations presented in this thesis. A home-built laser system consisting of a high-pulse energy Ti:Sa-based laser source and an OPA stage for frequency down-conversion with final pulse-compression stage delivers sub-two-cycle (11.2 fs), CEP-stable, 0.5 mJ laser pulses centered at 1.85 μm. These pulses enter a series of vacuum chambers called Attosecond Beamline, where they are split into two replicas by means of a beam splitter to constitute the pump and probe beam, recombining at the end of the interferometer on the experimental target.

Isolated attosecond SXR pulses are generated by extreme frequency up-conversion of the IR pulse via HHG and constitute the probe of the experimental setup. By tightly focusing the IR beam in a semi-infinite gas cell at high gas pressures of helium ($\sim$ 10 bar), the HHG process is driven in ionization gating conditions, efficiently producing a single attosecond burst per each laser shot. The SXR contribution to the HHG emission is separated from the co-propagating remaining IR driver with a metallic filter, after which an ellipsoidal mirror focuses the SXR beam in the experimental chamber. The transmitted SXR light is dispersed with an X-ray reflective grating and collected by an X-ray CCD camera.

The spectrum of the attosecond SXR pulses spans over the entire water window region ($284 - 543\,\mathrm{eV}$), allowing the coverage of different absorption edges, as presented in Chap. 3. Flux and spectral bandwidth can be highly tuned by controlling macroscopic parameters like gas pressure, gas cell position or laser CEP, directly affecting the phase-matching conditions at a microscopic level. The flux delivered on the experimental target is on the order of $10^7\,\mathrm{ph/s}$ and great spectral stability has been shown on a timescale of several hours.

Different implementations of the pump-probe scheme have been presented, according to different experimental requests. The non-collinear setup, used for TA measurements, has been reported, providing the possibility to use the same $1.85\,\mu\mathrm{m}$ pulse or its SH as pump pulse, hence offering tunability of the excitation photon energy. The collinear setup has instead been exploited to perform an attosecond streaking experiment, aiming at characterizing the HHG emission in the time domain. The experiment revealed the emission of a single attosecond pulse, with a duration of 165 as retrieved by means of reconstruction algorithms.

Chapter 3

Attosecond X-ray absorption fine structure spectroscopy

In this chapter, the well-established experimental technique of X-ray absorption fine-structure (XAFS) spectroscopy is presented. The basic principles of XAFS are explained and its implementation on a table-top attosecond source is described, discussing its capabilities with a presentation of the latest results.

A general presentation of the technique is reported in Sec. 3.1. Starting from its fundamentals, the spectroscopic capabilities of XAFS are described and a discussion on the available sources suitable for such applications is reported. In detail, a description of how the technique can provide information on the electronic (3.1.1) and lattice (3.1.2) structure of the probed material is presented.

In Sec. 3.2 the results of XAFS investigation of a graphite thin flake with the SXR attosecond light source are presented. The simultaneous access to electronic and lattice degree of freedom with unprecedented temporal resolution is reported.

The XAFS characterization of the graphite samples studied in this thesis is presented in Sec. 3.3. Samples are first evaluated in terms of previous results achieved in graphite, then compared with experimental data collected at a synchrotron light facility.

Finally, a numerical approach to model XAFS spectra based on density-functional-theory (DFT) calculations is presented in Sec. 3.4.

3.1 Introduction to XAFS

X-ray absorption fine-structure spectroscopy is a powerful technique providing information on the electronic, lattice and chemical structure of the measured target with atomic resolution [133, 134, 135]. All its properties are a direct consequence of the light-matter interaction taking place when X-ray photons are absorbed by the target, described by the photoelectric effect [136]. Given E_0 the binding energy of the electron in a certain energy state, the X-ray photon can be absorbed by the material allowing an electronic transition to continuum states if its energy E_{ph} is higher than the electron binding energy, $E_{ph} \geq E_0$. The emitted electron (usually referred to as a photoelectron) propagates with a wave-vector described by the formula

$$k = \frac{1}{\hbar}\sqrt{2m_e(E_{ph} - E_0)}, \tag{3.1}$$

where m_e is the electron mass and $\hbar$ is the reduced Planck constant. For photon energies approaching the electron binding energy, the absorption of X-ray light in the material experiences a sharp rise called absorption edge.

Photoemission of electrons to the continuum is not the only possible result of the interaction of X-ray light with matter. For photon energies close to the absorption edge, electronic transitions to unoccupied bound states of the system (conduction bands (CBs) for solids, excited states for atoms/molecules) are possible, if allowed by the selection rules. The analysis of the spectral region close the absorption edge provides then information on the electronic structure of the material and is called XANES (X-ray absorption near-edge structure, see 3.1.1) [137, 138]. The part of the absorption spectrum corresponding to electronic transitions to the continuum is called EXAFS (Extended X-ray absorption fine-structure): the analysis of this region provides instead information on the lattice structure, as described in Sec. 3.1.2 [139, 133].

The interaction of X-ray radiation with the material is ruled by the Beer-Lambert equation:

$$I(E) = I_0(E)e^{-\mu(E)\cdot x}, \tag{3.2}$$

where $I_0(E)$ and $I(E)$ are respectively the incident and transmitted intensity at the photon energy E, $\mu(E)$ is the absorption coefficient of the material and x its thickness. The absorption coefficient is a function of the photon energy E and presents a sharp rise for each energy corresponding to electronic transitions from inner shell levels to first unoccupied bound states, as described before. In the X-ray range, the photon energy is comparable to the energy of the inner electronic shells of the materials (1s, 2p, s2, etc...). These energy levels are characteristic of the probed material, being it a solid or a molecule, and do not strongly depend on the chemical composition as the outer valence shells. Absorption edges related to transitions from the 1s inner shell are called K-edges, while L-edges refer to 2s/2p inner shell, M-edges refer to 3s/3p/3d and so on. Because of this property of being sensitive to energetic fingerprints of the material, XAFS spectroscopy is defined as element-specific technique.

The implementation of XAFS spectroscopy implies the use of an X-ray source, which availability was limited mainly to large-scale facilities until about a decade ago. At synchrotron radiation facilities monochromatic X-ray sources of high brightness and excellent spectral stability are available to perform high-quality XAFS investigations [140, 141]. Drawbacks for these sources are the need for energy scanning (increasing the acquisition time and sometimes requiring concatenation of different spectra for simultaneous XANES/EXAFS analysis) and the temporal resolution, which is on the order of hundreds of femtoseconds for slicing sources [142], hence limiting its application to ultrafast spectroscopy. Nowadays shorter X-ray pulses with even higher brilliance can be obtained at Free-Electron Lasers (FELs), where pulse durations on the order of few-fs have been demonstrated (although for limited ranges of photon energies) [143, 144, 145]. The extraordinarily high number of photons per laser shot obtained at FEL sources allows to study light-matter interaction in the extreme non-linear regime but can also constitute a limit to the number of spectroscopic applications for these type of light sources (they are not suitable to study matter in an almost-unperturbed ground state). On the other side, the main limitation comes from the intrinsic nature of FEL X-ray pulses, which are originated from spontaneous emissions, hence lacking shot-to-shot reproducibility (some seeded cases with higher reproducibility are available but not for the whole X-ray spectral range [146, 147]). Finally, a common feature for both these type of sources (FEL and synchrotron) is their large-scale dimensions: there are only a limited amount of synchrotron and FEL sources nowadays and the access to the beamlines requires acceptance of beam-time requests, which can be challenging.

Large-scale facilities like FEL and synchrotron sources are not the only available option to generate X-ray light. One option to produce this radiation from a table-top source is to implement a plasma-based X-ray source: the X-ray radiation is produced by focusing a high-intensity laser onto a solid-state target in vacuum, producing a high density of electrons through photoemission. The electrons, accelerated by the electric field carried by the same laser pulse, penetrate inside the material, generating both X-ray continuum and emission lines [148]. However, the duration of this radiation is always confined to the picosecond-nanosecond regime, hence still not suitable for ultrafast spectroscopy.

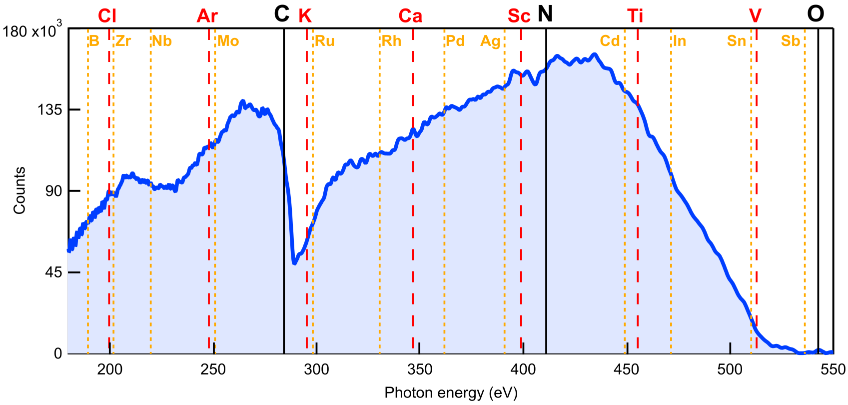

Figure 3.1: Measured SXR spectrum generated via HHG in Helium spanning over the water window region ($284-543$ eV). The spectrum is the average of 10 spectra, each one obtained with 60 s integration time. Reported on the figure are some of the absorption edges covered by the bandwidth of the SXR pulse: the solid black lines correspond to K-edges, the red dashed lines correspond to L-edges, the yellow dashed lines correspond to M-edges. For edges presenting spin-orbit splitting (as in the case of L- and M-edges), the line sits at an energy corresponding to the average between the different edges. Data for absorption edges are taken from [149].

Finally, the implementation of a table-top high-harmonic-generation (HHG) setup with SWIR-wavelength laser driver as the one described in Chap. 2 is, to date, the only available possibility to generate ultrashort ($<$ fs), high-coherence SXR pulses for XAFS applications with possible synchronization to a second laser pulse on the sub-fs timescale. The generated flux is several orders of magnitude lower than all the other mentioned sources and the emitted radiation only spans the SXR region, reaching a maximum of 1 keV, with an efficiency decreasing for increasing photon energy [21]. On the other hand, XAFS spectroscopy has already been demonstrated with this type of sources, as in the case of the pioneering works of our group [25, 150], and the temporal resolution of the attosecond SXR pulses has already been applied to several studies of electron dynamics, as presented in Sec. 1.1.2 [82, 29, 83]. The broadband spectrum produced by HHG in these conditions, as the one reported in Fig. 3.1, allows the simultaneous coverage of several absorption edges, offering a wide variety of possibilities for XAFS spectroscopy. These properties make the HHG-based SXR sources unique for application to ultrafast spectroscopy of electron and lattice dynamics, as will be shown in 3.2, 4.1 and 4.2.

3.1.1 XANES - probing electronic structure

In Fig. 3.1, the HHG spectrum generated in Helium is presented together with some of the absorption edges covered by the attosecond SXR radiation. Beside the K-edges of Carbon, Nitrogen and Oxygen, considered as the building blocks of most of the biological compounds, we find several L-edges (like Titanium, Vanadium, Chlorine, Argon, etc...) and M-edges (Boron, Zirconium, Molybdenum, Silver, etc...) which offer a wide variety of possibilities for XAFS spectroscopy. For each absorption edge, electronic transitions from inner shells to bound electronic states induced by absorption of X-ray photons (XANES spectrum) follow Fermi's golden rule

$$\Gamma_{i\to f} = \frac{2\pi}{\hbar} \left|\langle f|H'|i\rangle\right|^2 \rho(E_f), \tag{3.3}$$

where $\Gamma_{i\to f}$ is the transition probability from initial state i to final state f, H' is the perturbation inducing the transition and $\rho(E_f)$ is the density of states at the energy E_f of the final state. In the dipole approximation, the operator H' can be written as $H' = -e\vec{E}\cdot\vec{d}$, where e is the electron charge, $\vec{E}$ is the electric field carried by the X-ray laser pulse and $\vec{d}$ is the dipole moment of the sample. The scalar product between these two last quantities sets the so-called selection rules, consisting of a relation between the laser polarization and the symmetry of the initial and final electronic states. The transition probability hence depends on the character of the orbitals/bands involved, making XANES spectroscopy an orbital-selective technique.

The analysis of the XANES spectrum allows detecting quantitatively the chemical composition of the material, wherever the spectral resolution of the spectrometer permits to resolve the chemical shifts. In a publication of some years ago [25] my group showed the possibility to perform XANES spectroscopy of an organic compound (polyimide thin film) at the carbon K-edge, resolving the features relative to all the different chemical bonds involving carbon atoms. For solid-state samples, the XANES spectrum provides instead a quantitative measurement of the unoccupied density of states (DOS) of the material to which transitions are allowed. In Sec. 3.4 a model to reproduce the XAFS spectra based on the DOS is presented.

To extract meaningful information about the probed material, XAFS spectroscopy sets a requirement on the concentration of the sample, both for gas-phase and solid-state targets. The concentration has to be enough to have efficient interaction with the X-ray photons, but without heavily reducing the number of transmitted photons detected by the spectrometer. For spectroscopy studies of a single absorption edge, the general rule for the sample concentration is to choose a thickness equal to one absorption length, meant as the length after which the intensity drops by a factor $1/e$. Clear examples of XANES spectra are reported in 3.2 and 3.3.

3.1.2 EXAFS - probing lattice structure

As anticipated in Sec. 3.1, EXAFS usually refers to the region of the absorption spectrum several tens (hundreds) of eV above the edge corresponding to electronic transitions from inner shell states to the continuum. During the photoemission process, the electrons interact with the electron clouds around the surrounding atoms because of Coulomb interaction and eventually return to the absorbing atom, acting as a perturbation of the local electron density. The spherical wave associated with the emitted electron can interfere constructively or destructively with the electron density at each position corresponding to neighboring atoms, traveling for an average distance corresponding to the photoelectron mean-free-path.

The interference is reflected in the absorption spectrum as spectral modulations depending on the distance of the nearest neighbors. The interference pattern is described by the so-called EXAFS equation [133]:

$$\chi(k) = S_0^2 \sum_j N_j f_j(Rj,k) \frac{e^{-2\sigma_j^2 k^2} e^{-\frac{2R_j}{\lambda_{ej}(k)}}}{kR_j^2} sin(2kR_j + \delta_j(k)), \tag{3.4}$$

where S_0 is the probability of scattering from the absorbing atom while j is an index referring to the surrounding atoms; N_j is the number of scattering atoms in the jth shell, positioned at a mean distance R_j from the absorbing atom; $f_j(Rj,k)$ is the scattering amplitude function for the jth shell. The term $e^{-2\sigma_j^2 k^2}$ is the Debye-Waller factor accounting for damping due to static and thermal disorder in absorber-backscatterer distances σ_j. The term $e^{-\frac{2R_j}{\lambda_{ej}(k)}}$ considers losses due to inelastic scattering, with $\lambda_{ej}(k)$ being the electron mean-free-path. The oscillations in the EXAFS spectrum are reflected in the sinusoidal term $sin(2kR_j + \delta_j(k))$, where $\delta_j(k)$ is the scattering phase function for shell j. This sinusoidal term shows the direct relation between the frequency of the EXAFS oscillations in k-space and the absorber-backscatterer distance.

It is possible to extract information about the distances of the first nearest neighbors and their coordination numbers applying the EXAFS equation to the experimental data. The EXAFS signal, through the use of well-established software in the community like Athena and Arthemis [151], is obtained by the absorption spectrum after a spline polynomial removal, normalization to the edge jump and conversion from energy to wave-vector values. Scattering and phase amplitudes can be estimated with ab initio calculations [152]. Finally, a windowed Fourier transform is applied to the spectrum to retrieve the lattice distance from the position of the peaks in the Fourier spectrum. Application of EXAFS analysis to a solid-state target is reported in the next section.

3.2 Attosecond XAFS in graphite

In a work published by our group in 2018 [150], the application of the XAFS technique using SXR attosecond pulses to simultaneously identify the electronic and lattice structure of a solid-state target was demonstrated for the first time. With the analysis of both the XANES and EXAFS region of the absorption spectrum, the study exploits the extreme bandwidth of isolated SXR attosecond pulses to access the electronic and lattice parameters of a highly-oriented pyrolitic graphite (HOPG) film. In this section, a summary of the results is presented.

Graphite is a well-studied material because of its unique optical, electronic and thermal properties, originating from a peculiar crystalline structure consisting of a vertical series of one-dimensional layers (called graphene) arranged in hexagonal cells of carbon atoms, as reported in Fig. 3.2b. The sp^2 hybridization of carbon's atomic orbitals produces strong covalent bonds (called σ) in a planar configuration, distributed in hexagonal structure, while the remaining p-like orbital (called π) is oriented perpendicularly to the graphene layer and is responsible for the weak van der Waals force keeping the different layers together. The electronic band structure resulting from such lattice geometry and atomic electronic configuration is reported in Fig. 3.2a: the top of the valence band (VB), predominantly of π character, exhibits an almost-linear dispersion and is separated from the bottom of the conduction, with main π^* contribution, by a small energy band-gap of $\sim 40\,\mathrm{meV}$.

The inner 1s shell of graphite is 284 eV far from the Fermi energy, hence the XAFS spectrum of graphite is expected to produce a first absorption edge at this photon energy. As resumed in the sketch in Fig. 3.2c, the XANES region of the absorption spectrum consists of electronic transitions from the 1s inner shell to the first unoccupied electronic bands, namely the π^* and σ^* bands, according to the selection rules. For higher photon energies, the spectral modulations present in the EXAFS region carry information on the graphite lattice structure.

The results of the XANES analysis are summarized in Fig. 3.3a. The orbital selectivity of XAFS technique is reflected in the angular dependence of the absorption features: for an angle of 0^{o} between the SXR beam polarization and the crystal basal plane, only transition to σ^* states inside the graphene layer are allowed, resulting in a sharp edge at 292.5 eV. On the other hand, rotating the crystal allows having a non-zero projection along the π^* orbital, resulting in another absorption edge at lower energies, corresponding to 285.5 eV, with amplitude increasing for higher angles (as clearly shown by Fig. 3.3a). The results are in excellent agreement with high-resolution XAFS measurements carried out at synchrotron light facilities [153, 154].

Figure 3.3b reports the main results of the EXAFS analysis. After background subtraction and conversion from photon energy to photoelectron wavevector values, the resulting signal is fitted with the EXAFS equation 3.4, where

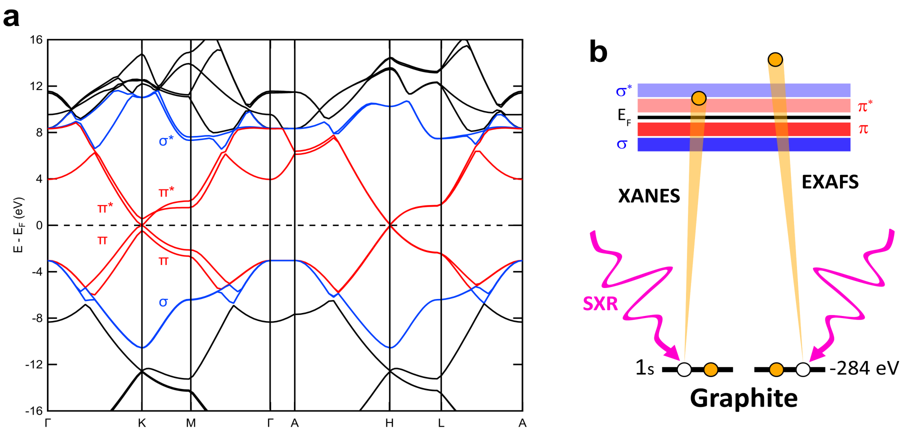

Figure 3.2: XAFS sensitivity to the electronic band structure of graphite. a) presents the band structure of graphite which we calculated with the DFT package Quantum Espresso. Highlighted in colors are the main contributions to the VB and CB: in red the π (VB) and π^* (CB) bands, originated by the carbon p_z orbitals, while in blue the σ (valence) and σ^* (conduction) bands, results of the sp^2 hybridization. A schematics of the contributions to XAFS spectrum is reported in b) [150] transitions from the 1s inner shell to electronic bound states close to the Fermi edge, constitute the XANES, while the EXAFS originates from emission of photoelectrons in the continuum. Note that there is no hard boundary separating the two regions of the XAFS spectrum.

the lattice distances and the coordination numbers are fitting parameters, while the scattering amplitudes and phases have been evaluated with ab initio calculations. Individual contributions to the EXAFS signal coming from groups of neighboring atoms can be calculated as well as their overall sum, as indicated by the figure (in this case, calculations are limited to the first four nearest neighbors due to the limited range of wave-vector values). From the Fourier analysis, considering the relative coordination numbers, the distances for the first four nearest neighbors are: (1.66 ± 0.03)Å, (2.58 ± 0.12)Å, (2.92 ± 0.03)Åand (4.01 ± 0.10)Å, where the error is the one obtained by the fit routine. The results are again in agreement with values extracted from measurements taken with synchrotron X-ray sources [155].

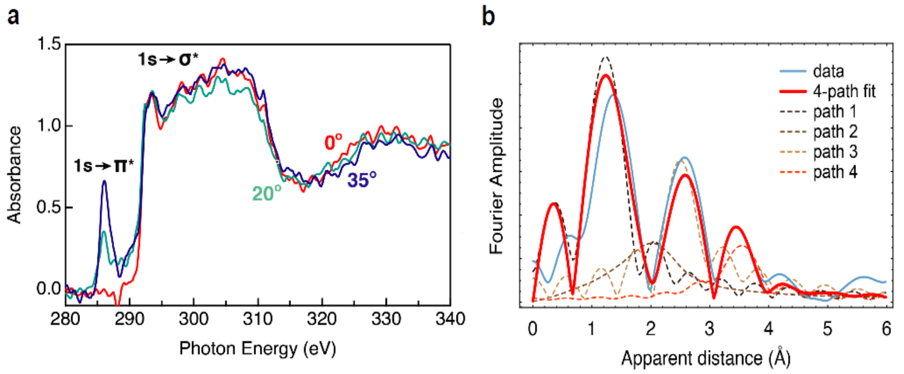

Figure 3.3: AttoXAFS spectroscopy on graphite [150]. a) The XANES region exhibits orbital-selectivity as function of the angle between the SXR beam polarization and the graphite basal plane. For any component projected onto the basal plane (graphene layer) a peak at 292.5 eV is obtained, corresponding to transition to σ^* band, while the π^* edge appears at 285.5 eV only for angles different from normal incidence. The lattice bond distances relative to the first four nearest neighbors are retrieved from the EXAFS region: b) shows the Fourier amplitude of the experimental spectrum together with the individual contributions from the first four scattering paths (dashed lines) and their sum (red line). Reprinted with permission from [150]. Copyright (2018) by the Optical Society of America.

3.3 Sample characterization

In this section, the XAFS characterization of the graphite samples used for time-resolved experiments (Chap. 4) is reported. Two different thin flakes of HOPG, namely 95 and 20 nm thickness, have been studied. The 95 nm sample has been chosen because it corresponds to the absorption length of graphite at the carbon K-edge. A thinner sample has been instead used for investigations of lattice dynamics, where the effects result to be stronger for lower thickness. The flakes are deposited directly on a metallic TEM grid (see Fig. 3.4) without the support of any substrate, which is of great help for XAFS application because of the non-negligible absorption in the substrate itself. The thickness of the thin flakes has been verified through electron energy-loss spectroscopy.

The SXR spectrum and the transmitted portion through the 95 nm thick sample is present in Fig. 3.5. Both in the 2D and the 1D spectra, a clear ab-

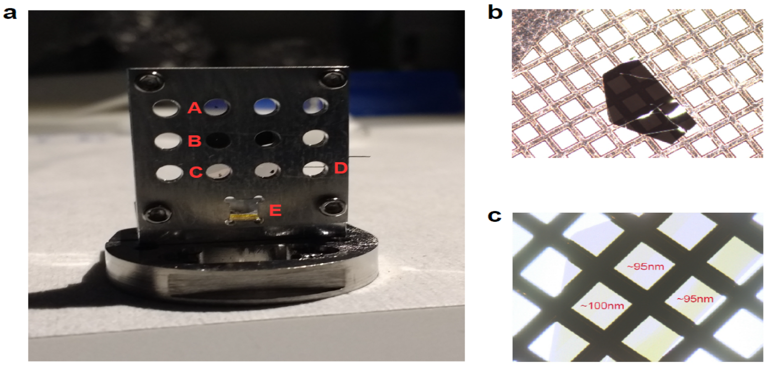

Figure 3.4: Sample holder and graphite flake used for the time-resolved XAFS measurements. a) Indicated with letters are the components used in the experimental campaign: A is the 20 nm thick graphite sample, B is the Nickel disk used for spatial overlap, C is the 95 nm thick sample, D is a metallic thin wire for imaging system calibration, E is the BBO used for spatio-temporal overlap. b) Picture of the 95 nm thick sample directly deposited on the copper TEM grid, together with its electron-energy loss spectroscopy image in c), from which the thickness is determined.

sorption edge is detected around 284 eV and non-zero absorption is detected up to ~ 450 eV. Also, visible modulations on the transmitted SXR spectrum are appearing for energies higher 284 eV, as expected in the EXAFS region according to the description in 3.1.2.

The dependence of the XAFS spectra on angle and thickness is shown in Fig. 3.6. As for the results discussed in Sec. 3.2, both features corresponding to transitions to π^* and σ^* bands are identified, with the results being in agreement with observations found in [150]. For energies after the edge, clearer modulations appear for both the reported spectra with respect to the measurements shown in 3.3a: this could be related to a higher quality of the samples here reported. In 3.6b, the clear difference in absorption amplitude between the two samples is shown, while the general shape of the absorption spectrum is conserved.

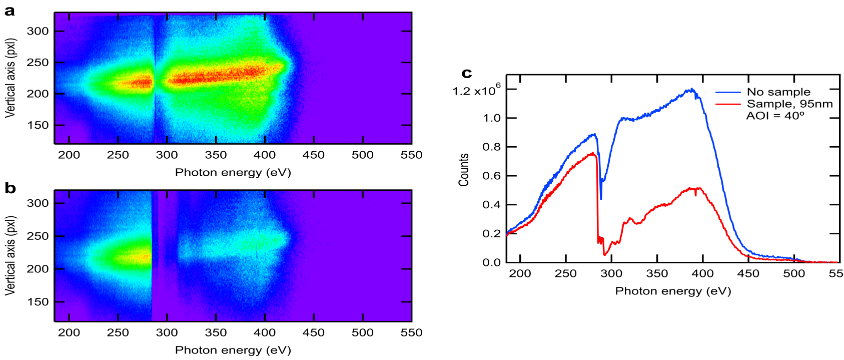

Figure 3.5: Detection of transmitted SXR spectrum through the 95 nm thick sample. To obtain the absorption of the material, measurements of the reference spectrum (a) and of the transmission through sample (b) are recorded on the SXR camera. Both spectra are obtained by averaging 20 spectra of 40 s integration time each. The vertically integrated spectra are reported in c) to highlight the energy-dependent transmission of the material. The absorbance is defined as the logarithm of the ratio between the "no sample" and "sample" spectra.

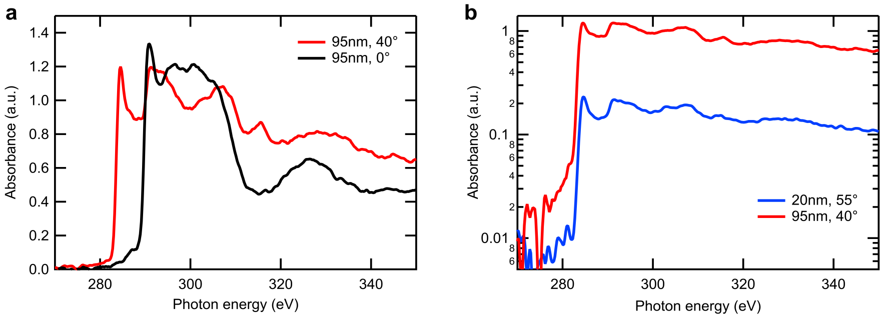

Figure 3.6: Graphite XAFS sample characterization. a) shows the angle dependence of the XAFS spectrum for the 95 nm sample. The two absorption edges corresponding to transition to π^* and σ^* bands are clearly identified, as observed in the results of [150]. The dependence on sample thickness is shown in figure (b), where the XAFS spectra for the 95 nm and the 20 nm thick samples are reported. Most of the spectral features appear identical on a broad spectral range, despite being two different samples measured at slightly different angles. Intensity scale is set to be logarithmic to highlight the small differences.

Finally, the XAFS data are compared to spectral measurements carried out at the NAno Magnetism Unit (NAMU) beamline at ALBA synchrotron facility by our collaborators. A summary of the comparison is presented in Fig. 3.7. Data collected on the 95 nm thick sample are considered for two different angles (0° and 40°) and result to be in unexpectedly good agreement with synchrotron data. Despite the lower energy resolution of our spectrometer, the most important features are identified over the reported energy range, highlighting the sensitivity of XAFS spectroscopy using attosecond SXR pulses and its potential for time-resolved spectroscopy.

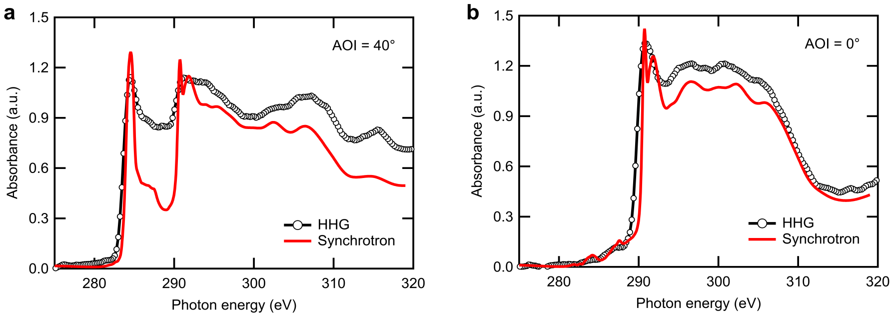

Figure 3.7: Comparison with XAFS data collected at a synchrotron SXR beamline. For the 95 nm thick sample, the XAFS spectra for 40° (a) and 0° (b) is plotted together with spectra measured at ALBA synchrotron by our collaborators from NAno Magnetism Unit (NAMU). Despite the lower spectral resolution of the HHG measurements (see Sec. 2.2.1 for details), the spectra are in excellent agreement over the reported energy range.

3.4 Modeling the XAFS spectra

The XAFS spectrum is, by definition, a quantitative measurement of the unoccupied electronic DOS of the probed material, especially when the absorption involves core levels (K-, L- edge spectroscopy) for which ambiguities coming from multiplet state can be resolved. This means that, upon experimental resolution and non-zero transition dipole elements, a direct mapping of the unoccupied DOS is possible. In this section, the model is applied to static XAFS spectra, while in Sec. 4.2.4 an attempt to model time-resolved data is reported.

The main ingredient of the numerical model is the calculation of an accurate band structure, from which the DOS can be obtained. For this, we employed the density-functional-theory (DFT) code Quantum Espresso, which result is shown in Fig. 3.2. To extract the DOS from the band structure, integration along the k-space dimension is performed directly via software, which also allows the possibility to consider the individual band contributions along with the total sum (used to identify the predominant character of each band, as reported in the figure).

Once the DOS is calculated, it is possible to get a quantitative comparison between the measured absorption spectrum and the number of unoccupied states, which are described by

$$N_{un}(E) = [1 - FD(E, T_e, \mu_e)] \cdot DOS(E), \tag{3.5}$$

where FD stands for a Fermi-Dirac distribution, used to model the electronic system in thermodynamic equilibrium given its temperature T_e and chemical potential μ_e. To connect this quantity to the measured spectra, the last thing to consider is the finite resolution of our measurement, which can be modeled by a Voigt function (distribution given by the convolution of a Lorentzian and a Gaussian distribution). In this way, the transition lifetime can be described by the Lorentzian component while the spectral resolution modeled as a Gaussian broadening. So, a final convolution between the Voigt profile and the N_{un} gives the proper function to numerically fit the absorption spectrum.

Using the fit to the static absorption spectrum, it is possible to fix most of the free parameters involved: we find $\Delta L = 150\,\text{meV}$ for the $1s$ core-hole lifetime (fixed according to [156, 157]), $\Delta G = 250\,\text{meV}$ for experimental resolution, $T_e = 350\,\text{K}$, $\mu_e = 284.75\,\text{eV}$ (meant as center of FD distribution). The agreement is extremely good for most of the region around the π^* edge, while it slightly deviates around the σ^* and in the region between the two edges, as shown in Fig. 3.8. The discrepancy between the two edges comes from imposing a theoretical DOS (based on DFT) and experimental XAFS with certain spectral resolution. Also, the XAFS spectrum is highly dependent on the incident angle (as observed in 3.2 and 3.3, so the contributions of different bands have to be taken into account with their specific weights. The estimation of these contributions with their correct weights and general refinement of the DFT calculations for the DOS are key ingredients to obtain a better agreement with experimental spectra.

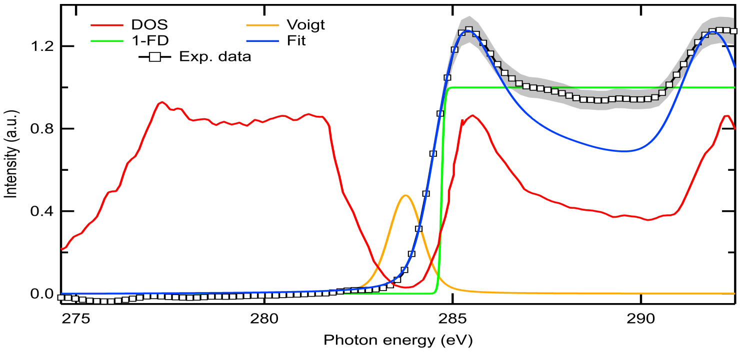

Figure 3.8: Measured XAFS spectrum of 95 nm thick graphite at 40° respect to the SXR beam polarization together with analytic model based on the DOS and FD distribution. For completeness, all the ingredients of the model have been reported. The shaded area represents the statistical error on the acquisition.

Another attempt to model the XAFS spectra has been done using numerical simulations using the self-consistent real-space FDMNES package [158], shown in Fig. 3.9. The package is based on ab-initio approach and it aims to simulate general x-ray absorption or scattering data. It is based on DFT (single electronic effects) but it includes some time-dependent corrections (TD-DFT) to try to simulate the excited states produced by light-matter interaction. Here, we obtain excellent agreement between simulations of non-excited atoms and experiment. The output of the calculations is an absorption spectrum at extremely high spectral resolution corresponding to a measurement of the transition probabilities at any given photon energy. For comparison with experimental data, the spectrum is then convoluted with a gaussian of 1.2 eV and energy-dependent arctangent-like function of 15 eV total height [158].

3.5 Conclusions

X-ray absorption spectroscopy is a powerful and well-established technique to investigate the matter in different states, from gases to crystals, accessing infor-

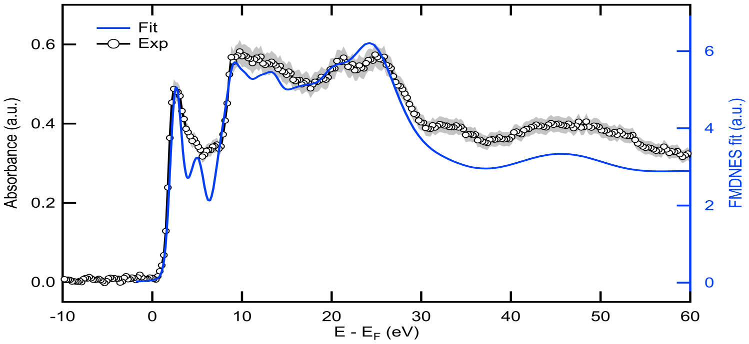

Figure 3.9: Measured XAFS spectrum of 95 nm thick graphite at 40° respect to the SXR beam polarization together with numerical model based on FDMNES package, showing a good agreement between the two curves over a broad energy range (70 eV). The shaded area represents the statistical error on the acquisition.

mation on the electronic and lattice structure of the target. The photon energy range allows interrogating electronic levels of the inner shells which are characteristic of the elements constituting the experimental target, making XAFS an element-specific technique.

The XAFS spectrum is usually considered composed of two different regions, related to different electronic transitions and hence carrying different information. The region in the proximity of the absorption edge is called XANES and corresponds to transitions from the inner shell to the unoccupied bound states close to the Fermi level satisfying the selection rules. The analysis of the XANES region gives access to the electronic structure with orbital selectivity. For photon energies higher than the absorption edge, electrons are directly emitted into the continuum as electron waves that scatter against the electron density situated at each surrounding atom. The spectral interference produced by this scattering can be analyzed to extract information on the position of the nearest neighbors with the EXAFS analysis.

While XAFS is a well-established technique for applications at large-scale facilities like synchrotron or FEL X-ray sources for several decades, the advent of HHG-based sources during the last years brought two main advantages.

First, the possibility to have table-top X-ray sources brought XAFS into optics laboratories, where the technique has been demonstrated for the first time in our group with satisfactory results [25], despite the definitively lower photon flux compared to large-scale facilities. Second, and probably most interesting, the possibility to confine X-ray radiation to pulses of sub-fs duration, while it is in general limited to the fs/ps regime for large-scale facilities (tens of fs for FELs, hundreds of fs up to several ps for synchrotron sources). X-ray pulses with sub-fs duration constitute the best probe for ultrafast electron dynamics, taking place on the few-fs timescale, hence too fast to be probed at large-scale facilities.

The first demonstration of the capabilities of using attosecond SXR pulses produced by our setup for XAFS spectroscopy to study the electronic and lattice structure has been reported in [150] with a study on graphite. The simultaneous probing of the π^* and σ^* orbitals together with the retrieval of the distances of the four nearest neighbors has been obtained, resulting in excellent agreement with synchrotron data found in the literature. XAFS spectra of graphite samples used for the experiments reported in this thesis have been compared with data taken at ALBA synchrotron light source, demonstrating an extremely good agreement despite the lower spectral resolution of the HHG setup.

Finally, preliminary results of two different strategies for modeling experimental XAFS spectra are presented. The first approach relies on the quantitative information present in XAFS data on the unoccupied electronic states of the material and implies the use of the DOS, obtained with DFT calculation, combined with a FD distribution at a given temperature. The second is instead a completely numerical approach, still based on DFT, to simulate the expected XAFS data over a broad spectral range. Refinement of these approaches will extend their application to the more complex time-resolved case.

Chapter 4

Ultrafast carrier and lattice dynamics in graphite

This chapter contains a description of the experimental investigation carried out on graphite to study ultrafast carrier and lattice dynamics via attosecond transient XAFS spectroscopy, constituting the core of my Ph.D. research project.

First, the measured time-resolved data are presented in Sec. 4.1. The experimental conditions to perform transient XAFS spectroscopy, the data acquisition protocol and the estimation of the pump pulse parameters are reported. Finally, the measured data are presented in two different groups, each related to a different graphite sample thickness, as introduced in Sec. 3.3.

The final section (4.2) contains a comprehensive report of the data analysis developed for the interpretation of the experimental data. The retrieved dynamics are presented from fastest to slowest, describing in detail the tools used to extract information. The carrier response to the electric field carried by the pump pulse is described in 4.2.1, while the mechanisms dominating carrier-carrier scattering in the first tens of femtoseconds are studied in 4.2.2. The evolution of the excited carrier distribution is analyzed in 4.2.3 and modeled with Fermi-Dirac (FD) statistics in 4.2.4. The coupling of the electronic excitation to SCOPs and in general to the lattice is modeled with a three-temperature model (3TM) (4.2.5). The effects induced by phonon excitation on the band structure are reported in 4.2.7, while a Fourier analysis is used to identify the different excited vibrational modes (4.2.8).

4.1 Attosecond transient XAFS in graphite

In this section, the experimental campaign of time-resolved measurements carried out on graphite is presented. A detailed description of the data acquisition protocol used is reported in Sec. 4.1.1, while the estimation of the pump pulse parameters is described in Sec. 4.1.2 for all the different conditions implemented. Finally, an overview of the time-resolved XAFS measurements is presented for both graphite samples of 95 nm and 20 nm thickness.

Measurements have been carried out on both samples with different configurations of the pump pulse, varying the pump fluence (from ~ 1 up to $\sim 200\,\mathrm{mJ/cm^2}$) and the pump wavelength ($1.85\,\mu\mathrm{m}$ and $0.8\,\mu\mathrm{m}$), where the dependence of the observed signal on these parameters resulted to be decisive for the interpretation of results. As described already in 3.3, the thicker sample, chosen with a thickness similar to one absorption length, has been studied for general carrier and lattice dynamics. The thinner one has been instead investigated mainly looking for evidence of lattice dynamics, an effect proven to be stronger for decreasing thickness (1.2.2). The overview contains the most significant datasets which have been evaluated for the data analysis and for the interpretation of the experimental results. The remaining datasets are reported in the Appendix for completeness.

The SXR probe pulse is p-polarized as the IR driver used for the HHG process. The pump pulse polarization is instead rotated by 90° with respect to the probe (s-polarization for the pump, p-polarization for the probe): the reason for this choice is to maximize the pump light absorption for the excitation of charge carriers from π to π^* band, only obtained for in-plane polarization. The graphite sample is rotated with respect to the SXR beam polarization in order to achieve sensitivity to both π^* and σ^* bands (as reported in Sec. 3.3).

4.1.1 Data acquisition protocol

In order to detect small variations of the SXR absorption spectrum induced by the IR pump pulse, the data acquisition protocol consists of a collection of series of transmission spectra with different combinations of the pump and probe beams overlapped on the sample. The alternation is made possible using shutters along with the probe and the pump way, synchronized with the acquisition camera.

The transient signal will be constituted by the differences between the spectrum taken with both pump and probe and the spectrum taken with only the probe after a proper background subtraction is performed. In this scenario, recording the probe only spectrum is of high importance to be able to rule out any possible influence of SXR spectral fluctuations on the analysis, while the pump only spectrum is important for correct background subtraction. For every experiment performed, the acquisition scheme is composed of:

- 15 spectra of 40 seconds each for pump+probe and only probe cases
- 4 spectra of 40 seconds for only pump case, taken every 4 spectra of the other combinations

These numbers translate in a total integration time of about 25 minutes per each time delay thus to record the entire full trace like the ones shown in Sec. 4.1.3 and 4.1.4 a total experiment time of about 33 hours is required.

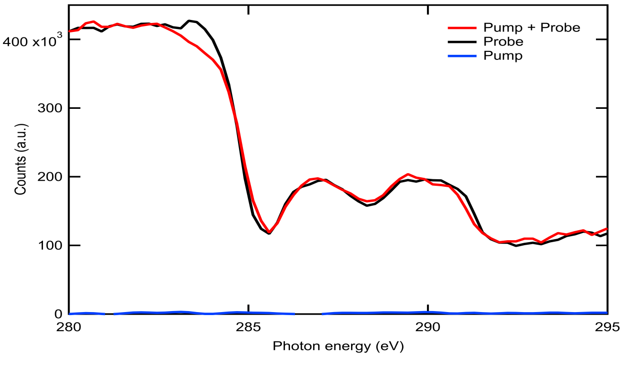

Figure 4.1: Measured transmission spectra of graphite with the three combinations of pump and probe pulses. All the spectra are obtained with the sum of 15 acquisitions, each corresponding to an integration time of 40 s, and removal of dark noise background.

The raw, recorded 2D transmitted spectra are integrated over the region of interest in the vertical dimension of the CCD and the recorded frames for pump+probe (T_{pp}), probe only (T_0), pump only (T_p) are summed to obtain individual 1D spectra at each time delay. Then the detector dark and thermal noise is removed from each spectrum.

Next, to remove the residual pump background the summed 1D pump only spectrum is multiplied by 15/4, accounting for the reduced integration time, and then subtracted from the pump+probe spectrum. Typically, the pump only spectrum shows larger noise coming from the lower pump only integration time and therefore a 3-point boxcar smoothing is applied to the pump only spectrum. In order to account for slow changes in the SXR flux the pump+probe, and probe only spectra are normalized to signal before carbon K-edge and 3-point boxcar smoothing is applied.

We finally calculate the differential transmission normalized to the unpumped case

$$\Delta T = (T_{pp} - T_0)/T_0 \tag{4.1}$$

from which we can obtain the differential absorption from the simple relation

$$-\log(\Delta T + 1) = \Delta A, \tag{4.2}$$

using the definition of absorbance, $A = log(\frac{I_0}{I_t})$, with I_0 is the intensity incident on the sample and I_t the transmitted one.

4.1.2 Pump pulse parameters

For the calculation of the pump pulse parameters, the beam profile has been measured with a knife-edge scan while the temporal duration quantified with a second-harmonic frequency-resolved optical grating measurement (SH-FROG). The retrieved temporal profile has been already shown in Fig. 2.11 and 2.13 respectively for the two cases of $1.85\,\mu$m and $0.8\,\mu$m. Calibration of the pump pulse energy is obtained with the use of different beam splitters at the beginning of the beamline (5% reflection for the low and medium fluence, 30% for the high fluence) and attenuation stages, made of thin pellicles used in transmission, for fine-tuning.

To calculate any quantity inside the material, the Fresnel losses occurring at the front surface of the graphite film are considered for a crystal axis rotation of 39° for the 95 nm sample and a rotation of 55° for the 20 nm sample. A carrier-independent refractive index is considered for the calculations: $n_{1.8\mu m} = 3.8497 - 3.092i$ and $n_{0.8\mu m} = 3.0867 - 1.8855i$ [159]. This produces a reduction of the pump pulse energy of about 60% for the 1.85 μm case and about 46% for the 0.8 μm one. Also, no effect related to absorption is included, meaning that the value indicated corresponds to the one right after the front surface.

In the appendix of the thesis three tables are provided (A.1), each one resuming the important pulse parameters for the different sets of measurements reported in Sec. 4.1.3 and 4.1.4, namely the 1.85 μm and 0.8 μm case for the 95 nm sample and the 1.85 μm again but for the 20 nm one.

4.1.3 95 nm thick sample

The results of the time-resolved XAFS experiments on the 95 nm thick sample are reported in this section. For all the measurements, the sample is rotated in order to have an angle of 40° between the SXR beam polarization (p-polarized) and the crystal axis. At this angle, according to the results shown in Sec. 3.3, the SXR pulse can probe both the π^* and σ^* bands of graphite. The pump beam is s-polarized to maximize the pump light absorption for the excitation of charge carriers from π to π^* band, only obtained for in-plane polarization. The results are grouped according to the pump pulse configuration used, showing for each configuration two different datasets: one measurement at high temporal resolution, scanning over few tens of femtoseconds around the zero time delay; the second measurement is recorded over a longer time delay range (usually ~ 1 ps) but with lower temporal resolution.

For each dataset, two different plots are reported:

- a 2D color plot showing the differential absorption spectrum ΔA (as defined in Eq. 4.1, 4.2) as function of time delay;
- a 1D plot showing the ΔA lineouts over a certain energy range as function of time delay, defined as the sum over the energy pixels contained in the transient signal, $\sum_i \Delta A(E_i)$.

The lineouts are useful to track the temporal evolution of transient signals related to different physical quantities, as it will be clearly shown in this section.

Before starting the overview of all the measurements performed, a general discussion on the shape of the differential absorption spectrum is presented here, which applies to all the measurements shown in this chapter. An example of ΔA spectrum is shown in Fig. 4.2 (the case of high-fluence pump pulse has been chosen because it presents the strongest transient signals), together with the static XAFS spectrum. Two distinct transient features are visible in the differential absorption spectrum, positioned at the π^* and σ^* edges, producing changes in absorption up to 15%.

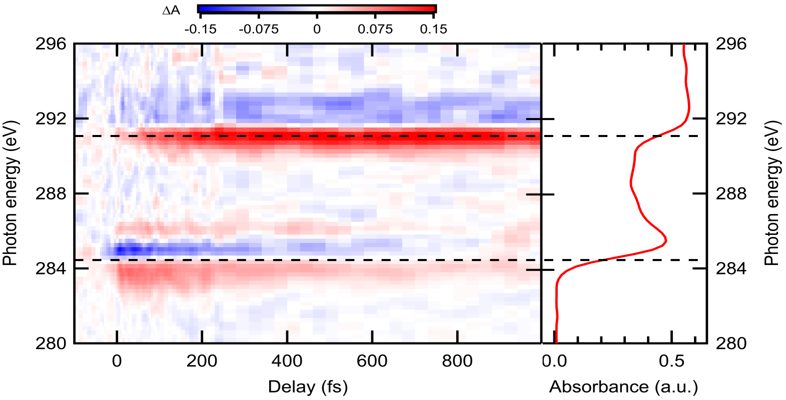

Figure 4.2: Differential absorption measurement in 95,nm graphite for $1.85\,\mu$m, $208\,$mJ/cm^2 pump pulse over $1\,$ps time delay range. The right panel of the figure presents the static absorption spectrum of graphite, reported here to highlight where the transient signals occur. The positive and negative signal around $285\,$eV (slope of the π^* edge) is related to creation of holes in VB and electrons in CB due to pump photoexcitation. The signal at $291.5\,$eV occurs at the σ^* edge and is not related to carrier excitation, but rather to band structure modifications induced by the excitation of strongly-coupled phonons (SCOPs).

The transient signal observed at the π^* edge presents a positive and negative feature, respectively below and above $284.7\,$eV. Both signals grow fast in time (they peak around $10-15\,\mathrm{fs}$) and decay after few hundreds of fs (see Fig. 4.5). The pump photon energy ($0.67\,\mathrm{eV}$) is enough to promote electrons from VB to CB near the K-point of the band structure, given the almost-zero band-gap of graphite ($\sim 40\,\mathrm{meV}$, as indicated by DFT calculations). The energy position, the temporal evolution and the sign of the signals allow us to assign these features to the creation of electrons in the CB and holes in the VB. An increase in electron population in CB would block transitions from the carbon 1s inner shell to CB states, producing a decrease in SXR absorption (i.e. negative feature). The opposite can be stated for the VB: the creation of holes as the result of photoexcitation would allow transitions to these unoccupied states, previously denied due to Pauli-blocking. The temporal evolution of these features is related to carrier population dynamics, as will be shown in 4.2. The additional negative signal appearing at higher photon energies has a similar temporal evolution of the electron and hole signals, it is responsible for the asymmetry between the two and is observed only for pump fluences above $8\,\mathrm{mJ/cm^2}$. We interpret this signal as band structure modification due to the high concentration of excited carriers (an effect similar to band-gap renormalization effects in semiconductors).

On the other hand, the pump photon energy is not sufficient to excite carriers at the Γ point, where the direct band-gap is $6\,\mathrm{eV}$, for which reason we don't expect a carrier-related feature at the σ^* edge. Here the observed signal is slower respect to the feature at the π^* edge: it peaks around $250\,\mathrm{fs}$ and doesn't show a clear decay over the observed time delay range (see Fig. 4.5). The feature presents a mainly positive signal which can be explained in terms of an edge shift and broadening (see Sec. 4.2.7). We attribute this modification of the absorption spectrum to the phonon-induced changes of the DOS of graphite. This interpretation was already proposed in the work of Van der Veen et al. [123] as the result of the interaction between the electronic system and SCOPs.

$1.85\,\mu$m, low fluence pump pulse

The differential absorption spectrum obtained in the experiment with $1.85\,\mu\mathrm{m}$, $8\,\mathrm{mJ/cm^2}$ pump pulse is shown in Fig. 4.3 over $1\,\mathrm{ps}$ time delay range. Clearly visible are the positive and negative signals at the π^* edge, almost symmetric in energy, and a weak positive signal at the σ^* edge. The right panel presents the lineouts calculated for the three mentioned features: electrons and holes signals present a rise time longer than the pump pulse duration (peak around

$50-60$ fs) and decay over few hundreds of fs. The σ^* signal instead appears only at ~ 400 fs and doesn't present a clear decay over the observed time delay range.

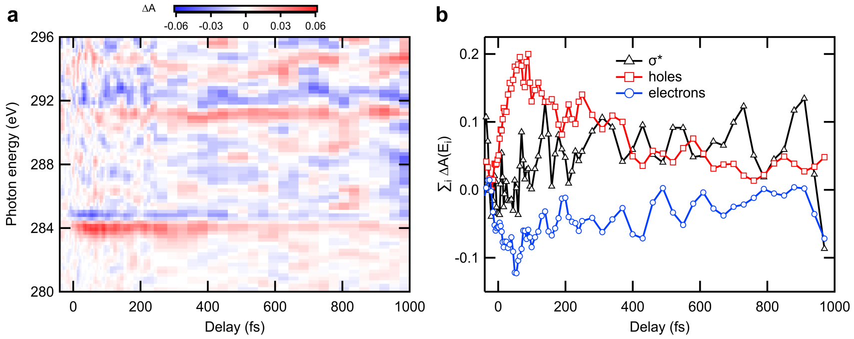

Figure 4.3: Differential absorption measurement in 95 nm graphite for 1.85 μm, 8 mJ/cm^2 pump pulse over 1 ps time delay range. In a) the ΔA spectrum as function of time delay is reported. Time delay step size is: 5 fs in $-40 : 100$ fs range, 10 fs in $100 : 250$ fs range, 30 fs in $250 : 1000$ fs range. b) Temporal behavior of the signal assigned to holes, electrons and σ^* is obtained by summing ΔA over the corresponding group of energy pixels, as defined in 4.1.3.

Using the same pump pulse conditions, a high-temporal-resolution experiment is reported in Fig. 4.4. The rise of the electron and hole signal is nicely resolved and again results to be longer than the pump pulse duration, suggesting an additional underlying mechanism different from photoexcitation (see Sec. 4.2.2). No signal is detected at the σ^* edge for the time delay range scanned. By looking at the lineouts, the rise of the ΔA signal for both electrons and holes presents modulations with a period of ~ 6 fs. A Fourier analysis of these oscillations is presented in Sec. 4.2.1.

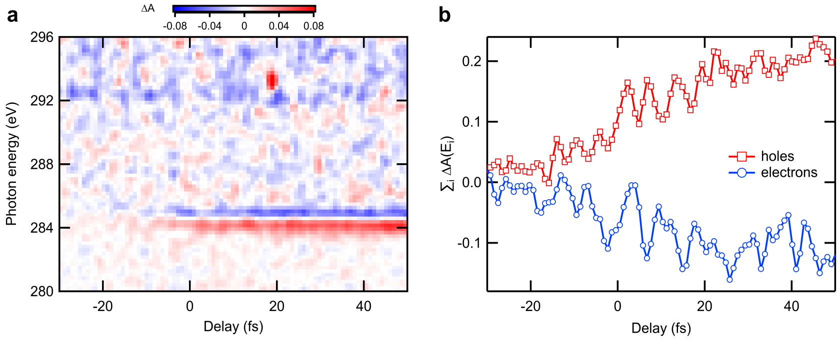

Figure 4.4: Sub-fs-resolved differential absorption measurement in 95 nm graphite for 1.85 μm, 8 mJ/cm^2 pump pulse. Time delay step size is 0.9 fs for the whole time delay range.

1.85 μm, high fluence pump pulse

The ΔA spectrum obtained with 1.85 μm, 208 mJ/cm^2 pump pulse over 1 ps time range is reported in Fig. 4.5 and has been partially described in Sec. 4.1.3. Here, in addition, the lineouts relative to the three main features of the spectrum (electron and hole signals at the π^* edge and the positive signal at the σ^* edge) are presented. The rise time of the carrier signals is faster compared to the low-fluence case (peaks around $10 - 15$ fs for both electrons and holes) and comparable to the pump pulse duration, while the general time evolution is conserved. The signal at the σ^* edge is definitely stronger than the one at low pump fluence: it peaks around 250 fs and presents a faint decay with a constant definitely longer than the 1 ps range here reported.

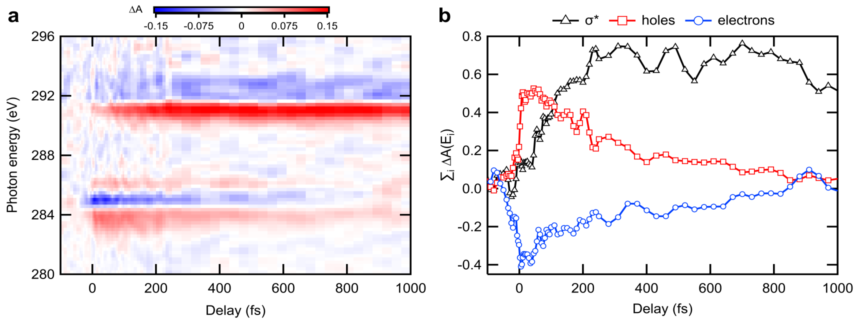

Figure 4.5: Differential absorption measurement in 95 nm graphite for 1.85 μm, 208 mJ/cm^2 pump pulse over 1 ps time delay range. Time delay step size is: 10 fs in $-100 : -40$ fs range, 5 fs in $-40 : 100$ fs range, 10 fs in $100 : 250$ fs range, 30 fs in $250 : 1000$ fs range.

The sub-fs-resolution scan with 1.85 μm, 208 mJ/cm^2 pump pulse is reported in Fig. 4.6. The rise time is on the order of the pump pulse duration (12.5 fs) and no clear oscillations on the rise of the hole and electron signals are detected, in contrast with the observations for the 1.85 μm, low fluence case. Interestingly, the signal at the σ^* edge (assigned to the coupling of carrier excitation to optical phonons) is already visible at 20 fs, a sign of extremely fast coupling dynamics occurring between the carrier and lattice system.

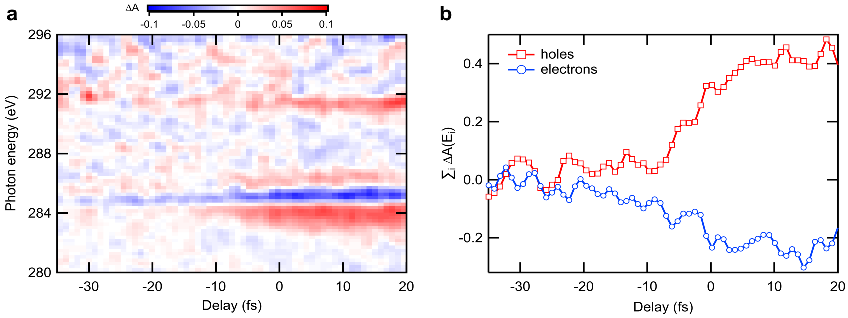

Figure 4.6: Sub-fs-resolved differential absorption measurement in 95 nm graphite for 1.85 μm, 208 mJ/cm^2 pump pulse. Time delay step size is 0.9 fs for the whole time delay range.

0.8 μm, medium fluence pump pulse

For the experiments performed with 0.8 μm, 5.3 mJ/cm^2 pump pulse, here two different measurements are reported: a fs-resolved scan up to 80 fs time delay and a sub-fs-resolved scan around the zero time delay. A long-delay-range scan is reported in the appendix A (because it has not been considered for the data analysis reported in this thesis). Figure 4.7 shows the results of the fs-resolved scan: despite the finite resolution of the SXR spectrometer, the separation between holes and electrons signals is slightly clearer than the 1.85 μm, 8 mJ/cm^2 case due to the higher pump photon energy. Also for this case, the lineouts are presenting a rise longer than the pump pulse duration both for electrons and holes, suggesting a similarity with respect to the 1.85 μm, 8 mJ/cm^2 case. For the time delay range reported, no clear signal is discernible at the σ^* edge.

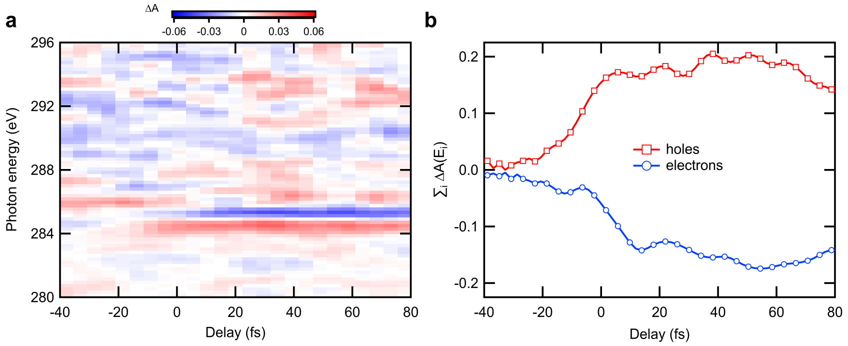

Figure 4.7: Differential absorption measurement in 95 nm graphite for 0.8 μm, 5.3 mJ/cm^2 pump pulse. Time delay step size is 4 fs for the whole time delay range.

Finally, the results of the sub-fs-resolved scan are reported in Fig. 4.8. The scan is a zoom on the rise of the signal with 0.6 fs step size and it reveals, as for the case of 1.85 μm, 8 mJ/cm^2 pump, an intensity modulation on top of the rise signal, this time with a higher frequency (period is around 3 fs). Also for this scan, a proper analysis of the oscillatory behavior is reported in Sec. 4.2.1.

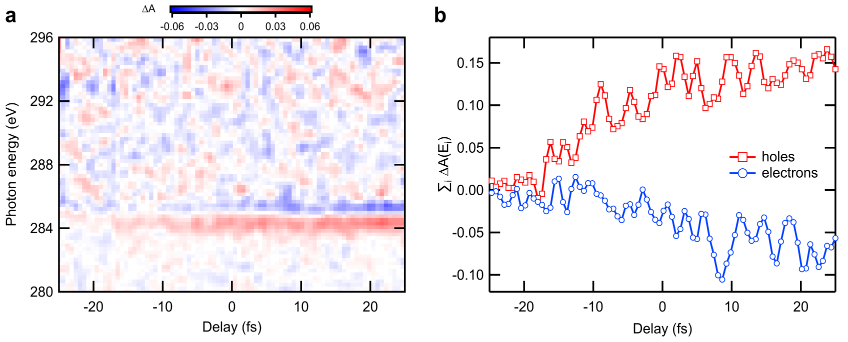

Figure 4.8: Sub-fs-resolved differential absorption measurement in 95 nm graphite for 0.8 μm, 5.3 mJ/cm^2 pump pulse. Time delay step size is 0.6 fs for the whole time delay range.

4.1.4 20 nm thick sample

Compared to the case of the thicker sample, measurements on this sample have been carried out on both the fs and the ps timescale, with the aim of looking for evidence of lattice dynamics following the electronic excitation and the EPC. Measurements on this sample have been performed only for 1.85 μm pump pulse at high and medium fluence (respectively 150 and 42 mJ/cm^2). Pump parameters are lower than the ones for thicker sample due to the fact that here the angle between SXR polarization and crystal axis is higher, namely 55°.

First, pump-probe measurements similar to the ones performed on the thicker sample were recorded, with the goal of proving that the material response after photoexcitation stays unchanged. The following experiments were carried out:

- sub-fs scan at high pump fluence, reported in A;
- fs-resolved scan at high (here reported) and medium pump fluence (presented in A).
- ps-resolved experiment at high pump fluence has been performed (presented in A) aiming at detecting lattice dynamics.

Femtosecond resolved scan

The results of the fs-resolved measurement on the 20,nm graphite sample are reported in Fig. 4.9. The observed features are in line with measurements carried out on the thicker sample at similar pump pulse conditions (4.5). The only visible difference is the amplitude of the signals: by looking at the lineouts, while the holes and electrons signal have similar amplitude, the signal detected at σ^* edge is definitely lower than the one observed on the thicker sample (4.5). A possible explanation is the lower pump fluence (due to the higher angle between SXR beam polarization and crystal axis): while the carrier signal stays constant, probably close to saturation effects, the excitation of SCOPs is reduced.

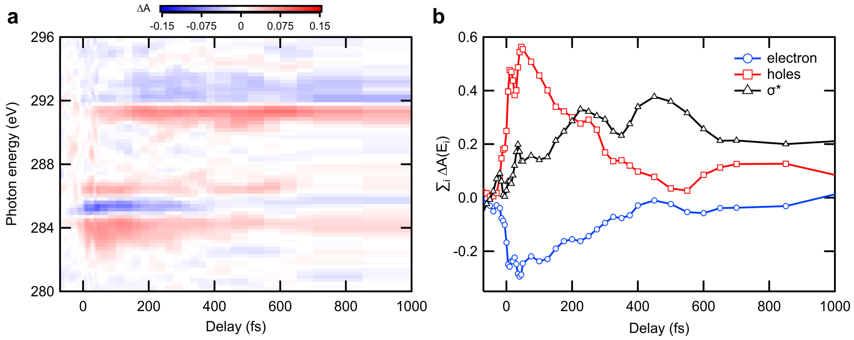

Figure 4.9: Fs-resolved differential absorption measurement in 20,nm graphite for $1.85\,\mu$m, $150\,$mJ/cm^2 pump pulse. Time delay step size is: $5\,$fs in $-70 : 50\,$fs range, $25\,$fs in $50 : 400\,$fs range, $50\,$fs in $400 : 700\,$fs range, $150\,$fs in $700 : 1000\,$fs range.

4.2 Data analysis and interpretation

After the overview of all the time-resolved data collected on graphite shown in the previous sections, the data analysis and the interpretation of the results is presented here. The approach is to start with the fastest observed dynamics, on the order of the pump pulse's optical cycle, and then move towards the slower ones, up to picosecond regime. In each of the following section, the general idea behind the analysis will be explained, together with the presentation of the method and the indication of which datasets have been considered.

4.2.1 Sub-optical-cycle dynamics

In general pump-probe experiments, the duration of the laser pulses used sets a limit to the temporal resolution. In our case, having a probe with sub-fs duration, the main limitation resides in the pump pulse, which in our case ranges between 12 and 15 fs. A consequence of this is the fact that the observed transient signal has a rise time which is usually the convolution of the pump pulse profile and the characteristic time of the photo-induced dynamics. Important insights on carrier dynamics taking place in the first tens of femtoseconds have been extracted by examining the dependence of the rise time of the signal on pump pulse parameters like fluence and wavelength (shown in next Sec. 4.2.2), but nothing really faster than $15 - 20$ fs could be deduced from such analysis.

An important quantity to consider in light-matter interaction when pump intensity is relatively high (for values above 10^{11} W/cm^2) is the electric field carried by the laser pulse, entering in the non-linear regime. For these laser intensities and for CEP-stable laser pulses (meaning with a reproducible electric field over time), the interaction of the electric field with nearly-free charge carriers is not negligible and can induce measurable modulations of the absorption/reflection spectrum, as reported in Sec. 1.1.2. If this type of interaction occurs, the time scale of the induced dynamics is not only the pulse duration but its optical cycle, resulting in the possibility to detect sub-optical-cycle carrier dynamics. Experiments involving pump pulses with similar conditions have shown evidence of non-linear interaction of pump light with carriers, modulating the spectrum at twice ([83, 73, 72, 76, 75]) or three times ([74]) the pump laser frequency. The reason resides in the mechanism behind this modulation, related to nonlinear interaction with the electric field (or the vector potential) carried by the pump light (intraband currents for [83, 75], multi-photon absorption for [74], tunneling ionization for [73], Wannier-Stark localization for [72] or dynamical Franz-Keldysh effect for [76]). The electronic band structure of the material (i.e. insulating, semi-conductor, semi-metal behavior) and the pump pulse intensity determine which of these non-linear interactions dominate. These conditions are in general familiar to all the experiments involving a pump pulse which is a replica of the HHG driver, for which high pulse intensity and CEP stability are necessary requisites to obtain good HHG flux and spectral stability.

To look for possible field-driven effect in our experiments, we considered the datasets with sub-fs step size, for the cases of high- and low-fluence 1.85 μm pump and the medium-fluence 0.8 μm case, whose lineouts for electrons and holes are shown in Fig. 4.6, 4.4 and 4.8 respectively and represented here below for explanation (Fig. 4.10). Oscillations are visible on the rise of both electron and hole signal for the cases of low- and medium-fluence pump, while they are not detected for the high-fluence case. Besides, the comparison of the two cases at different pump wavelengths shows that the frequency of the oscillation changes, suggesting a dependence on this parameter.

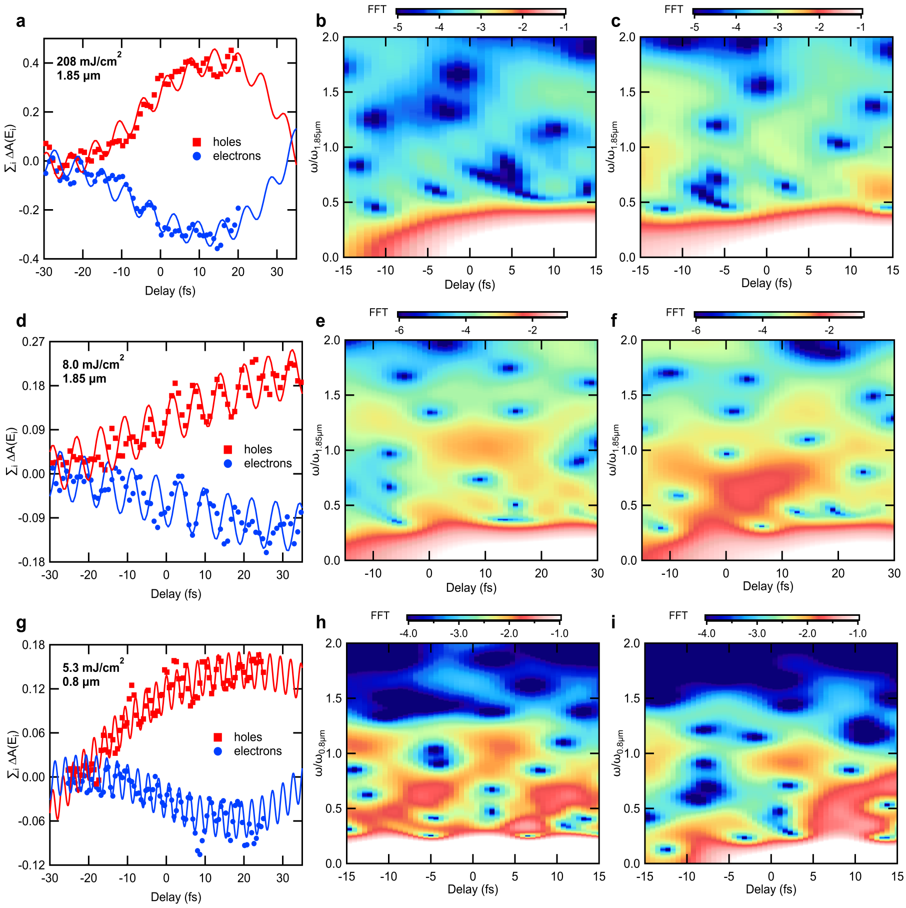

Figure 4.10: Sub-optical-cycle carrier dynamics. Lineouts extracted from measured differential absorption data, both for electrons and holes, are presented in a), d) and g), together with sine waves oscillating at the laser frequency to guide the eye over the sub-cycle modulations. The FFT amplitude obtained with STFT are presented on the two other columns, where b), e) and h) show information about the holes and c), f) and i) about the electrons.

For a proper frequency analysis, we performed a short-time Fourier transform (STFT) of these lineouts, whose results are shown in Fig. 4.10. While for all scans no clear frequency component can be observed throughout the whole scan range, for short periods around the zero time delay some spectral content is revealed at frequencies close to the driving laser frequency. In the figures, sine waves have been plotted on top of the lineouts to help the eye visualizing the modulation. This is not reflected in the high-fluence data, where no clear frequency component appears.

Our findings are supported by numerical simulations based on real-time time-dependent density-functional theory (TD-DFT) performed by our collaborators from Prof. Dr. K. Yabana's group at the University of Tsukuba [160]. They calculated the effect of the IR field on the charge density or the effective potential for our experimental conditions. The results show that these quantities are modulated at the laser frequency for the first $\sim 10-15$ fs, after which higher frequencies appear, smearing out the initial modulation effect (see Fig. 4.11). The time window in which the modulation appears is faster with increasing pump fluence, which explains the absence of such effect for the high-fluence case.

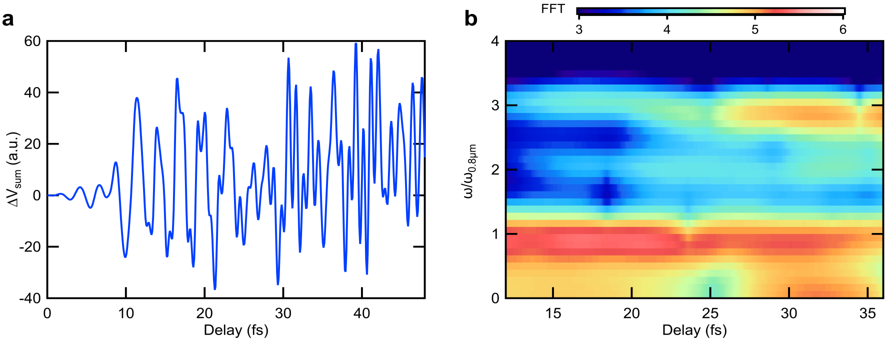

Figure 4.11: Numerical investigations on induced carrier dynamics with TD-DFT. a) The effect of the IR pump on the graphite sample is to modify locally the charge density, hence the crystalline potential felt by the electrons. This modulations shows for the first $10-15$ fs oscillations at lower frequency, while clearly higher frequencies appear later smearing out the effect. From the FFT analysis shown in b), it is clear that at the beginning the frequency corresponds to the ω_{pump}, while higher components at $2\omega_{pump}$ and $3\omega_{pump}$ appear at later times.

The main reason behind this behavior resides in the extremely high carrier mobility for graphite: after photoexcitation, the nearly-free excited carriers show an almost metallic response to the electric field, resulting in a modulation at the same laser frequency, confirmed by the behavior observed at the two different pump wavelengths. We do not observe any spectral content at twice the laser frequency, as observed in other similar experiments [83, 73, 75, 72, 76]. A limiting condition fo the observation of these features is the fact that pump and probe have crossed polarization (chosen to maximize the $\pi - \pi^*$ electronic excitation): if the non-linear modulation induced by the pump pulse is not probed in the same direction, the visibility of the effect decreases dramatically (as experimentally proved for atomic targets [161, 162]). The temporal smearing effect induced by the non-collinear angle can also play a role in this case, washing out the eventual faster modulations at higher frequency components. In any case, repeating the same experiment with parallel polarization could give another important piece of information regarding the interaction of the excited carriers with the pump electric field.

4.2.2 Carrier multiplication

The concept of carrier multiplication has been introduced already in Sec. 1.2.1 while discussing some recent experiments carried out in graphene [110, 111] and theoretical investigations [106, 107, 108, 109]. Carrier multiplication takes place when, through carrier-carrier scattering processes, the final number of excited carriers exceeds the number of carriers produced via photoexcitation. This phenomenon has attracted high interest in the field of energy harvesting and fabrication of optoelectronic devices for the possibility of generating strong currents with low-intensity laser pulses [96].

The idea behind this analysis is trying to identify which are the mechanisms dominating the ultrafast carrier-carrier scattering on the first tens of femtoseconds after photoexcitation and verify the possibility to detect carrier multiplication in graphite, at date never experimentally proved. Theoretical investigations [106, 107, 108, 109] propose Auger processes, in the form of Auger Heating (AH) and its counterpart Impact Ionization (II), as main mechanisms for carrier cooling and, under certain optical pumping conditions, carrier multiplication in graphene and graphite. Both II and AH, by definition, affect directly the number of carriers and their average kinetic energy, as resumed in the sketch in Fig. 4.12.

To extract from the differential absorption trace any insight on the primary carrier scattering phenomena occurring after photoexcitation, an analysis is performed on the generated carrier distribution (both for holes-VB and electrons-CB) inspired by the work of Gierz et al. [111]. Their experiment consists of time-resolved ARPES investigation on graphene, pumped with a $< 10\,\mathrm{fs}$, $800\,\mathrm{nm}$ pulse at a fluence of $20\,\mathrm{mJ/cm^2}$: the similar pump fluence used and the analogy in optical properties between graphene and graphite justify the use of the same approach.

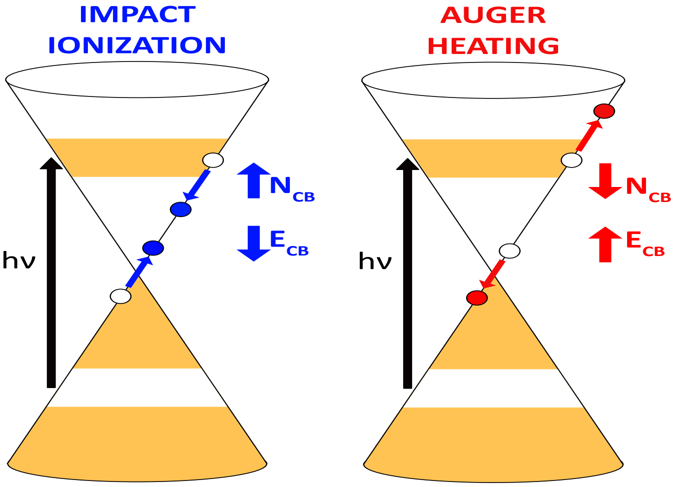

Figure 4.12: Schematic illustration of the two opposite processes dominating carrier-carrier scattering in graphite. For Impact Ionization (II), the energy lost by an electron in a scattering process is used to generate a new electron-hole pair at energies closer to the Dirac point. In Auger Heating (AH), the energy gained by the recombination of an electron-hole pair is instead acquired by a second electron to reach a higher-energy level. After the generation of excited carrier distributions, AH is usually limited by the available phase space, hence II is thought to dominate at earlier times. As clear by the picture, only II can lead to carrier multiplication, both in CB and VB (same treatment can be done for electrons and holes).

With this general scheme in mind, I analyzed the experimental ΔA data at each time delay for the three different cases studied (high- and low-fluence $1.85\,\mu$m and $0.8\,\mu$m). As a reminder, for the VB the positive signal in the ΔA trace below 284.7 eV is attributed to the holes and for the CB the negative signal above 284.7 eV is attributed to the electrons. For each configuration, the sub-fs-resolved scans were averaged with lower-resolution scans to increase the signal-to-noise ratio.

To evaluate the number of carriers N_c, at each delay we summed the values of ΔA spectrum over the energy range in which we detected a transient signal, as described for the calculation of the ΔA lineouts

$$N_c \propto |\sum_i \Delta A(E_i)|. \tag{4.3}$$

Considering the SXR absorption as a measurement of the density of unoccupied electronic states (in absence of any other contribution to the XAFS spectrum), this sum (in absolute value) is directly proportional to the number of carriers present in the evaluated energy range. To extract the average kinetic energy $\widehat{E}_c$, the energy corresponding to the center-of-mass of the carrier distribution is calculated, both for holes and electrons, with the formula

$$\widehat{E}_c = \frac{\sum_i E_i \cdot \Delta A(E_i)}{\sum_i \Delta A(E_i)}. \tag{4.4}$$

Finally, the two quantities are plotted together versus time delay: a temporal window in which N_c increases while $\widehat{E}_c$ decreases would correspond to II and hence to carrier multiplication. The opposite behavior is instead expected for AH, with the N_c decreasing while $\widehat{E}_c$ increases.

The results for all the different combinations are shown in Fig. 4.13, 4.14 and 4.15 . We start with the $0.8\,\mu$m pump case to help the interpretation of the results. For this configuration, both electrons and holes are showing the same pattern: after the initial rise due to photoexcitation, there is a clear window ($\sim$ 40 fs) in which N_c keeps increasing while $\widehat{E}_c$ decreases (4.13). This scenario corresponds to the II scheme and results are in line with the findings of Gierz and coauthors [111]. If on one side the slightly lower pump fluence (5 vs 20 mJ/cm^2) of our case and the longer pulse duration (15 vs 8 fs) could be responsible for the longer window for II (40 vs 25 fs), it is interesting to observe that same result is obtained between graphite and graphene, demonstrating once again their similarity in terms of band structure and carrier dynamics. It is also important to highlight that holes and electrons are showing the same behavior, which was theoretically predicted but never confirmed with experiments.

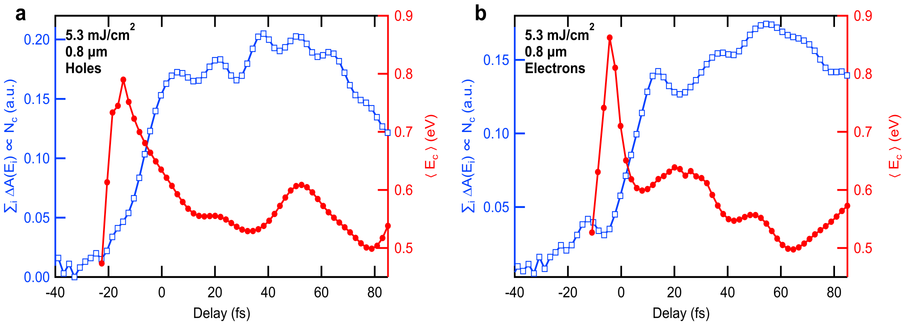

Figure 4.13: Carrier multiplication analysis for the measurements with 0.8 μm pump pulse, both for holes (a) and electrons (b). The two behavior are almost identical, with the number of carriers increasing for a time window longer than the pump pulse. At the same time, it is possible to identify a window for both cases in which the average kinetic energy decreases, hence in which II takes place.

The case of low-fluence 1.85 μm pump case is presented in Fig. 4.14. For the electrons, we can identify a similar trend to the one observed for the 0.8 μm case but with a shorter window ($\sim$ 25,fs), indicating again that II is dominating. The shorter time window can be explained in terms of the smaller phase space available for the electron to lose energy when using pump photon energy of 0.69 eV compared to 1.6 eV, where the electrons are distributed further away from the Dirac point. For the holes, the same trend can be observed only for an even shorter time window ($\sim$ 10 fs), after which the average kinetic energy rather increases, contradicting the II scheme and breaking the symmetry with the electron side. A possible reason for this is the presence of p-doping which would further limit the phase space available for the holes and accelerating the takeover of AH. It is worth to highlight here that with a similar pump photon energy (0.95 eV), Gierz et al. carried out the same experiments on graphene [163], concluding that no II was observed. We believe the reason they could not recognize a time window for impact ionization is the time resolution, due to the pump pulse duration of their experiment, definitively longer (100 fs) compared to our case.

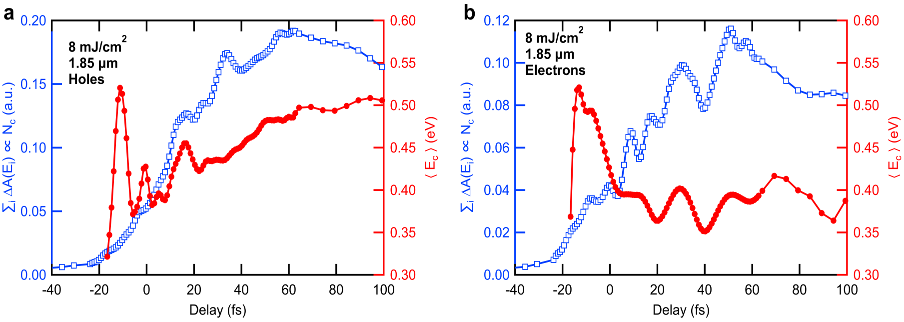

Figure 4.14: Carrier multiplication analysis for the measurements with low-fluence, $1.85\,\mu$m pump pulse, both for holes (a) and electrons (b). The electrons show a behavior similar to the $0.8\,\mu$m case, but carrier multiplication takes place on a shorter time window. For the holes, II is observed for a very short time window, after which the energy stays constant or rather increases. The asymmetry could be related to the presence of carrier doping, as predicted in [106].

Finally, for the high fluence case, we can observe again a similar trend for electrons and holes, but it can't be explained in terms of either II or AH. After the initial rise, both quantities are staying constant for the reported time delay range. Our interpretation is that at this very high fluence, the rate of both processes is so high that there is a competition between them, resulting in an almost constant number of carriers and average kinetic energy, until other processes, like carrier-phonon scattering, take place.

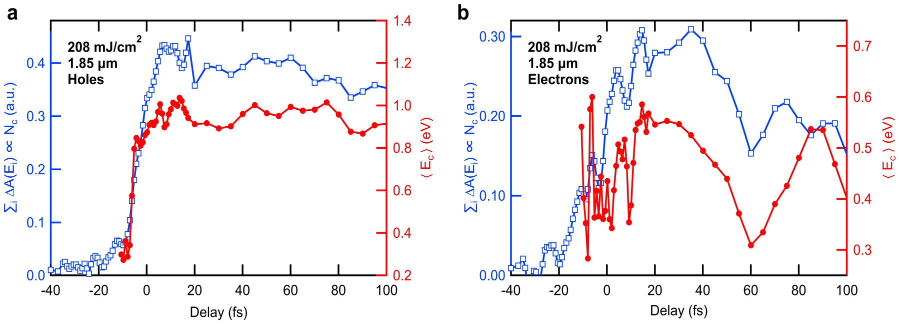

Figure 4.15: Carrier multiplication analysis for the measurements with high-fluence, 1.85 μm pump pulse, both for holes (a) and electrons (b). This case is fundamentally different from the previous two and it cannot be read in neither of the two schemes for carrier scattering (II and AH). The two mechanisms could have equivalent rate at this high fluence, resulting in a negligible net effect on both number of carrier and average kinetic energy.

4.2.3 Energy-dependent carrier lifetime

Exploiting the capability of XAFS spectroscopy to directly interrogate the band structure via the unoccupied electronic states of the material allows extracting information on the evolution of the carrier distribution in reciprocal space. Identifying in which state electrons and holes are created and through which channel (towards which valley or direction) they decay can give a complete description of the carrier dynamics, not always available in angularly-integrated detection scheme.

One interesting aspect is to study the energy dependence of the observed signal referring to photoexcited carriers. In our measurement, this translates in analyzing the transient features appearing in the ΔA trace without summing up all the energy pixels, but rather comparing them. An obvious bottleneck for applying this analysis to our measurements is the spectral resolution, which at the carbon K-edge has the nominal value of $\sim 0.3\,$eV, limiting the number of pixels that can be considered. To extract some meaningful information, I considered for this analysis only the high-fluence cases, both for the 95 (4.5) and 20 nm (4.9) thick sample, exhibiting the broadest transient signal.

For these measurements, while for the VB we have a uniform positive signal, for the CB it splits into a positive and negative contribution. The positive feature can be assigned to the excitation of carriers in the CB because they would block transitions from the inner 1s shell (state-blocking). The negative signal is instead opposite in sign, hence incompatible with a state-blocking picture for that energy range. On the other hand, the temporal evolution of this signal is in line with the other two features observed at the π^* edge, suggesting the same common nature, and it appears in the proximity of the M-point of the band structure, where the density of electronic states has a local maximum. We interpret this signal as the modification of the band structure (complex interplay of edge shift and/or broadening) induced by the high concentration of excited carriers (which explains why this effect is visible only for the experiments with high pump fluence). In conclusion, being the electron signal not broad enough to extract a meaningful energy dependence, for this analysis only the (VB) holes signal is considered.

Plotting the value of ΔA versus time delay for each pixel with detectable changes, one obtains the plot shown in Fig. 4.16a (here the case of the 95 nm sample is shown). The curves have all the same shape (fast rise and slower decay) and are definitively noisier than the one obtained when summing up all the pixels, but the general trend can still be discussed. Regarding the rise time, there is a clear dependence on energy (values are all related to the photon energy corresponding to the zero-crossing line the ΔA spectrum) for which the rise is slower for energies further away from the Dirac point. This can be explained in terms of band-filling, which is the saturation of available empty states reached by the pump photon energy for a high concentration of excited carriers, resulting in a blue-shift of absorption spectrum (the effect is well-known for semiconductor laser [164]). Another possible explanation is ultrafast carrier-carrier scattering processes (like AH, as discussed in the previous section), for which the distribution spreads over energy due to the high density of excited carriers.

If one focuses the attention on the decay, it is not difficult to identify that it is faster for energies further away from the Dirac point. The energy dependence of the decay time, or in general the excited carrier lifetime, has been the object of both theoretical [99] and experimental investigations [100] and relates directly to the shape of the band structure. The relation between the carrier lifetime in a 3D gas of interacting electrons is described by Landau's theory of Fermi liquids [101], for which

$$1/\tau \propto (E - E_F)^2. \tag{4.5}$$

Anyway, things behave differently when considering electrons in a periodic crystalline potential, for which it is important to consider that electronic states can have the same energy but a different position in the k-space, even if considering only the first Brillouin zone. In particular, Moos et al. [100] have shown with photoemission spectroscopy (ARPES) on graphite pumped by 800 nm light that anisotropy of carrier lifetime can show up in proximity of critical points of the band structure, like the saddle point present at the M point of the reciprocal lattice (see band structure 3.2).

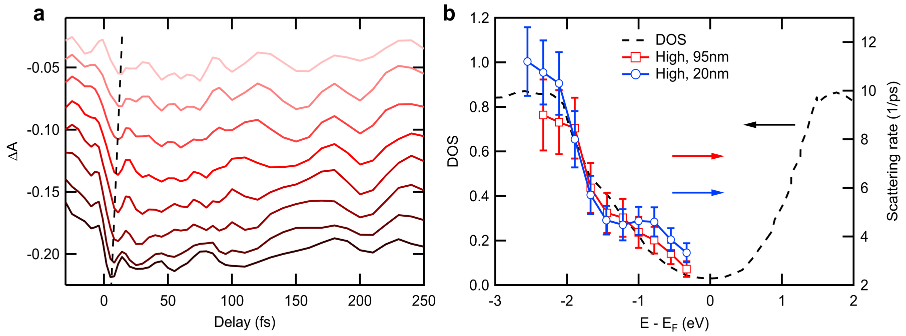

Figure 4.16: Energy-dependent carrier rise and decay time. a) shows a series of differential absorption curves, each one considering a single pixel involved in the hole transient signal for the high-fluence 95 nm case. The darkest color corresponds to the energy pixel closest to E_F, while the furthest energy pixel is given by the lighter color. The dashed line is to guide the eye over the energy-dependent rise time. In b) the obtained scattering rates are plotted against the DOS: the change in slope occurs in the proximity of the saddle point of the band structure at the M point (~ -2 eV). Error bars refer to uncertainty on the decay constant obtained by the numerical fit (see A.3).

To calculate the dependence of the scattering rate on the energy for the holes in our experiment, a single exponential fit is performed on all the energy pixels where a transient signal appears, as presented in Fig. 4.16a (an example of exponential fit of a single trace is reported in the App. A.3). The inverse of the decay constants obtained with the fit is then plotted against the energy axis, as shown in Fig. 4.16b for the two cases of 95 and 20 nm samples, together with the DOS corresponding to the VB. The scattering rate for both cases increases with increasing energy, denoting a shorter hole lifetime, until it changes slope for energies around 2.0 eV, where the DOS shows a maximum, corresponding to the saddle point at the M point of the k-space. This result is in line with the findings shown by Moos et al [100]. However, it is important to highlight that our analysis refers to the holes instead of electrons and confirms the XAFS potential to track carrier dynamics for both VB and CB in the same experiment.

4.2.4 Modeling the carrier distribution with Fermi-Dirac statistics

In Sec. 3.4 the general approach to model experimental XAFS spectra was introduced. It relies on the knowledge of the DOS of the material and the use of the FD distribution to describe the electron system. This distribution is described by the chemical potential μ_e and the temperature T_e of the thermodynamical system at equilibrium. The effect of photoexcitation is to create a concentration of carriers out-of-equilibrium, for which the FD statistics is not valid anymore. Nevertheless, the system will recover a thermodynamical equilibrium through carrier-carrier and carrier-phonon scattering on timescales which can be very fast [104], ending up in a state at a usually higher temperature than the initial one. Following the evolution of parameters like temperature and chemical potential can give important information on the photo-induced dynamics inside the material.

The starting point is the analytical fit used for the static XAFS spectrum, described in 3.4. Once a good set of fit parameters is found, we apply the same fit routine for the transient data, leaving only a few parameters free, like the temperature and the chemical potential. For this part, we focused our analysis on a narrow region around the π^* edge (± 2.5 eV), since only here we expect changes in carrier distribution due to the presence of the pump pulse. We expect the electronic system to be out-of-equilibrium for a certain temporal window right after photoexcitation, but thermalization has been observed in less than 100 fs [104], after which it is justified to assign again a temperature and a chemical potential to the system.

In Fig. 4.17a the retrieved temperature behavior, both for the high and low fluence case, is reported. In both cases there is a very fast rise due to the photoexcitation process, bringing the temperature to several thousands of K (respectively $\sim 2000\,\mathrm{K}$ in the low and $\sim 5000\,\mathrm{K}$ in high fluence case), followed by an exponential decay. The decay constant is the result of two underlying processes affecting the carrier temperature, namely scattering with SCOPs and lattice. In the next section, through the use of a numerical model, the interpretation of the temperature evolution will become clearer.

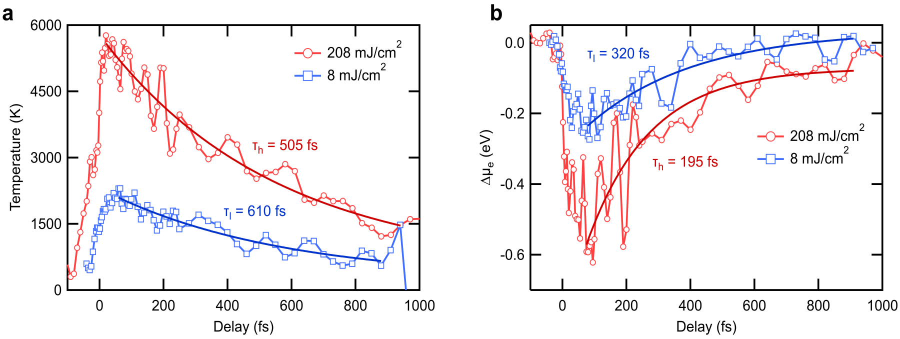

Figure 4.17: Temporal evolution of carrier temperature (a) and chemical potential (b) extracted from imposing a FD distribution to experimental data. Data are reported for the high and low fluence case, both with $1.85\,\mu$m pump pulse. For all the curves, the decay has been fitted with a single exponential and the resulting decay constant reported on the graph (τ_l stays for low fluence, τ_h for high).

The behavior of μ_e with time is presented in Fig. 4.17b. The rise time is again very fast around the zero time delay, result of the out-of-equilibrium condition of the system, while the recovery is faster than the one observed with the temperature (see decay constants reported in Fig. 4.17). The faster decay can be justified by the fact that the chemical potential rather depends on carrier density and its dynamics, so it manifests a smaller (or no) dependence on the slower scattering with the lattice. The dynamics of the chemical potential reflect the out-of-equilibrium state of the electron and hole distribution, but can also be related to the ultrafast modification of the band structure. For semimetals like graphite, in absence of a real band-gap, it is not correct to talk about effects like band-gap renormalization, but a rearrangement of the band structure due to the high concentration of excited carriers is expected [165]. On the other side, the amplitude of the effect (namely the maximum value in 4.17b), evaluated for these the two cases, seems to scale with the number of excited carriers according to the relation $\Delta E \sim N_e^{1/3}$, as expected for band-gap renormalization effects [77].

4.2.5 Three-temperature model

Modeling the electron (hole) gas system as a FD distribution allows us to assign statistical quantities like the temperature of the system, as seen in the previous section. Following photoexcitation, the hot electron system will reach very high temperature until undergoing thermalization processes which will bring the system back towards the initial thermodynamic state. The most dominant decay channels in graphite are carrier-carrier scattering (discussed in Sec. 4.2.2, $\sim 10-20\,\mathrm{fs}$ time scale) and carrier-phonon scattering resulting from the strong coupling with optical phonons (SCOPs, $\sim 200-300\,\mathrm{fs}$ time scale, extracting up to 90% of the excitation energy [102]), which can further decay by coupling to the lattice via phonon-phonon scattering ($\sim 1\,\mathrm{ps}$ time scale) [125, 114, 124].

A general procedure applied to solid-state pump-probe experiments to estimate the time scales and coupling strengths of carrier-phonon and/or phonon-phonon interaction is the so-called three-temperature model (3TM). In this model, three different systems are introduced (usually electrons, optical phonons, and lattice) and their temporal evolution is ruled by a system of differential equations. The adaptation of this model to our experimental findings is the result of a collaboration with Dr. Thomas Vasileiadis and Prof. Dr. Ralph Ernstorfer from Fritz Haber Institute in Berlin [166, 167].

The experimental evolution of the electronic temperature, extracted by modeling the experimental data with the FD distribution (Sec. 4.2.4), has been fitted with a 3TM in which graphite is composed of three, interacting heat baths: (1) the laser-excited hot electrons, (2) the strongly coupled optical phonons (SCOPs) and (3) the entire lattice. The 3TM can be expressed with a system of three coupled differential equations:

$$C_E \frac{dT_E}{dt} = -G_{E-SC} \cdot (T_E - T_{SC}) + S(t), \tag{4.6}$$

$$C_{SC} \frac{dT_{SC}}{dt} = G_{E-SC} \cdot (T_E - T_{SC}) - G_{ph-ph} \cdot (T_{SC} - T_L), \tag{4.7}$$

$$C_L \frac{dT_L}{dt} = G_{ph-ph} \cdot (T_{SC} - T_L), \tag{4.8}$$

where C_i are the heat capacities, T_i are the temperatures and the lower indices denote the heat bath (E, SC and L for the electrons, the SCOPs and the lattice, respectively). The $S(t)$ is a source term for the absorbed laser pulse, which is primarily exciting the electrons. The heat capacity of the electrons is given by:

$$C_E = \gamma \cdot T_E \tag{4.9}$$

with $\gamma = 2.5\,\mathrm{J/m^3K^2}$ based on published works [168]. In the model, the SCOPs have an energy of $\hbar\omega = 200\,\mathrm{meV}$ and their heat capacity is calculated according to the formula [124]:

$$C_{SC} = \frac{d}{dt} \frac{fN\hbar\omega}{e^{\hbar\omega/k_B T} - 1} \tag{4.10}$$

where $N = 3.4 \cdot 10^{29}\,\mathrm{m^{-3}}$ is the total number of vibrational modes per volume for graphite and f is the fraction corresponding to the SCOPs. Finally, the heat capacity of the lattice (C_L) is found from the work of E. Pop et al [169]. The equations of the 3TM are used for a nonlinear fitting of the experimental data, where the fitted parameters are the coupling constants (G_{E-SC} and G_{ph-ph}), the fraction of the SCOPs (f) and the laser fluence.

The comparison between the temperature profile extracted from the data and the nonlinear fit produced by the 3TM is presented in Fig. 4.18a. The electronic temperature is in excellent agreement with the temperature data, except for the initial time delays, where the profile is mainly dominated by the non-equilibrium carrier excitation induced by the pump pulse. The rising part can be included introducing a convolution with a Gaussian pulse simulating the photo-excitation.

Based on the fitting, SCOPs represent 0.24% of all the vibrational modes, they are excited by hot electrons with an energy transfer rate $G_{E-SC} = 2.8 \cdot 10^{16}\,\mathrm{W/Km^3}$ and they cool down by phonon-phonon coupling with an energy transfer rate $G_{ph-ph} = 5.5 \cdot 10^{16}\,\mathrm{W/Km^3}$. Fitting the modelled temperature evolution with a bi-exponential decay shows that the time-constants for heating and cooling of SCOPs are $\tau_1 = 120\,\text{fs}$ and $\tau_2 = 600\,\text{fs}$, respectively.

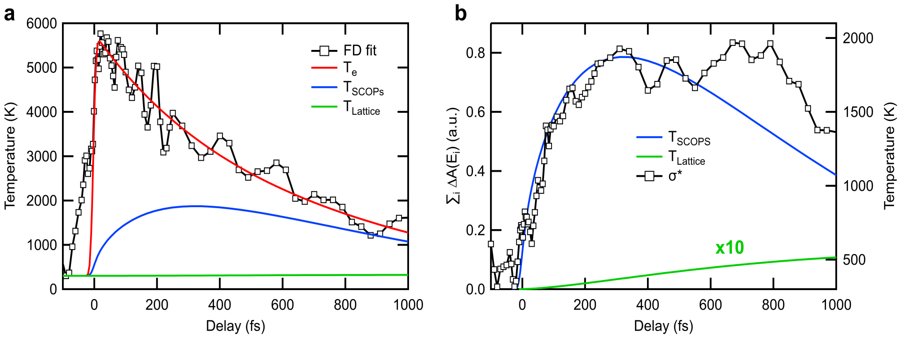

Figure 4.18: Results of the 3TM model and comparison with experimental data. In a), the behavior of the temperature for the electron, SCOPs and lattice system is reported, where the nonlinear fit obtained with the 3TM is in agreement with the temperature extracted from FD analysis. b) Comparison between temporal trends of ΔA detected at the σ^* edge and T_{SC} and T_L, denoting a close relation between the excitation of these phonon modes and the experimental findings.

The time constant for heating of SCOPs is very similar to the general rise time of the transient signal detected at the σ^* edge for the measurements with the high-fluence pump pulse. This strongly suggests the comparison between the temporal evolution of T_{SC} and T_L and the ΔA lineout for the σ^* (related to 4.5), as reported in Fig. 4.18b. Even though we are comparing distinct physical quantities, it is impressive the agreement of the two curves ($\Delta A(\sigma^*)$ and T_{SC}), while after about $\sim 600\,\text{fs}$, they start to differ. Interestingly, this is the time delay after which the temperature of the lattice (i.e. the population of acoustic phonons) becomes significant, as the result of the decay of SCOPs.

In our interpretation, this is clear evidence that the nature of the transient signal at the σ^* edge is related with the excitation of phonons, dominated by the excitation of SCOPs but accompanied by a minor contribution from the acoustic phonons, only becoming consistent for time delays after 600 fs. This relation is further investigated in Sec. 4.2.7 and 4.2.8.

4.2.6 Coherent vs incoherent phonon excitation

The results of the 3TM suggest a close connection between the temporal evolution of the phonon excitation, both for SCOPs and acoustic phonons, and the measured ΔA signal at the σ^* edge. Before entering into the analysis of the observed signal, a brief discussion on possible mechanisms for phonon excitation in graphite is reported, analyzing the interaction of the lattice with both the few-optical-cycle pump pulse and the excited carrier distribution. The direct phonon excitation via IR photon absorption is not reported in this discussion because not related to our experimental findings.

Experimental evidence of coherent vibrations of the lattice driven by femtosecond laser pulses was reported since the early 1990s in pump-probe measurements of differential transmissivity or reflectivity [118, 170, 171, 172]. The induced coherent vibrations all obeyed Raman transitions' selection rules (i.e. Raman-active modes) and they have been produced in materials with very different electronic (insulators, semiconductors, metals) and structural properties. On the other hand, different behavior was observed between transparent and opaque materials [118, 170], which opened the search for a theory describing this general phenomenon of light-matter interaction.

The first mechanisms suggested explaining the laser-induced coherent excitation of phonons are Impulsive Stimulated Raman Scattering (ISRS) and Displacive Excitation of Coherent Phonon (DECP). In the ISRS scheme [118, 173], if a crystal (the same argument applies to molecular targets too) interacts with a broadband laser pulse which duration is shorter than the period of the phonon modes of the crystal, a vibrational coherence can be induced in the material. The driving force (the light pulse) acts on the atoms inducing non-linear polarizability, responsible for the impulsive excitation of coherent vibrations for the case of ultrashort pulses, resulting in a sin-like oscillation (derived from the equation of motion including the laser driving force [118]). This mechanism applies to every transparent medium, in which case the laser pulse induces the vibrational coherence via coupling to electronic virtual states (as by definition of Raman scattering). The extension of the ISRS scheme to absorbing media, where light is in resonance with electronic excitation, resulted to be not straightforward.

For the case of opaque materials, the DECP scheme was proposed [119]. The carrier promotion from VB (bonding character) to CB (antibonding character) weakens the atomic bonds and induces a change in the equilibrium nuclear coordinates which leads to the minimization of the total energy of the system. This movement, initiated by the quasi-instantaneous shift induced by the e-h formation, induces the coherent vibration of the lattice around the new atomic positions only for fully-symmetric mode respect to the nuclear coordinates. The amplitude of the oscillations depends on the concentration of excited carriers and the phase is expected to be 0^o (cos-like oscillation, due to the step-like nature of the excitation force).

A unified mechanism for the coherent phonon excitation has been proposed, which considers the ISRS and DECP interactions as two different aspects of the same light-matter interaction, for the cases of transparent and opaque materials respectively, but allowing any intermediate configuration [120]. In this generalized scheme, oscillations with phase intermediate between $\phi = 0$ and $\phi = \pm\frac{\pi}{2}$ are allowed, as observed in many experiments. The interplay between excited carrier distribution and lattice vibrations is considered [174], and responsible of many interesting observed features, like frequency shifts [175], lineshape modification [176] or interaction between different phonon modes [177].

The laser-induced coherent excitation is not the only possible mechanism to excite phonon in the material. The energy deposited in the electron system via photoexcitation can decay through carrier-phonon scattering, involving both optical and acoustic vibrational modes [178, 179]. As already discussed in Sec. 1.2.1 and 1.2.2, graphite is a clear example of such connection between the electron and lattice degrees of freedom. Experiments have reported a strong coupling of the electron excitation with optical phonons (namely the E_{2g} and A_1' mode), in which channel $\sim 90\%$ of the deposited energy decay in less than 500 fs [102]. This excitation mechanism, being based on scattering processes, is not deterministic, hence can only give rise to an incoherent contribution to phonon-related features.

In graphite, experimental proofs of coherent and incoherent phonon excitation have been reported. Laser-induced coherent excitation of Raman-active E_{2g} modes (with periods of 21 and 770 fs) have been experimentally reported [117, 121] and numerically simulated [180], while on a slower (picosecond) time scale even coherent out-of-plane modes (the breathing mode [125]) have been reported. The incoherent phonon excitation obtained through EPC have been instead reported in experiments of UED ([125, 114]) and combined time-resolved Raman and ARPES spectroscopy ([124]), identifying the E_{2g} and A'_1 mode as the main characters of the EPC.

For our experimental conditions, we expect to observe signatures of both coherent and incoherent excitation of phonon modes in graphite in the time-resolved XAFS experiments. The sub-2-cycle IR pump pulse is resonant with electronic excitation and at the same time shorter than any vibrational mode in graphite. Hence, our conditions allow exciting both the E_{2g} mode via ISRS and the A'_1 mode via DECP. We expect to detect a signal similar to the one obtained in the experiments of time-resolved UED ([125, 181], where phonon modes have been identified through time-domain analysis of the measured oscillatory component superimposed to transient incoherent contribution. Being the E_{2g} and A'_1 mode fast compared to the time delay range scanned in our measurements, the changes in the detected coherent contribution could also provide information on phonon dynamics (i.e. decay). The signal observed at the σ^* edge is a good candidate for such analysis, which is described in the Sec. 4.2.7 and 4.2.8.

4.2.7 Incoherent phonon excitation: DOS modification

The temporal evolution pump-induced transient feature detected in the proximity of the σ^* peak has already been compared with the excitation of optical and acoustic phonons in Sec. 4.2.5. In light of this comparison, we interpret this feature as the modification of the band structure induced by the excitation of phonons. This is justified by its time evolution (in line with the excitation of SCOPs and acoustic phonons reported by the 3TM results=, the nearly-zero probability of directly exciting carriers with the pump pulse directly from the VB (more than ten absorbed photons would be needed) or the absence of the typical state-blocking spectral feature (as the one observed at the π^* edge). In general, for the strong coupling condition of graphite, it is expected to have phonon-induced effects for the high concentration of excited carriers. Moreover, it was already suggested as a possible mechanism by van der Veen et al. [123] in an ultrafast electron energy-loss spectroscopy experiment on graphite with picosecond resolution. We interpret this modification of the band structure as the signature of incoherent excitation of phonons via EPC.

This feature is clearly visible in the experiment with high-fluence (Fig. 4.5) and medium-fluence (Fig. A.1) 1.85 μm pump pulse and still detectable in the measurement with same pump photon energy but lower fluence (Fig. 4.3), while it was never detected in the experiments with the 0.8 μm pump pulse. For the rest of the discussion, we will consider the more interesting case of high-fluence 1.85 μm pump pulse, while still applying the same analysis to the low fluence case for comparison. The signal presents a strong feature (almost 20% change in absorption) peaked at 291 eV in correspondence of the inflection point of the edge but extending over a range of about 3 eV (see Fig. 4.2.7). Here a decomposition of the detected signal in terms of two different contributions, namely an edge shift and broadening, is presented [77]. The contribution related to the edge shift is calculated with a fit routine applied to the SXR absorption spectrum at each time delay, while the broadening one is considered as the remaining signal once the other contribution is subtracted.

To evaluate the edge shift, at each delay the fit routine applies a rigid energy shift to the static (i.e. no pump pulse) absorption spectrum such that the corresponding differential absorption spectrum results in the same amplitude value of the measured signal at the σ^* edge (see Fig. 4.2.7a for clarification). Letting the fit routine run over the full experiment, the edge shift (the "pumped" edge position minus the static one) is evaluated as a function of time delay (see Fig. 4.2.7b). The σ^* edge shifts up to 160 meV towards lower energies for the high fluence configuration, while we can detect a shift of maximum 20 meV for the low fluence case, the result of the lower phonon excitation compared to the high fluence case.

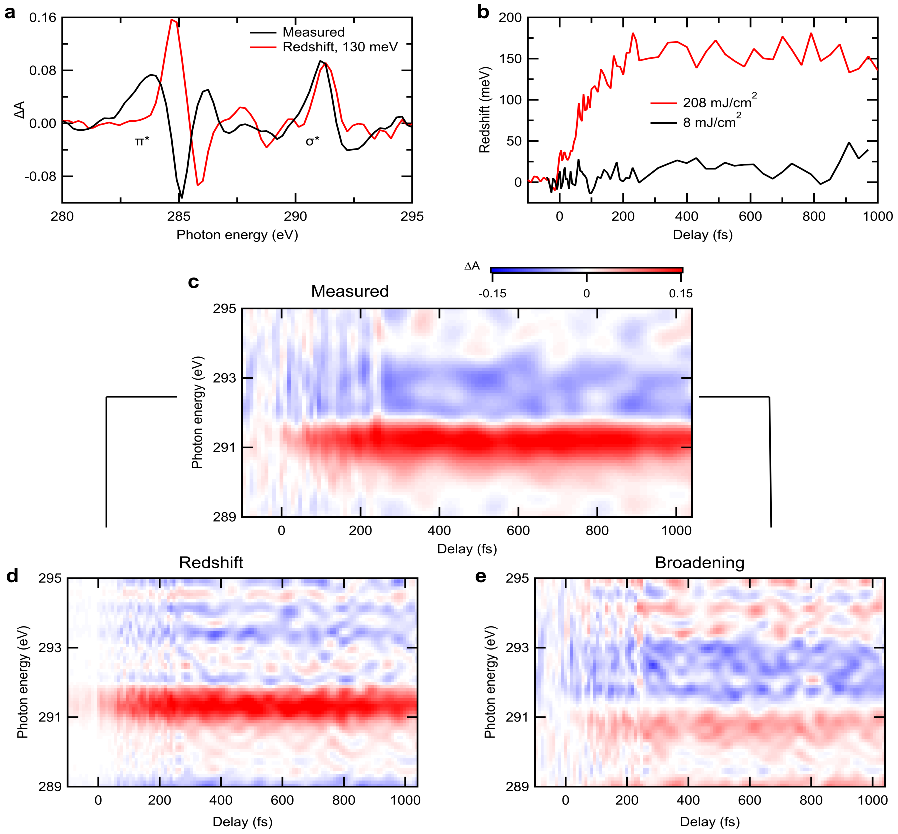

Figure 4.19: Spectral decomposition of measured differential absorption signal detected at the σ^* edge. a) presents the measured spectrum together with a simulation of the signal produced by a redshift of $130\,$meV, able to reproduce only the feature around $291\,$eV. Applying the fit routine, a value of edge shift can be extracted per each delay value, producing the curves in b). Finally, the measured ΔA trace (c) can be decomposed in the rigid redshift component (d) and a remaining signal, attributed to edge broadening (e).

It is important to highlight the fact that, while the redshift can reproduce the feature at the σ^* edge, we cannot say the same for the region around the π /π^* edge, where it produces a feature opposite in sign with the measured data (see Fig. a). Our explanation, in line with the proposal by van der Veen et al. in [123], goes back to the nature of this signal: band structure modification due to excitation of phonon modes. These strongly-coupled modes, which have been identified with a Fourier analysis (see Sec. 4.2.8) and cross-checked with related works performed on graphite in similar condition [114], are producing atomic motion taking place mainly inside the graphene layers, where the covalent σ bonds lay. This motion consists in a perturbation of the σ bonds bigger compared to what happens to the π bonds, oriented perpendicularly to the graphene sheets, then resulting in a stronger modification of the SXR absorption at the σ^* edge.

If the redshift contribution (Fig. 4.2.7d) is removed from the measured ΔA trace, what is left is a feature, with both positive and negative sides, mostly symmetric around the inflection point (see Fig. 4.2.7e). Such features can be reproduced if the spectrum is convoluted with a Gaussian function to simulate a broadening effect and are usually present when heating mechanisms are involved or more generally disorder (like vibrations) is induced in the crystal, as in the case of the Debye-Waller effect.

Finally, we attempted to numerically simulate the effect of phonons on XAFS spectrum. Through the use of the FDMNES package, the lattice distortion induced by the two dominant phonon modes involved in EPC (the E_{2g} and A_1' mode) is simulated by redefining the lattice structure according to the mode representation reported in [113]. The modified XAFS spectrum is considered as a "pumped" case, from which a differential absorption is calculated as defined for all the tr-XAFS measurements here reported. The results are summarized in Fig. 4.20 for three different displacements ($0.75, 1$ and $3\,$pm). The changes induced by the E_{2g} mode are more similar to the measured Δa spectrum (here reported is the time-delay-integrated Δa spectrum for the high-fluence case) compared to the A_1' case, with the case for $1.5\,$pm displacement matching quite well with measured data. Interestingly, both modes seem to induce changes also at the π^* edge. Further investigations are needed to implement a numerical fit routine to extract meaningful comparison between the data and simulated lattice vibrations.

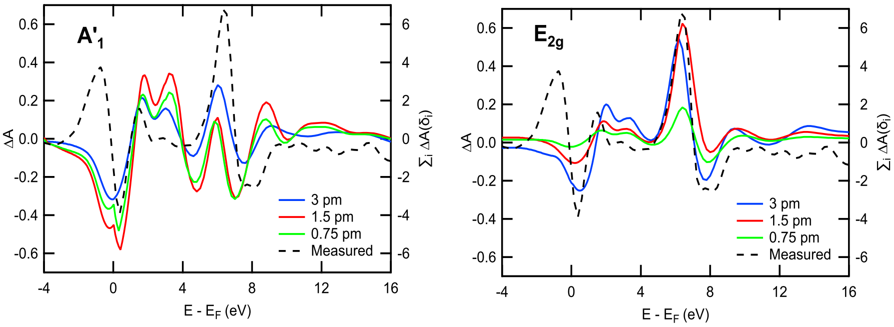

Figure 4.20: Simulation of phonon-induced modification of XAFS spectrum with FDMNES. The two strongly-coupled vibrational modes E_{2g} and A_1' have been simulated, choosing three different values for atomic displacements ($0.75, 1$ and $3\,$pm) and the resulting differential absorption evaluated. For comparison, the time-delay integrated ΔA spectrum for the high-fluence case is reported. Figure is provided by Dr. Themistoklis Sidiropoulos.

4.2.8 Coherent phonon excitation: time-domain analysis

The temporal evolution of the transient signal detected at the σ^* edge has been shown in Fig. 4.5 (considering the high-fluence $1.85\,\mu$m pump case showing the clearest feature) and discussed in the previous section (Fig. 4.2.7). By looking at the lineout obtained when summing up the intensity for all the pixels showing a transient signal, it is not difficult to identify an oscillatory behavior on top of the slow exponential rise, as expected for light-induced coherent excitation of phonon modes. The spectral analysis of these oscillations is presented here, providing information on the involved vibrational modes and their dynamics.

For the spectral analysis, only the three pixels around $291.3\,$eV showing the strongest transient signal are considered to increase the signal-to-noise ratio in the following analysis: the sum of their intensities produces the black curve in Fig. 4.21a below. Then, the curve is interpolated on an equally spaced time delay axis (acquired time delay axis is not uniform) and a polynomial fit is subtracted to reduce the DC component obtained in the Fourier space, as generally done in time-resolved ISRS spectroscopy (see Fig. 4.21a). The result is the red curve in Fig. 4.21b, which presents different spectral components: for smaller delay values frequency is higher, while it becomes lower when going towards the second half of the trace.

The long integration time needed to acquire low-noise data (about 25 minutes per each time delay value) does not allow scanning over a long delay range with high temporal resolution. For this reason, the delay step size was changed during the experiment (the high-fluence 1.85 μm pump case), with a time resolution higher around the zero time delay and lower towards the end of the scan, assuming that the fast (electronic) dynamics would take place earlier than the slow (vibrational) ones. Precisely, the step size during the scan corresponds to:

- 5 fs in the $0 - 100$ fs range
- 10 fs in the $100 - 250$ fs range
- 30 fs in the $250 - 1000$ fs range.

It is important to stress that the delay step size chosen for the measurement sets a limit to the higher frequency component we can retrieve in the Fourier analysis. The effect of changing the step size becomes clear when observing the data shown in Fig. 4.21b: at 250 fs there is a sharp change, after which we lose resolution on the high-frequency components and only the low frequencies become detectable.

Using the discrete Fourier transform algorithm, we obtain the Fourier amplitude spectrum shown in Fig. 4.21c. It presents a series of peaks which are in good agreement with the frequencies of the E_{2g} (45 THz) and A_1' (35 THz) vibrational modes of graphite and to the products of their decays, as described by Stern et al. in [114]. Slight modifications of the phonon frequencies can be induced by the high concentration of excited carriers for the high-fluence case studied here. These modes are SCOPs and they constitute the main energy decay channel in graphite after photoexcitation from π to π^* band.

If this analysis allows us to retrieve the frequencies of the involved phonon modes with a good spectral resolution, it doesn't provide any information on their temporal dependence. To access any dynamics, we performed the so-called short-time discrete Fourier transform analysis, which consists of a Fourier transform performed on a moving time window sliding over the temporal axis. The shorter delay axis over which the Fourier transform operation is evaluated results in a lower final spectral resolution but allows to follow frequency changes

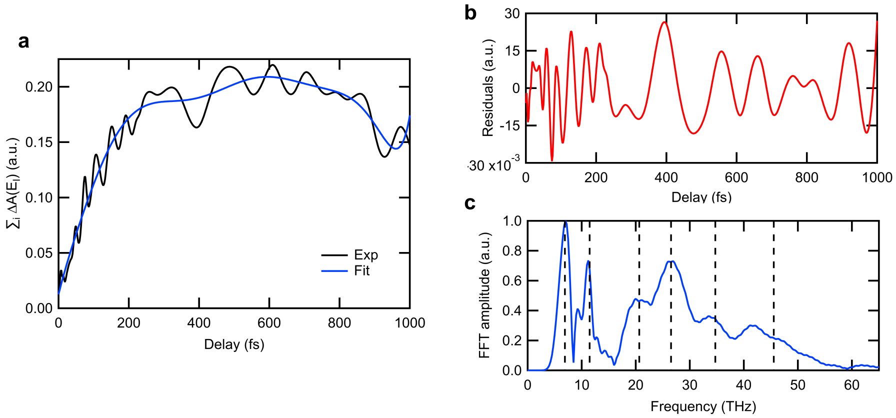

Figure 4.21: Discrete Fourier transform analysis of the differential absorption signal detected at the σ^* edge. a) The signal is fitted with a polynomial function over the time delay range, which is then subtracted from the measured lineout to highlight its oscillatory part, shown in b). This trace is then Fourier-transformed to obtain the amplitude spectrum in c). The dashed lines correspond to the frequencies of the E_{2g} and A_1' together with the products of their decay, as indicated in [114].

over the measured range. It is easy to deduce that the choice of the window length is important and related to the expected frequency values.

In our case, we know from the spectrum that frequencies from 7 up to 45 THz are involved, with the high frequencies appearing before the low ones. Considering this, we found the best choice is to have a window Δ with a varying length, dictated by the following relation:

$$\Delta = (0 + j * a,\ 100 + j * b)\ fs \tag{4.11}$$

where j is an index that moves the window over the time delay axis and sets the desired final resolution, while a and b are time-delay coefficients that adjust the rate at which the window length changes. A good choice of parameter for our case is to set $a = 6.25$ fs and $b = 12.5$ fs, which results in a window length that goes from 100 up to 550 fs. To define the new delay axis for the final plot, at every step the time delay value is defined as the center of the window.

The obtained results are presented in Fig. 4.22, showing a clear temporal trend of the frequency content. In the first 100 fs, spectral content is detected between 30 and 50 THz, corresponding to the superposition of E_{2g} and A_1' mode, confirming the ultrafast EPC in graphite. The former mode is Raman-active, so it can be the result of coherent excitation via ISRS. The latter is a fully-symmetric mode whose coherent excitation in graphite has never been observed before: the high-pump-fluence conditions of our experiment suggest a coherent excitation of this mode via the DECP mechanism.

Between 100 and 250 fs, most of the spectral content has already moved to the $15 - 30$ THz region. This result can be explained as the combination of two different reasons: first, the bigger step size in this time delay window (10 fs) doesn't allow a proper detection of frequencies higher than 30 THz resulting in a decreasing amplitude; second, these modes are already decaying towards lower frequency acoustic modes, as indicated in [114]. Both modes can decay creating two phonons of same energy but opposite wave-vector in the lower-energy acoustic branches: for the E_{2g} mode this can happen along with both ΓK and ΓM directions, while for the A_1' mode the ΓK is preferred [114]. The frequencies of the decay products (between 19 and 24 THz) are in good agreement with FFT results for this time window. Also, results reveal that the decay process takes place on an unexpectedly fast timescale if we compare these numbers to the findings of Stern et al. (corresponding to decay times of about 1 ps). The faster decay mechanism can be attributed to the higher pump fluence used in our experiment (about 1 order of magnitude higher than [114]), which produces a higher phonon density, leading to an acceleration of their decay process.

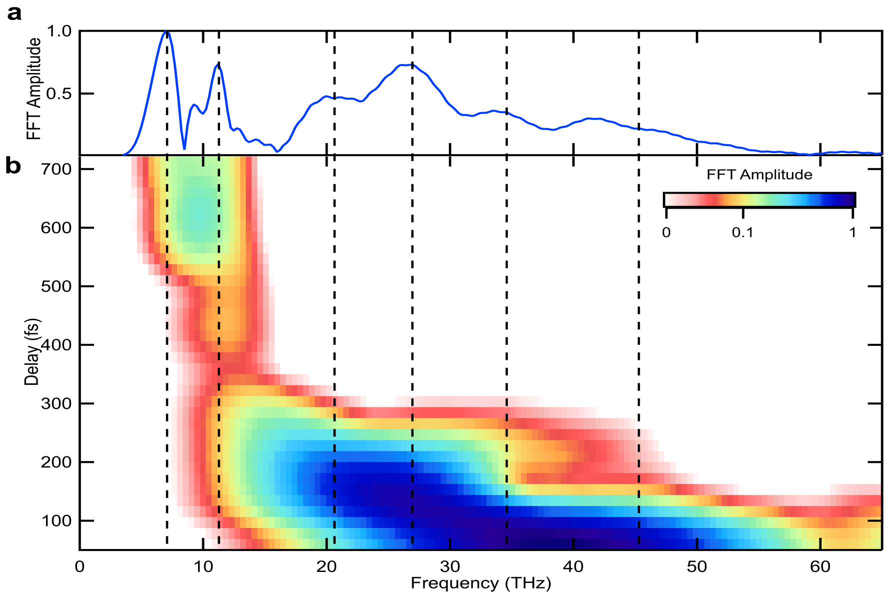

Figure 4.22: Phonon dynamics studied via STFT analysis. From the comparison of the 1D spectrum in a) and the 2D map resulting from the STFT, we can extract the time evolution of the excited phonon modes. The E_{2g} and A_1' modes present an ultrafast decay already on the first $150-200$ fs, while acoustic modes are efficiently excited only after 500 fs.

From 250 fs up to the end, the step size (30 fs) doesn't allow efficiently detecting frequencies above $15-20$ THz, thus about the E_{2g} and A_1' mode and their primary decay products. On the other side, an interesting feature appears at low frequencies ($7-11$ THz) in the graph around 500 fs which increases in amplitude towards the end of the detected range. Comparing the frequency values again with literature [114], numbers are in good agreement with the frequencies of secondary products of the decay of E_{2g} and A_1' mode, when the phonon populations move towards the lower frequency region of the acoustic phonon bands (see phonon dispersion band in Fig. 1.6 and data in [114]). In line with the previous observation regarding the primary decay product, also here the observed timescale results to be faster than the expected one, due again to the higher density of excited phonons via EPC.

The interpretation of the STFT results in terms of the excitation of different phonon modes, each with its temporal evolution, is also supported by a numerical fit of the measured ΔA signal at the σ^* edge as reported in Fig. 4.23. The fit function is composed by the same polynomial function used in 4.21 plus the sum of two sine waves, with frequencies varying for the three temporal region discussed before ($0-100\,\mathrm{fs}$, $100-250\,\mathrm{fs}$ and $250-1000\,\mathrm{fs}$). The frequencies of the phonon modes are used as the initial guess for the fit parameters. The excellent agreement between fit and experimental data (except for the region $250-500\,\mathrm{fs}$, as revealed from the STFT analysis) and between the retrieved frequencies (4.23) and the values from literature gives additional strength to our interpretation of the experimental results.

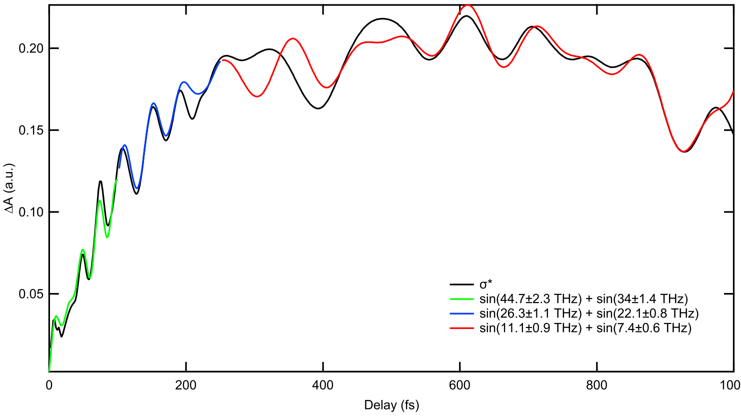

Figure 4.23: Reconstruction of the oscillatory component of the ΔA signal at the σ^* edge. For three different time windows ($0-100\,\mathrm{fs}$, $100-250\,\mathrm{fs}$ and $250-1000\,\mathrm{fs}$), the oscillatory component is reproduced by the sum of two sine waves, where the frequencies of the phonon modes obtained in 4.21 have been used as initial guess. The frequencies obtained from the fit are in good agreement with values taken from literature for the E_{2g} and A_1' mode and their decay products.

4.3 Conclusions

In this final chapter, the results of the experimental campaign of time-resolved XAFS on graphite have been presented and discussed. The capabilities of XAFS spectroscopy to access information on the electronic and lattice structure of the material have been combined with an IR, few-cycle, CEP-stable pump pulse, which is resonant with electronic excitation from the top of the valence (π) band to the bottom of the conduction (π^*) band. Two different pump wavelengths (1.85 and $0.8\,\mu$m) and different pump fluences (from 1 up to $200\,\mathrm{mJ/cm^2}$) have been used to get a deeper insight on the observed dynamics.

The differential absorption spectrum ΔA obtained as a function of the delay between pump and probe (4.2) presents two groups of transient features, evolving with different characteristic times. A comparison with the static absorption spectrum of graphite allows associating these features with the π^* and the σ^* absorption edges. The group of spectral features at the π^* edge, showing both increase and decrease of SXR absorption, has been interpreted in terms of state-blocking (excited electrons in CB decrease absorption for these energies, opposite for the holes in VB) together with an ultrafast carrier-dependent modification of the band structure, responsible for the extra positive signal around $\sim 286\,\mathrm{eV}$. The transient signal appearing at the σ^* edge shows a slower build-up time respect to the π^* one and has been explained as a combination of edge shift and broadening induced by phonon excitation.

The analysis of the rise of the transient feature at the π^* edge revealed a modulation of the signal oscillating at laser frequency both for holes and electrons, confirmed by the data obtained at two different pump wavelengths. With the help of DFT calculations, the modulation is explained in terms of the metallic response of the nearly-free carriers to the phase-stable electric field of the pump pulse, which drives carrier motion on a sub-optical-cycle timescale.

By following the temporal evolution of the number of carriers (proportional to the amplitude of the transient signal) and their average kinetic energy (respect to the Fermi energy) on the first tens of fs after photoexcitation, insight on the mechanisms dominating carrier-carrier scattering has been obtained. For low pump fluences (below $10\,\mathrm{mJ/cm^2}$) and both pump wavelengths, Impact Ionization has been found to dominate over Auger Heating for a short time window ($30-40\,\mathrm{fs}$) after the pump arrival, producing a carrier multiplication effect. For the case of high pump fluence, no clear evidence of one dominating mechanism is observed, most likely due to the extremely high excitation density which increases the rate of Auger processes.

Modeling the experimental data with FD statistics allows extracting information on the carrier distribution, like the temperature of the carrier system. The temperature evolution extracted via numerical fit is then reproduced by a three-temperature model describing the interaction of the excited electron system with two thermal baths, corresponding to optical phonons and the lattice. The energy transfer rate from the electron to the optical phonon system and from this last one to the lattice system are obtained from this model.

The temporal evolution of the excitation of optical phonons is in agreement with the transient signal observed at the σ^* edge, supporting the interpretation of a phonon-induced modification of the absorption edge. Preliminary results based on DFT-based numerical calculations trying to simulate the effect of vibrations on the XAFS spectrum show further support to this interpretation. The transient feature observed at the σ^* edge, dominated by the incoherent excitation of optical phonons via strong electron-phonon coupling, presents a modulation with frequency changing over the measured time delay region. This modulation reveals the coherent contribution to the phonon-induced signal, related to the pump-induced coherent excitation of the Raman-active E_{2g} via impulsive Raman scattering and the fully-symmetric A_1' modes via displacive excitation. A Fourier analysis of the coherent modulation allows identifying the excitation of the E_{2g} and A_1' mode as well as their decay products.

Chapter 5

Summary and Outlook

5.1 Summary

The results accomplished during my Ph.D. project are the fruit of the application of a powerful experimental technique like attosecond-resolved X-ray absorption spectroscopy to the study of carrier and structural dynamics in a highly-interesting material like graphite in real-time. We employed for the first time (along with the work reported in [83]) attosecond XAFS spectroscopy on a solid-state target and report, for the first time, a comprehensive study of ultrafast dynamics in graphite involving both the charge carriers and the lattice, from the sub-fs up to the ps regime.

The first Chap. (1) aims at providing the necessary background in which this thesis project has been developed. The new research field of attoscience is presented, with particular attention to the established process to generate attosecond pulses (high-order harmonic generation (HHG)). The most significant applications using attosecond pulses to study electron dynamics on atoms, molecules, and solids are reviewed, highlighting the strong impact attoscience had on the study of ultrafast phenomena. In the second part, the most interesting properties of graphite are presented together with a review of the most representative experiments investigating ultrafast carrier and structural dynamics. With the help of a short description of the experimental techniques used, the general picture of ultrafast dynamics in graphite following photoexcitation of carriers from valence to conduction band is described: the excited carrier distribution thermalizes through carrier-carrier scattering in the first tens of fs, after which it loses energy via a strong coupling to optical phonons, which finally further decay by coupling to the lattice.

A detailed presentation of the experimental setup used for time-resolved X-ray absorption spectroscopy has been reported in Chap. 2. The important features of the laser system needed to drive the HHG process are discussed. The vacuum system needed for generation, propagation, and detection of attosecond SXR pulses is described in detail. Ultrabroadband spectra supporting Fourier transform limit of less than the atomic unit of time (24 as) are produced by focusing the 1.85 μm, few-cycle, phase-stable laser pulse in a gas cell filled with high pressures of helium ($10 - 12$ bar). The SXR beam is refocused using an ellipsoidal mirror and detected with a home-built spectrograph (resolution of 0.3 eV at 300 eV). The source flux is such that $1.6 \cdot 10^7$ ph/s impinge on the experimental target. The attosecond SXR pulses are synchronized with an infrared pulse constituting the pump beam for time-resolved experiments. A replica of the HHG driver or its second harmonic can be used as a pump, which is recombined collinearly or with a small angle with the SXR probe. Finally, a temporal characterization of the HHG emission is presented through an attosecond streaking experiment. The results are showing that isolated attosecond pulses are produced per each laser shot with a duration of 165 as due to the intrinsic dispersion of the HHG process.

In Chap. 3 the X-ray absorption fine-structure spectroscopy technique is described. Starting from its fundamentals, the powerful capabilities of this technique to obtain information on both the electronic and lattice structure with element-specificity are discussed. The implementation of XAFS spectroscopy with HHG-based sources allows increasing considerably the temporal resolution compared to the case of large-scale X-ray sources like synchrotron or FEL facilities. Attosecond XAFS has been performed with our experimental setup in graphite to probe the first unoccupied electronic bands (π^* and σ^*) and to retrieve the distances of the first four neighboring atoms, resulting in good agreement with data collected at synchrotron sources. In the end, a description of a numerical approach to model the XAFS spectra based on DFT calculations is presented.

The results of the experimental investigations of carrier and structural dynamics in graphite via time-resolved XAFS absorption spectroscopy are contained in Chap. 4. Graphite is pumped by a few-cycle IR pump pulse resonant with electronic excitation from valence (π) to conduction (π^*) band. Two main features appear in the differential absorption spectrum, located in the proximity of the π^* and σ^* absorption edges, evolving with different timescales as a function of the time delay between pump and probe. The first is interpreted as the creation of electron and hole populations combined with an ultrafast modification of the band structure due to the presence of excited carriers. The second is instead explained in terms of a slower phonon-induced modification of the band structure, consequence of the strong electron-phonon coupling (EPC) happening in graphite after $\pi - \pi^*$ excitation.

From the analysis of time-resolved data taken at different pump fluences (from 1 up to $200\,\mathrm{mJ/cm^2}$) and two different pump wavelengths (1.85 and $0.8\,\mu$m), deep insights are obtained on dynamics involving both the charge carriers and the lattice. The sub-cycle response of the carriers to the intense electric field carried by the pump pulse is observed for the first time in graphite, revealing a nearly-metallic behavior. Evidence of Auger scattering processes (namely Impact Ionization) have been found to dominate carrier-carrier scattering on the first tens of fs after photoexcitation, leading to the first observation of carrier multiplication in graphite. The evolution of the carrier population is described in terms of a FD distribution, from which statistical quantities like the temperature of the electron system can be extracted. A three-temperature model has been used to describe the electron-phonon and phonon-lattice coupling, providing an estimation of the energy transfer rate between these systems. The temporal evolution of the excitation of optical phonons is in line with the transient signal observed at the σ^*, supporting the interpretation of a phonon-induced modification of the band structure. Finally, a Fourier analysis of the signal at σ^* reveals a coherent contribution to the phonon-induced signal, from which the vibrational modes and their dynamics can be studied.

In conclusion, the work presented in this thesis aims at being a reference for the application of X-ray spectroscopy with attosecond pulses in condensed matter, providing access to the investigation of carrier and lattice dynamics in real-time with element-specificity.

5.2 Outlook

In the light of the results presented in this thesis, here an outlook section is reported to discuss possible future directions of investigation. In the first part, possible upgrades of the experimental setup will be discussed to improve the sensitivity and extend the capabilities of attosecond XAFS spectroscopy. In the second part, the focus of the discussion is moved to possible applications of this technique to the study of ultrafast dynamics.

The experimental setup has proved to be a high-stability femtosecond IR pump - attosecond SXR probe scheme capable to perform experiments with sub-fs resolution on timescales of tens of hours. For future applications, the system would benefit from an increase of SXR flux, which would allow reducing the acquisition time for the experiments. To achieve this, higher pulse energy for the HHG driver is needed. The increase in pulse energy can come from higher Ti:Sa output, adjustment of the wavelength conversion process or new pulse compression scheme (photonic crystal fibers show superior performances compared to hollow-core fibers but are restricted, to date, to lower input pulse energy). The increase of the cutoff energy of the SXR spectrum to higher photon energies, completely covering the Oxygen K-edge for example, would extend the spectroscopic possibilities to new materials, hence to new physics. As described in Chap. 2, the most promising approach is to exploit the ponderomotive scaling of the HHG process, i.e. using a longer-wavelength driver. Finally, recent advances have been reported on driving the HHG process in a two-color field, which has proven the possibility to increase both the flux and the cutoff energy [182, 183]. In our case, the leftover 800 nm at the TOPAS output, the 1.3 μm signal of the OPA process or a weak second- or third-harmonic of the 1.85 μm can be used as second color field.

Another improvement of the experimental setup would be to increase the spectral resolution of the spectrograph, which could be crucial to observe fine spectral features in experiments. At the moment, the nominal resolution at the Carbon K-edge (284 eV) is about 0.3 eV, which is not too far respect to the pump photon energy if a replica of the HHG driver is used. Improving spectral resolution is not an easy task for the availability of optics in this energy range, hence a completely new design of the spectrograph (including a longer distance between grating and camera with respect to the actual setup, or a tunable slit) would be needed. New possibilities for experiments could also come from increasing the wavelength tunability of the pump pulse. For experiments requiring a phase-stable pump pulse, one possibility is to perform spectral broadening in a photonic crystal fiber, which has proven to generate short pulses down to the UV range [184]. If CEP-stability is not necessary, new possibilities are offered by the use of the leftover 800 nm at the TOPAS output or the 1.3 μm signal of the OPA process, for which prior pulse compression would be needed.

For time-resolved spectroscopy of condensed matter, the possibility to control the temperature of the crystal allows another dimension to the set of parameters available to investigate the material. Moreover, many materials undergo phase transitions for certain temperature conditions, which are known to change both the electronic and structural properties of the material. For this reason, the implementation of a cooling stage for the experimental target by installing a cryostat would bring access to new fascinating physical processes. The potential of XAFS spectroscopy to interrogate both the electron and the lattice system, combined with the possibility of controlling temperature, constitutes the perfect tool to study strongly-correlated materials, where the EPC drives mechanisms like superconductivity, charge- and spin-density waves or insulator-to-metal transitions.

The ultra-broadband spectrum of the attosecond SXR pulses offers the possibility to simultaneously probe more than one absorption edge. Performing XANES spectroscopy of several edges at the same time allows monitoring changes in the electronic structure of different elements composing the material. Phenomena like ultrafast charge transfer, polaron formation or exciton dynamics could be followed in real-time by transient XANES spectroscopy at different edges and have a direct impact on several research fields, like energy harvesting for example. Finally, the sub-fs resolution makes attosecond XAFS technique the perfect tool to study the control of carrier motion on the timescales of the optical cycle of the pump laser field, usually referred to as petahertz-speed electronics. Creating and controlling photocurrents at this regime would in principle allow increasing the maximum speed at which optoelectronics devices can be used, at the moment limited to the terahertz regime. The work performed by our group on ultrafast carrier motion in a transition-metal dichalcogenide (TiS_2, [83]) is one of the first investigations of this ultrafast carrier control in solids.

Appendix A

Appendix

A.1 Pump pulse parameters

Here, three tables are reported with the estimation of the main pump pulse parameters for the cases of 1.85 μm pump pulse with thick and thin sample and for the case of 0.8 μm for the case of thick sample only. Values in vacuum refer to estimation at the front surface of the graphite film, while the values in graphite consider the Fresnel losses on the first surface.

Pulse parameter	**1.85 μm High**	**1.85 μm Medium**	**1.85 μm Low**
Fluence vacuum	$204\,\mathrm{mJ/cm^2}$	$57\,\mathrm{mJ/cm^2}$	$8\,\mathrm{mJ/cm^2}$
Intensity vacuum	$1.4 \cdot 10^{13}\,\mathrm{W/cm^2}$	$3.9 \cdot 10^{12}\,\mathrm{W/cm^2}$	$5.5 \cdot 10^{11}\,\mathrm{W/cm^2}$
Field amplitude vacuum	$1.03\,\mathrm{V/Å}$	$0.54\,\mathrm{V/Å}$	$0.20\,\mathrm{V/Å}$
Fluence graphite	$81.4\,\mathrm{mJ/cm^2}$	$22.7\,\mathrm{mJ/cm^2}$	$3.2\,\mathrm{mJ/cm^2}$
Intensity graphite	$5.6 \cdot 10^{12}\,\mathrm{W/cm^2}$	$1.6 \cdot 10^{12}\,\mathrm{W/cm^2}$	$2.2 \cdot 10^{11}\,\mathrm{W/cm^2}$
Field amplitude graphite	$0.33\,\mathrm{V/Å}$	$0.17\,\mathrm{V/Å}$	$0.07\,\mathrm{V/Å}$
Ponderomotive energy	$10.8\,\mathrm{eV}$	$3.0\,\mathrm{eV}$	$0.4\,\mathrm{eV}$
Keldysh parameter	0.03	0.06	0.15

Table A.1: Pulse parameters for the $1.85\,\mu$m pump used for the experiments on 95 nm thick graphite.

Pulse parameter	**0.8μ,m Medium**	**0.8μ,m Low**
Fluence vacuum	$5.3\,\mathrm{mJ/cm^2}$	$1.2\,\mathrm{mJ/cm^2}$
Intensity vacuum	$3.5 \cdot 10^{11}\,\mathrm{W/cm^2}$	$7.7 \cdot 10^{10}\,\mathrm{W/cm^2}$
Field amplitude vacuum	$0.16\ V/Å$	$0.07\ V/Å$
Fluence graphite	$2.8\,\mathrm{mJ/cm^2}$	$0.6\,\mathrm{mJ/cm^2}$
Intensity graphite	$1.9 \cdot 10^{11}\,\mathrm{W/cm^2}$	$4.1 \cdot 10^{10}\,\mathrm{W/cm^2}$
Field amplitude graphite	$0.07\,\mathrm{V/Å}$	$0.03\,\mathrm{V/Å}$
Ponderomotive energy	$0.08\,\mathrm{eV}$	$0.02\,\mathrm{eV}$
Keldysh parameter	0.36	0.76

Table A.2: Pulse parameters for the $0.8\,\mu$m pump used for the experiments on 95 nm thick graphite.

Pulse parameter	$1.85\,\mu$**m High**	$1.85\,\mu$**m Medium**
Fluence vacuum	$150\,\mathrm{mJ/cm^2}$	$42\,\mathrm{mJ/cm^2}$
Intensity vacuum	$1.0 \cdot 10^{13}\,\mathrm{W/cm^2}$	$2.9 \cdot 10^{12}\,\mathrm{W/cm^2}$
Field amplitude vacuum	$0.88\,\mathrm{V/Å}$	$0.47\,\mathrm{V/Å}$
Fluence graphite	$60\,\mathrm{mJ/cm^2}$	$16.8\,\mathrm{mJ/cm^2}$
Intensity graphite	$4.1 \cdot 10^{12}\,\mathrm{W/cm^2}$	$1.2 \cdot 10^{12}\,\mathrm{W/cm^2}$
Field amplitude graphite	$0.28\,\mathrm{V/Å}$	$0.15\,\mathrm{V/Å}$
Ponderomotive energy	$8.0\,\mathrm{eV}$	$2.2\,\mathrm{eV}$
Keldysh parameter	0.035	0.07

Table A.3: Pulse parameters for the $1.85\,\mu$m pump used for the experiments on $20\,$nm thick graphite.

A.2 Time-resolved XAFS

$95\,$nm sample, $1.85\,\mu$m, medium-fluence pump pulse

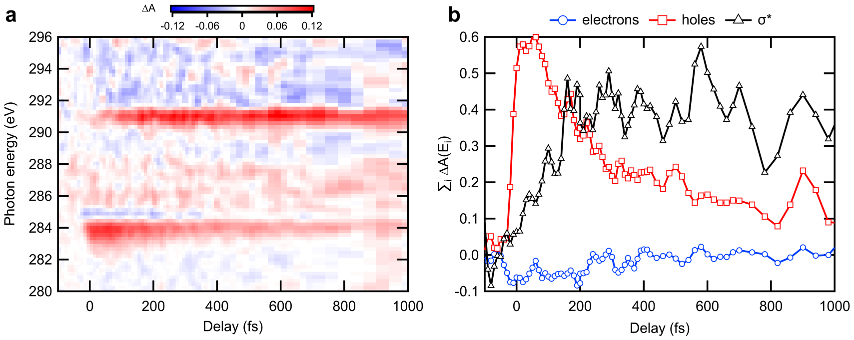

Figure A.1: Differential absorption measurement in $95\,$nm graphite for $1.85\,\mu$m, $57\,\mathrm{mJ/cm^2}$ pump pulse over $1\,$ps time delay range. Time delay step size is: $10\,$fs in $-100 : 420\,$fs range, $20\,$fs in $420 : 700\,$fs range, $30\,$fs in $700 : 1000\,$fs range.

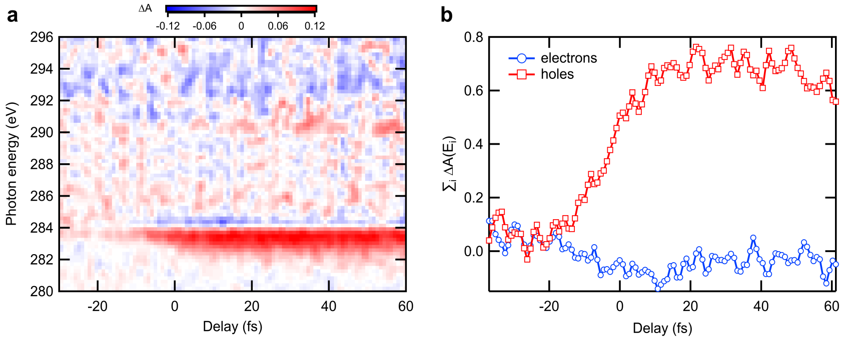

Figure A.2: Sub-fs-resolved differential absorption measurement in 95 nm graphite for 1.85 μm, 57 mJ/cm^2 pump pulse over 1 ps time delay range. Time delay step size is 0.9 fs for the whole time delay range.

95 nm sample, 0.8 μm, medium-fluence pump pulse

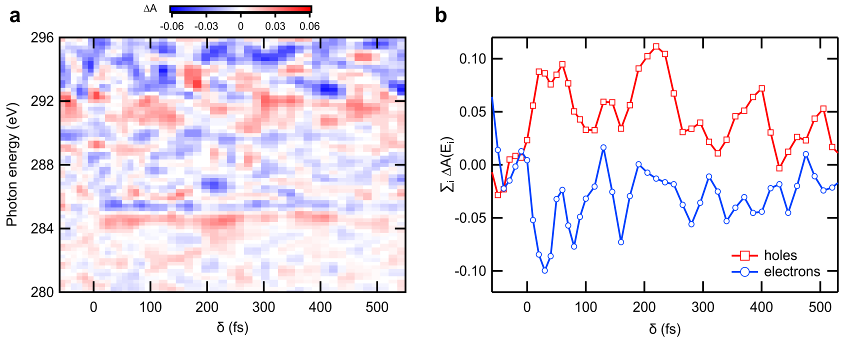

Figure A.3: Differential absorption measurement in 95 nm graphite for 0.8 μm, 5.3 mJ/cm^2 pump pulse over 1 ps time delay range. Time delay step size is: 10 fs in $-60 : 100$ fs range, 15 fs in $100 : 550$ fs range.

95 nm sample, 0.8 μm, low-fluence pump pulse

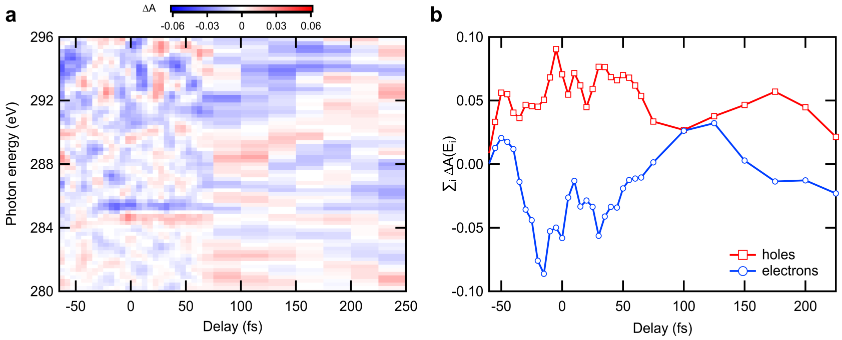

Figure A.4: Differential absorption measurement in 95 nm graphite for 0.8 μm, 1.2 mJ/cm^2 pump pulse over 1 ps time delay range. Time delay step size is: 5 fs in $-65 : 75$ fs range, 25 fs in $75 : 250$ fs range.

20 nm sample, 1.85 μm, high-fluence pump pulse

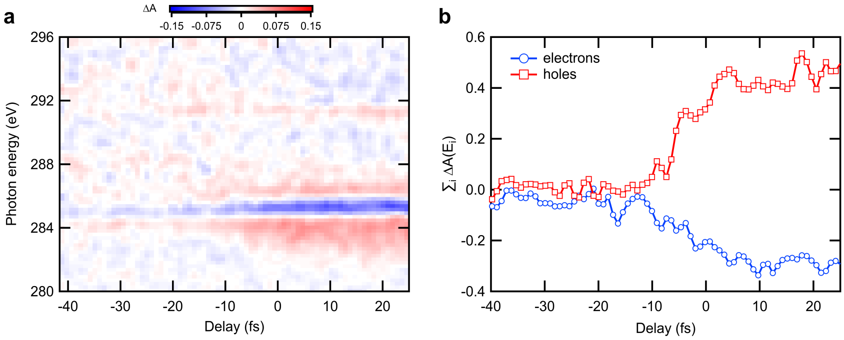

Figure A.5: Sub-fs-resolved differential absorption measurement in 20 nm graphite for 1.85 μm, 150 mJ/cm^2 pump pulse over 1 ps time delay range. Time delay step size is 0.9 fs for the whole time delay range.

20 nm sample, 1.85 μm, high-fluence pump pulse, picosecond scan

The energy axis of the ΔA plot is now increased up to 400 eV to monitor changes in the EXAFS region. Beside a strong signal at 0 ps present around $285-293$ eV and lasting several ps, most likely due to residual carrier population, the ΔA spectrum presents an alternation of positive and negative signals in the $300-400$ eV region appearing after 5 ps and reaching a maximum value towards the end of the scan.

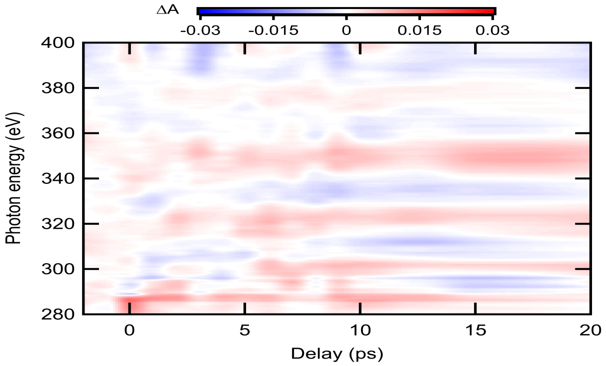

Figure A.6: Ps-resolved differential absorption measurement in 20,nm graphite for 1.85 μm, 150 mJ/cm^2 pump pulse. Time delay step size is 1 ps for the whole time delay range. Data is smoothed on the horizontal axis because of the small number of delay values evaluated.

20 nm sample, 1.85 μm, medium-fluence pump pulse

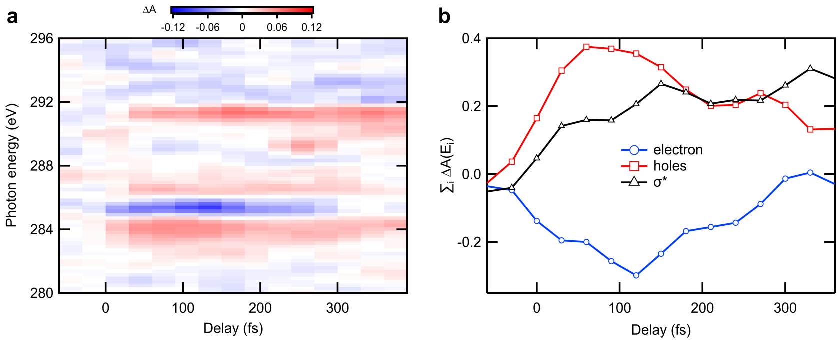

Figure A.7: Sub-fs-resolved differential absorption measurement in 20 nm graphite for 1.85 μm, 42 mJ/cm^2 pump pulse over 1 ps time delay range. Time delay step size is 30 fs in $-60 : 390$ fs range.

A.3 Extraction of decay rate from ΔA data

An example of exponential decay fit to differential absorption data as function of time delay is reported here. From the delay position corresponding to the maximum ΔA value, a single exponential decay is fitted to the experimental data. The resulting decay constant, together with the numerical uncertainty, is reversed to obtain the scattering rate, evaluated for the analysis reported in 4.2.3.

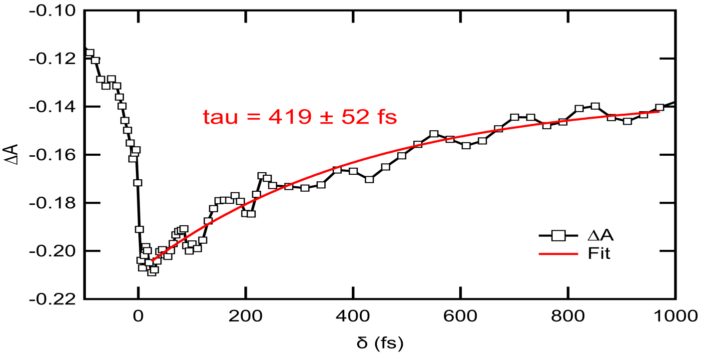

Figure A.8: Exponential decay fit to measured differential absorption data. The inverse of the obtained decay constant, the decay rate, is then used for the analysis of 4.2.3.

Bibliography

[1] A. Zewail, "*Femtochemistry: Atomic-scale Dynamics of the Chemical Bond*," *Journal of Physical Chemistry A*, vol. **104**, no. 24, pp. 5660–5694, (2000).

[2] M. T. Hassan, T. T. Luu, A. Moulet, O. Raskazovskaya, P. Zhokhov, M. Garg, N. Karpowicz, A. M. Zheltikov, V. Pervak, F. Krausz, and E. Goulielmakis, "*Optical attosecond pulses and tracking the nonlinear response of bound electrons*," *Nature*, vol. **530**, pp. 66–70, (2016).

[3] D. Strickland and G. Mourou, "*Compression of amplified chirped optical pulses*," *Optics Communications*, vol. **56**, no. 3, pp. 219–221, (1985).

[4] A. McPherson, G. Gibson, H. Jara, U. Johann, T. S. Luk, I. A. McIntyre, K. Boyer, and C. K. Rhodes, "*Studies of multiphoton production of vacuum-ultraviolet radiation in the rare gases*," *Journal of the Optical Society of America B*, vol. **4**, no. 4, pp. 595–601, (1987).

[5] M. Ferray, A. L'Huillier, X. F. Li, L. A. Lompre, G. Mainfray, and C. Manus, "*Multiple-harmonic conversion of 1064 nm radiation in rare gases*," *Journal of Physics B*, vol. **21**, no. 3, (1988).

[6] P. M. Paul, E. S. Toma, P. Breger, G. Mullot, F. Augé, P. Balcou, H. G. Muller, and P. Agostini, "*Observation of a Train of Attosecond Pulses from High Harmonic Generation*," *Science*, vol. **292**, no. 5522, pp. 1689–1692, (2001).

[7] M. Hentschel, R. Kienberger, C. Spielmann, G. A. Reider, N. Milosevic, T. Brabec, P. Corkum, U. Heinzmann, M. Drescher, and F. Krausz, "*Attosecond Metrology*," *Nature*, vol. **414**, p. 509–513, (2001).

[8] P. Corkum and F. Krausz, "*Attosecond Science*," *Nature Physics*, vol. **3**, pp. 381–387, (2007).

[9] F. Krausz and M. Ivanov, "*Attosecond Physics*," *Review of Modern Physics*, vol. **81**, pp. 163–234, (2009).

[10] M. F. Kling and M. J. J. Vrakking, "*Attosecond Electron Dynamics*," *Annual Review of Physical Chemistry*, vol. **59**, p. 463–492, (2008).

[11] F. Calegari, G. Sansone, S. Stagira, C. Vozzi, and M. Nisoli, "*Advances in attosecond science*," *Journal of Physics B: Atomic, Molecular, Optical Physics*, vol. **49**, no. 062001, (2016).

[12] S. R. Leone and D. M. Neumark, "*Attosecond science in atomic, molecular, and condensed matter physics*," *Faraday Discussions*, vol. **194**, no. 15, (2016).

[13] J. L. Krause, K. J. Schafer, and K. G. Kulander, "*High-order harmonic generation from atoms and ions in the high intensity regime*," *Physical Review Letters*, vol. **68**, no. 3535, (1992).

[14] P. B. Corkum, "*Plasma perspective on strong field multiphoton ionization*," *Physical Review Letters*, vol. **71**, no. 1994, (1993).

[15] M. Nisoli, P. Decleva, F. Calegari, A. Palacios, and F. Martín, "*Attosecond Electron Dynamics in Molecules*," *Chemical Reviews*, vol. **117**, no. 16, pp. 10760–10825, (2017).

[16] M. Lewenstein, P. Balcou, M. Y. Ivanov, A. L'Huillier, and P. B. Corkum, "*Theory of high-harmonic generation by low-frequency laser fields*," *Physical Review A*, vol. **49**, no. 2117, (1994).

[17] P. Balcou and A. L'Huillier, "*Phase-matching effects in strong-field harmonic generation*," *Physical Review A*, vol. **47**, p. 1447–1459, (1993).

[18] P. Balcou, P. Salieres, A. L'Huillier, and M. Lewenstein, "*Generalized phase-matching conditions for high harmonics: the role of field-gradient forces*," *Physical Review A*, vol. **55**, p. 3204–3210, (1997).

[19] B. Shan and Z. Chang, "*Dramatic extension of the high-order harmonic cutoff by using a long-wavelength driving field*," *Physical Review A*, vol. **65**, no. 011804(R), (2001).

[20] E. J. Takahashi, T. Kanai, K. L. Ishikawa, and K. Nabekawa, Y. andand Midorikawa, "*Coherent Water Window X Ray by Phase-Matched High-Order Harmonic Generation in Neutral Media*," *Physical Review Letters*, vol. **101**, no. 253901, (2008).

[21] A. D. Shiner, C. Trallero-Herrero, N. Kajumba, H. C. Bandulet, D. Comtois, F. Légaré, M. Giguère, J.-C. Kieffer, P. B. Corkum, and D. M. Villeneuve, "*Wavelength Scaling of High Harmonic Generation Efficiency*," *Physical Review Letters*, vol. **103**, no. 073902, (2009).

[22] D. R. Austin and J. Biegert, "*Strong-field approximation for the wavelength scaling of high-harmonic generation*," *Physical Review A*, vol. **86**, no. 023813, (2012).

[23] P. Colosimo, G. Doumy, C. I. Blaga, J. Wheeler, C. Hauri, F. Catoire, J. Tate, R. Chirla, A. M. March, G. G. Paulus, H. G. Muller, P. Agostini, and L. F. DiMauro, "*Scaling strong-field interactions towards the classical limit*," *Nature Physics*, vol. **4**, pp. 386–389, (2008).

[24] G. Doumy, J. Wheeler, C. Roedig, R. Chirla, P. Agostini, and L. F. DiMauro, "*Attosecond Synchronization of High-Order Harmonics from Mid-infrared Drivers*," *Physical Review Letters*, vol. **102**, no. 093002, (2009).

[25] S. L. Cousin, F. Silva, S. M. Teichmann, M. Hemmer, B. Buades, and J. Biegert, "*High-flux table-top soft x-ray source driven by sub-2-cycle, CEP stable, 1.85-μm 1-kHz pulses for carbon K edge spectroscopy*," *Optics Letters*, vol. **39**, no. 18, (2014).

[26] F. Silva, S. M. Teichmann, S. L. Cousin, M. Hemmer, and J. Biegert, "*Spatio-temporal isolation of attosecond soft X-ray pulses in the water window*," *Nature Communications*, vol. **6**, no. 661, (2015).

[27] S. M. Teichmann, F. Silva, S. L. Cousin, M. Hemmer, and J. Biegert, "*0.5 keV soft X-ray attosecond continua*," *Nature Communications*, vol. **7**, no. 11493, (2016).

[28] J. Li, X. Ren, Y. Yin, K. Zhao, A. Chew, Y. Cheng, E. Cunningham, Y. Wang, S. Hu, Y. Wu, M. Chini, and Z. Chang, "*53-attosecond X-ray pulses reach the carbon K-edge*," *Physical Review A*, vol. **8**, no. 186, (2017).

[29] A. Attar, A. R. Bhattacherjee, C. D. Pemmaraju, K. Schnorr, K. D. Closser, D. Prendergast, and S. R. Leone, "*Femtosecond x-ray spectroscopy*

of an electrocyclic ring-opening reaction," *Science*, vol. **356**, no. 6333, pp. 54–59, (2017).

[30] C. Schmidt, Y. Pertot, T. Balciunas, K. Zinchenko, M. Matthews, H. J. Wörner, and J.-P. Wolf, "*High-order harmonic source spanning up to the oxygen K-edge based on filamentation pulse compression*," *Optics Express*, vol. **26**, no. 9, pp. 11834–11842, (2018).

[31] A. S. Johnson, D. R. Austin, D. A. Wood, C. Brahms, A. Gregory, K. B. Holzner, S. Jarosch, E. W. Larsen, S. Parker, C. S. Strüber, P. Ye, J. W. G. Tisch, and J. P. Marangos, "*High-flux soft x-ray harmonic generation from ionization-shaped few-cycle laser pulses*," *Science Advances*, vol. **336**, no. 6086, pp. 1287–1291, (2018).

[32] T. Popmintchev, M.-C. Chen, D. Popmintchev, P. Arpin, S. Brown, S. Ališauskas, G. Andriukaitis, T. Balčiunas, O. D. Mücke, A. Pugzlys, A. Baltuška, B. Shim, S. E. Schrauth, A. Gaeta, C. Hernández-García, L. Plaja, A. Becker, A. Jaron-Becker, M. M. Murnane, and H. C. Kapteyn, "*Bright Coherent Ultrahigh Harmonics in the keV X-ray Regime from Mid-Infrared Femtosecond Lasers*," *Science*, vol. **336**, no. 6086, pp. 1287–1291, (2012).

[33] P. Johnsson, J. Mauritsson, T. Remetter, A. L'Huillier, and K. J. Schafer, "*Attosecond Control of Ionization by Wave-Packet Interference*," *Physical Review Letters*, vol. **99**, no. 233001, (2007).

[34] M. Holler, F. Schapper, L. Gallmann, and U. Keller, "*Attosecond Electron Wave-Packet Interference Observed by Transient Absorption*," *Physical Review Letters*, vol. **106**, no. 123601, (2011).

[35] R. Kienberger, E. Goulielmakis, M. Uiberacker, A. Baltuska, V. Yakovlev, F. Bammer, A. Scrinzi, T. Westerwalbesloh, U. Kleineberg, U. Heinzmann, M. Drescher, and F. Krausz, "*Atomic transient recorder*," *Nature*, vol. **427**, p. 817–821, (2004).

[36] O. Tcherbakoff, E. Mével, D. Descamps, J. Plumridge, and E. Constant, "*Time-gated high-order harmonic generation*," *Physical Review A*, vol. **68**, no. 043804, (2003).

[37] I. J. Sola, E. Mével, L. Elouga, E. Constant, V. Strelkov, L. Poletto, P. Villoresi, E. Benedetti, J.-P. Caumes, S. Stagira, C. Vozzi, G. Sansone, and M. Nisoli, "*Controlling attosecond electron dynamics by phase-stabilized polarization gating*," *Nature Physics*, vol. **2**, p. 319–322, (2006).

[38] G. Sansone, E. Benedetti, F. Calegari, C. Vozzi, L. Avaldi, R. Flammini, L. Poletto, P. Villoresi, C. Altucci, R. Velotta, S. Stagira, S. De Silvestri, and M. Nisoli, "*Isolated Single-Cycle Attosecond Pulses*," *Science*, vol. **314**, no. 5798, pp. 443–446, (2006).

[39] H. Mashiko, S. Gilbertson, M. Chini, X. Feng, C. Yun, H. Wang, S. D. Khan, S. Chen, and Z. Chang, "*Extreme ultraviolet supercontinua supporting pulse durations of less than one atomic unit of time*," *Optics Letters*, vol. **34**, no. 21, pp. 3337–3339, (2009).

[40] T. Pfeifer, A. Jullien, M. J. Abel, P. M. Nagel, L. Gallmann, D. M. Neumark, and S. R. Leone, "*Generating coherent broadband continuum soft-x-ray radiation by attosecond ionization gating*," *Optics Express*, vol. **15**, no. 25, pp. 17120–17128, (2007).

[41] F. Ferrari, F. Calegari, M. Lucchini, C. Vozzi, S. Stagira, G. Sansone, and M. Nisoli, "*High-energy isolated attosecond pulses generated by above-saturation few-cycle fields*," *Nature Photonics*, vol. **4**, pp. 875–879, (2010).

[42] H. Vincenti and F. Quéré, "*Attosecond Lighthouses: How To Use Spatiotemporally Coupled Light Fields To Generate Isolated Attosecond Pulses*," *Physical Review Letters*, vol. **108**, no. 113904, (2012).

[43] K. T. Kim, C. Zhang, T. Ruchon, J.-F. Hergott, T. Auguste, D. M. Villeneuve, P. B. Corkum, and F. Quéré, "*Photonic streaking of attosecond pulse trains*," *Nature Photonics*, vol. **7**, p. 651–656, (2013).

[44] H. Merdji, T. Auguste, W. Boutu, J. P. Caumes, B. Carré, T. Pfeifer, A. Jullien, D. M. Neumark, and S. R. Leone, "*Isolated attosecond pulses using a detuned second-harmonic field*," *Optics Letters*, vol. **32**, no. 21, pp. 3134–3136, (2007).

[45] C. Vozzi, F. Calegari, F. Frassetto, L. Poletto, G. Sansone, P. Villoresi, M. Nisoli, S. De Silvestri, and S. Stagira, "*Coherent continuum generation above 100 eV driven by an ir parametric source in a two-color scheme*," *Physical Review A*, vol. **79**, p. 033842, (2009).

[46] E. J. Takahashi, P. Lan, O. D. Mücke, Y. Nabekawa, and K. Midorikawa, "*Infrared Two-Color Multicycle Laser Field Synthesis for Generating an Intense Attosecond Pulse*," *Physical Review Letters*, vol. **104**, no. 233901, (2010).

[47] J. Itatani, F. Quéré, G. L. Yudin, M. Y. Ivanov, F. Krausz, and P. B. Corkum, "*Attosecond Streak Camera*," *Physical Review Letters*, vol. **88**, no. 173903, (2002).

[48] Y. Mairesse and F. Quéré, "*Frequency-resolved optical gating for complete reconstruction of attosecond bursts*," *Optics Express*, vol. **71**, pp. 1–4, (2005).

[49] E. Goulielmakis, M. Uiberacker, R. Kienberger, A. Baltuska, V. Yakovlev, A. Scrinzi, T. Westerwalbesloh, U. Kleineberg, U. Heinzmann, M. Drescher, and F. Krausz, "*Direct Measurement of Light Waves*," *Science*, vol. **305**, no. 5688, pp. 1267–1269, (2004).

[50] M. Lucchini, M. H. Brügmann, A. Ludwig, L. Gallmann, U. Keller, and T. Feurer, "*Ptychographic reconstruction of attosecond pulses*," *Optics Express*, vol. **23**, no. 23, pp. 29502–29513, (2015).

[51] M. Chini, S. Gilbertson, S. D. Khan, and Z. Chang, "*Characterizing ultrabroadband attosecond lasers*," *Optics Express*, vol. **18**, no. 12, pp. 13006–13016, (2010).

[52] S. L. Cousin, N. Di Palo, B. Buades, S. M. Teichmann, M. Reduzzi, M. Devetta, A. Kheifets, G. Sansone, and J. Biegert, "*Attosecond Streaking in the Water Window: A New Regime of Attosecond Pulse Characterization*," *Physical Review X*, vol. **7**, no. 041030, (2017).

[53] T. Gaumnitz, A. Jain, Y. Pertot, M. Huppert, I. Jordan, F. A. Lamas, and H. J. Wörner, "*Streaking of 43-attosecond soft-X-ray pulses generated by a passively CEP-stable mid-infrared driver*," *Optics Express*, vol. **25**, pp. 27506–27518, (2017).

[54] P. Tzallas, E. Skantzakis, L. A. A. Nikolopoulos, G. D. Tsakiris, and D. Charalambidis, "*Extreme-ultraviolet pump–probe studies of one-femtosecond-scale electron dynamics*," *Nature Physics*, vol. **7**, p. 781–784, (2011).

[55] M. Drescher, M. Hentschel, R. Kienberger, M. Uiberacker, V. Yakovlev, A. Scrinzi, T. Westerwalbesloh, U. Kleineberg, U. Heinzmann, and F. Krausz, "*Time-resolved atomic inner-shell spectroscopy*," *Nature*, vol. **419**, p. 803–807, (2002).

[56] M. Uiberacker, T. Uphues, M. Schultze, A. J. Verhoef, V. Yakovlev, M. F. Kling, J. Rauschenberger, N. M. Kabachnik, H. Schröder, M. Lezius, K. L. Kompa, H. G. Muller, M. J. J. Vrakking, S. Hendel, U. Kleineberg, U. Heinzmann, M. Drescher, and F. Krausz, "*Attosecond real-time observation of electron tunnelling in atoms*," *Nature*, vol. **446**, pp. 627–632, (2007).

[57] G. Sansone, F. Kelkensberg, J. F. Pérez-Torres, F. Morales, M. F. Kling, W. Siu, O. Ghafur, P. Johnsson, M. Swoboda, E. Benedetti, F. Ferrari, F. Lépine, J. L. Sanz-Vicario, S. Zherebtsov, I. Znakovskaya, A. L'Huillier, M. Y. Ivanov, M. Nisoli, F. Martín, and M. J. J. Vrakking, "*Electron localization following attosecond molecular photoionization*," *Nature*, vol. **465**, pp. 763–766, (2010).

[58] F. Calegari, D. Ayuso, A. Trabattoni, L. Belshaw, S. De Camillis, S. Anumula, F. Frassetto, L. Poletto, A. Palacios, P. Decleva, J. B. Greenwood, F. Martín, and M. Nisoli, "*Ultrafast electron dynamics in phenylalanine initiated by attosecond pulses*," *Science*, vol. **346**, no. 6207, pp. 336–339, (2014).

[59] M. Schultze, M. Fieß, N. Karpowicz, J. Gagnon, M. Korbman, M. Hofstetter, S. Neppl, A. L. Cavalieri, Y. Komninos, T. Mercouris, C. A. Nicolaides, R. Pazourek, S. Nagele, J. Feist, J. Burgdörfer, A. M. Azzeer, R. Ernstorfer, R. Kienberger, U. Kleineberg, E. Goulielmakis, F. Krausz, and V. S. Yakovlev, "*Delay in photoemission*," *Science*, vol. **328**, no. 5986, pp. 1658–1662, (2010).

[60] A. L. Cavalieri, N. Müller, T. Uphues, V. S. Yakovlev, A. Baltuška, B. Horvath, B. Schmidt, L. Blümel, R. Holzwarth, S. Hendel, M. Drescher, U. Kleineberg, P. M. Echenique, R. Kienberger, F. Krausz, and U. U. Heinzmann, "*Attosecond spectroscopy in condensed matter*," *Nature*, vol. **449**, p. 1029–1032, (2007).

[61] S. Neppl, R. Ernstorfer, A. L. Cavalieri, C. Lemell, G. Wachter, E. Magerl, E. M. Bothschafter, M. Jobst, M. Hofstetter, U. Kleineberg, J. V. Barth, D. Menzel, J. Burgdörfer, P. Feulner, F. Krausz, and R. Kienberger, "*Direct observation of electron propagation and dielectric screening on the atomic length scale*," *Nature*, vol. **517**, p. 342–346, (2015).

[62] K. Klünder, J. M. Dahlström, M. Gisselbrecht, T. Fordell, M. Swoboda, D. Guénot, P. Johnsson, J. Caillat, J. Mauritsson, A. Maquet, R. Taïeb,

and A. L'Huillier, "*Probing Single-Photon Ionization on the Attosecond Time Scale*," *Physical Review Letters*, vol. **106**, no. 143002, (2011).

[63] M. Sabbar, S. Heuser, R. Boge, M. Lucchini, T. Carette, E. Lindroth, L. Gallmann, C. Cirelli, and U. Keller, "*Resonance Effects in Photoemission Time Delays*," *Nature*, vol. **115**, no. 133001, (2015).

[64] R. Locher, L. Castiglioni, M. Lucchini, M. Greif, L. Gallmann, J. Osterwalder, M. Hengsberger, and U. Keller, "*Energy-dependent photoemission delays from noble metal surfaces by attosecond interferometry*," *Optica*, vol. **2**, no. 5, pp. 405–410, (2015).

[65] J. Itatani, J. Levesque, D. Zeidler, H. Niikura, H. Pépin, J. C. Kieffer, P. B. Corkum, and D. M. Villeneuve, "*Tomographic reconstruction of molecular orbitals*," *Nature*, vol. **432**, p. 867–871, (2004).

[66] O. Smirnova, Y. Mairesse, S. Patchkovskii, N. Dudovich, D. Villeneuve, P. B. Corkum, and M. Y. Ivanov, "*High harmonic interferometry of multi-electron dynamics in molecules*," *Nature*, vol. **460**, p. 972–977, (2009).

[67] P. M. Kraus, B. Mignolet, D. Baykusheva, A. Rupenyan, L. Horný, E. F. Penka, G. Grassi, O. I. Tolstikhin, J. Schneider, F. Jensen, L. B. Madsen, A. D. Bandrauk, F. Remacle, and H. J. Wörner, "*Measurement and laser control of attosecond charge migration in ionized iodoacetylene*," *Science*, vol. **350**, no. 6262, pp. 790–795, (2015).

[68] S. Ghimire, A. D. DiChiara, E. Sistrunk, P. Agostini, L. F. DiMauro, and D. A. Reis, "*Observation of high-order harmonic generation in a bulk crystal*," *Nature Physics*, vol. **7**, pp. 138–141, (2011).

[69] S. Ghimire and D. A. Reis, "*High harmonic generation from solids*," *Nature Physics*, vol. **15**, pp. 10–16, (2019).

[70] R. Geneaux, H. J. B. Marroux, A. Guggenmos, D. M. Neumark, and S. R. Leone, "*Transient absorption spectroscopy using high harmonic generation: a review of ultrafast X-ray dynamics in molecules and solids*," *Philosophical Transactions of the Royal Society A*, vol. **377**, no. 20170463, (2019).

[71] S. Y. Kruchinin, F. Krausz, and V. S. Yakovlev, "*Colloquium: Strong-field phenomena in periodic systems*," *Review of Modern Physics*, vol. **90**, no. 20170463, (2018).

[72] M. Schultze, E. M. Bothschafter, A. Sommer, S. Holzner, W. Schweinberger, M. Fiess, M. Hofstetter, R. Kienberger, V. Apalkov, V. S. Yakovlev, M. I. Stockman, and F. Krausz, "*Controlling dielectrics with the electric field of light*," *Nature*, vol. **493**, pp. 75–78, (2013).

[73] M. Schultze, K. K. Ramasesha, C. D. Pemmaraju, S. A. Sato, D. Whitmore, A. Gandman, J. S. Prell, L. J. Borja, D. Prendergast, K. Yabana, D. M. Neumark, and S. R. Leone, "*Attosecond band-gap dynamics in silicon*," *Science*, vol. **346**, no. 6215, pp. 1348–1352, (2014).

[74] H. Mashiko, K. Oguri, T. Yamaguchi, A. Suda, and H. Gotoh, "*Petahertz optical drive with wide-bandgap semiconductor*," *MRS Bulletin*, vol. **12**, pp. 741–745, (2016).

[75] F. Schlaepfer, M. Lucchini, S. A. Sato, M. Volkov, M. Kasmi, N. Hartmann, A. Rubio, L. Gallman, and U. Keller, "*Attosecond optical-field-enhanced carrier injection into the GaAs conduction band*," *Nature physics*, vol. **14**, pp. 560–564, (2018).

[76] M. Lucchini, S. A. Sato, A. Ludwig, J. Herrmann, M. Volkov, L. Kasmi, Y. Shinohara, K. Yabana, L. Gallmann, and U. Keller, "*Attosecond dynamical Franz-Keldysh effect in polycrystalline diamond*," *Science*, vol. **353**, no. 6302, pp. 916–919, (2016).

[77] M. Zürch, H.-T. Chang, L. J. Borja, P. M. Kraus, S. Cushing, A. Gandman, C. J. Kaplan, M. H. Oh, J. S. Prell, D. Prendergast, C. D. Pemmaraju, D. M. Neumark, and S. R. Leone, "*Direct and simultaneous observation of ultrafast electron and hole dynamics in germanium*," *Nature communications*, vol. **8**, no. 15734, (2017).

[78] E. Papalazarou, D. Boschetto, J. Gautier, T. Garl, C. Valentin, G. Rey, P. Zeitoun, A. Rousse, P. Balcou, and M. Marsi, "*Probing coherently excited optical phonons by extreme ultraviolet radiation with femtosecond time resolution*," *Applied Physics Letters*, vol. **93**, no. 041114, (2008).

[79] J. Weisshaupt, A. Rouzée, M. Woerner, M. J. J. Vrakking, T. Elsaesser, E. L. Shirley, and A. Borgschulte, "*Ultrafast modulation of electronic structure by coherent phonon excitations*," *Physical Review B*, vol. **95**, no. 081101(R), (2017).

[80] L. M. Carneiro, S. K. Cushing, C. Liu, Y. Su, P. Yang, A. P. Alivisatos, and S. R. Leone, "*Excitation-wavelength-dependent small polaron trapping of photoexcited carriers in α-$Fe_2 0_3$*," *Applied Physics Letters*, vol. **16**, p. 819–825, (2017).

[81] M. F. Jager, C. Ott, P. M. Kraus, C. J. Kaplan, W. Pouse, R. E. Marvel, R. F. Haglund, D. M. Neumark, and S. R. Leone, "*Tracking the insulator-to-metal phase transition in VO_2 with few-femtosecond extreme UV transient absorption spectroscopy*," *Proceedings of the National Academy of Science*, vol. **5**, no. 114, pp. 9558–9563, (2017).

[82] Y. Pertot, C. Schmidt, M. Matthews, A. Chauvet, M. Huppert, V. Svoboda, A. von Conta, A. Tehlar, D. Baykusheva, J.-P. Wolf, and H. J. Wörner, "*Time-resolved x-ray absorption spectroscopy with a water window high-harmonic source*," *Science*, vol. **355**, no. 6322, pp. 264–267, (2017).

[83] B. Buades, A. Picón, I. León, N. Di Palo, S. L. Cousin, C. Cocchi, E. Pellegrin, J. Herrero Martin, S. Mañas-Valero, E. Coronado, T. Danz, C. Draxl, M. Uemoto, K. Yabana, M. Schultze, S. Wall, and J. Biegert, "*Attosecond-resolved petahertz carrier motion in semi-metallic TiS_2*," *arXiv:1808.06493*, (2018).

[84] D. D. L. Chung, "*Review graphite*," *Journal of Materials Science*, vol. **37**, p. 1475 – 1489, (2002).

[85] J.-C. Charlier, X. Gonze, and J.-P. Michenaud, "*Graphite Interplanar Bonding: Electronic Delocalization and van der Waals Interaction*," *Europhysics letters*, vol. **28**, no. 6, (1994).

[86] P. R. Wallace, "*The band theory of graphite*," *Physical Review*, vol. **71**, p. 622–634, (1947).

[87] J. W. McClure, "*Energy Band Structure of Graphite*," *IBM Journal of Research and Development*, vol. **8**, no. 3, (1964).

[88] D. E. Soule, "*Change in Fermi Surfaces of Graphite by Dilute Acceptor Doping*," *IBM Journal of Research and Development*, vol. **8**, no. 3, (1964).

[89] M. Müller, M. Bräuninger, and B. Trauzettel, "*Temperature Dependence of the Conductivity of Ballistic Graphene*," *Physical Review Letters*, vol. **103**, no. 196801, (2009).

[90] M. Koch, F. Ample, G. Joachim, and L. Grill, "*Voltage-dependent conductance of a single graphene nanoribbon*," *Nature Nanotechnology*, vol. **7**, pp. 713–717, (2012).

[91] A. K. Geim and K. S. Novoselov, "*The rise of graphene*," *Nature Materials*, vol. **6**, pp. 183–191, (2007).

[92] F. Bonaccorso, Z. Sun, T. Hasan, and A. C. Ferrari, "*Graphene photonics and optoelectronics*," *Nature Photonics*, vol. **4**, pp. 611–622, (2010).

[93] J. Yin, S. Slizovskiy, Y. Cao, S. Hu, Y. Yang, I. Lobanova, B. A. Piot, S.-K. Son, S. Ozdemir, T. Taniguchi, K. Watanabe, K. S. Novoselov, F. Guinea, A. K. Geim, V. Fal'ko, and A. Mishchenko, "*Dimensional reduction, quantum Hall effect and layer parity in graphite films*," *Nature Physics*, vol. **15**, pp. 437–442, (2019).

[94] L. A. Pendrys, C. Zeller, and F. L. Vogel, "*Electrical transport properties of natural and synthetic graphite*," *Journal of Materials Science*, vol. **15**, no. 8, p. 2103–2112, (1980).

[95] E. A. Taft and H. R. Philipp, "*Optical properties of graphite*," *Physical Review*, vol. **138**, no. A197, (1965).

[96] F. H. L. Koppens, T. Mueller, P. Avouris, A. C. Ferrari, M. S. Vitiello, and M. Polini, "*Photodetectors based on graphene, other two-dimensional materials and hybrid systems*," *Nature Nanotechnology*, vol. **9**, (2014).

[97] N. S. Rasor and J. D. McClelland, "*Thermal properties of graphite, molybdenum and tantalum to their destruction temperatures*," *Journal of Physics and Chemistry of Solids*, vol. **15**, no. 1-2, pp. 17–26, (1960).

[98] K. Seibert, G. C. Cho, W. Kütt, H. Kurz, D. H. Reitze, J. I. Dadap, H. Ahn, M. C. Downer, and A. M. Malvezzi, "*Femtosecond carrier dynamics in graphite*," *Physical Review B*, vol. **42**, no. 5, (1990).

[99] C. D. Spataru, M. A. Cazalilla, A. Rubio, P. M. Benedict, L. X. Echenique, and S. G. Louie, "*Anomalous Quasiparticle Lifetime in Graphite: Band Structure Effects*," *Physical Review Letters*, vol. **87**, no. 24, (2001).

[100] G. Moos, C. Gahl, R. Fasel, M. Wolf, and T. Hertel, "*Anisotropy of Quasiparticle Lifetimes and the Role of Disorder in Graphite from Ultrafast Time-Resolved Photoemission Spectroscopy*," *Physical Review Letters*, vol. **87**, no. 26, (2001).

[101] D. Pines and P. Nozieres, *The theory of Quantum Liquids, Normal Fermi Liquids Vol. I.* Addison-Wesley, (1989).

[102] T. Kampfrath, L. Perfetti, F. Schapper, C. Frischkorn, and M. Wolf, "*Strongly Coupled Optical Phonons in the Ultrafast Dynamics of the Electronic Energy and Current Relaxation in Graphite*," *Physical Review Letters*, vol. **95**, no. 187403, (2005).

[103] M. Breusing, C. Ropers, and T. Elsaesser, "*Ultrafast carrier dynamics in graphite*," *Physical Review Letters*, vol. **102**, no. 086809, (2009). doi: `10.1103/PhysRevLett.102.086809`.

[104] G. Rohde, A. Stange, A. Müller, M. Behrendt, L. P. Oloff, K. Hanff, T. J. Albert, P. Hein, K. Rossnagel, and M. Bauer, "*Ultrafast Formation of a Fermi-Dirac Distributed Electron Gas*," *Physical Review Letters*, vol. **121**, no. 256401, (2018). doi: `10.1103/PhysRevLett.121.256401`.

[105] C. Stange, A. C. Sohrt, L. X. Yang, G. G. Rohde, K. Janssen, P. Hein, L. P. Oloff, K. Hanff, K. Rossnagel, and M. Bauer, "*Hot electron cooling in graphite: Supercollision versus hot phonon decay*," *Physical Review B*, vol. **92**, no. 184303, (2015).

[106] T. Winzer, A. Knorr, and E. Malic, "*Carrier multiplication in graphene*," *Nano Letters*, vol. **10**, p. 4839–4843, (2010).

[107] E. Malic, T. Winzer, E. Bobkin, and A. Knorr, "*Microscopic theory of absorption and ultrafast many-particle kinetics in graphene*," *Physical Review B*, vol. **84**, no. 205406, (2011).

[108] T. Winzer and E. Malic, "*Impact of Auger processes on carrier dynamics in graphene*," *Physical Review B*, vol. **85**, no. 241404(R), (2012).

[109] E. Malic, T. Winzer, F. Wendler, and A. Knorr, "*Review on carrier multiplication in graphene*," *Physica Status Solidi B*, vol. **253**, no. 12, (2016).

[110] D. Brida, A. Tomadin, C. Manzoni, Y. J. Kim, A. Lombardo, S. Milana, R. R. Nair, K. S. Novoselov, A. C. Ferrari, G. Cerullo, and M. Polini, "*Ultrafast collinear scattering and carrier multiplication in graphene*," *Nature communications*, vol. **4**, no. 1987, (2013).

[111] I. Gierz, F. Calegari, S. Aeschlimann, M. Chávez Cervantes, C. Cacho, R. T. Chapman, E. Springate, S. Link, U. Starke, C. R. Ast, and A. Cavalleri, "*Tracking Primary Thermalization Events in Graphene with Photoemission at Extreme Time Scales*," *Physical Review Letters*, vol. **115**, no. 086803, (2015). doi: `10.1103/PhysRevLett.115.086803`.

[112] J. Maultzsch, S. Reich, C. Thomsen, H. Requardt, and P. Ordejón, "*Phonon dispersion in graphite*," *Physical Review Letters*, vol. **92**, no. 7, (2004).

[113] M. Mohr, J. Maultzsch, E. Dobardžić, S. Reich, I. Milošević, M. Damnjanović, A. Bosak, M. Krisch, and C. Thomsen, "*Phonon dispersion of graphite by inelastic x-ray scattering*," *Physical Review B*, vol. **76**, no. 035439, (2007).

[114] M. J. Stern, L. P. René de Cotret, M. R. Otto, R. P. Chatelain, M. Boisvert, J-P. Sutton, and B. J. Siwick, "*Mapping momentum-dependent electron-phonon coupling and nonequilibrium phonon dynamics with ultrafast electron diffuse scattering*," *Physical Review B*, vol. **97**, no. 165416, (2018).

[115] S. Reich and C. Thomsen, "*Raman spectroscopy of graphite*," *Phil. Trans. R. Soc. Lond. A*, vol. **362**, p. 2271–2288, (2004).

[116] A. C. Ferrari, "*Raman spectroscopy of graphene and graphite: Disorder, electron–phonon coupling, doping and nonadiabatic effects*," *Solid State Communications*, vol. **143**, no. 1-2, pp. 47–57, (2007).

[117] T. Mishina, K. Nitta, and Y. Masumoto, "*Coherent lattice vibration of interlayer shearing mode of graphite*," *Physical Review B*, vol. **62**, no. 4, (2000).

[118] S. Rhuman, A. G. Joly, and K. A. Nelson, "*Coherent molecular vibrational motion observed in the time domain through impulsive stimulated Raman scattering*," *IEEE Journal of Quantum Electronics*, vol. **24**, no. 2, pp. 460–469, (1988).

[119] H. J. Zeiger, J. Vidal, T. K. Cheng, E. P. Ippen, G. Dresselhaus, and M. S. Dresselhaus, "*Theory for displacive excitation of coherent phonons*," *Physical Review B*, vol. **45**, no. 2, (1992).

[120] G. A. Garrett, T. F. Albrecht, J. F. Whitaker, and R. Merlin, "*Coherent THz Phonons Driven by Light Pulses and the Sb Problem: What is the Mechanism?*," *Physical Review Letters*, vol. **77**, no. 17, (1996).

[121] K. Ishioka, M. Hase, M. Kitajima, L. Wirtz, A. Rubio, and H. Petek, "*Ultrafast electron-phonon decoupling in graphite*," *Physical Review B*, vol. **77**, no. 121402(R), (2008).

[122] H. Yan, D. Song, K. F. Mak, I. Chatzakis, J. Maultzsch, and T. H. Heinz, "*Time-resolved Raman spectroscopy of optical phonons in graphite: Phonon anharmonic coupling and anomalous stiffening*," *Physical Review B*, vol. **80**, no. 121403(R), (2009).

[123] R. M. van der Veen, T. J. Penfold, and A. H. Zewail, "*Ultrafast core-loss spectroscopy in fourdimensional electron microscopy*," *Structural dynamics*, vol. **2**, no. 024302, (2015).

[124] J.-A. Yang, S. Parham, D. Dessau, and D. Reznik, "*Novel Electron-Phonon Relaxation Pathway in Graphite Revealed by Time-Resolved Raman Scattering and Angle-Resolved Photoemission Spectroscopy*," *Scientific Reports*, vol. **7**, no. 40876, (2017).

[125] R. P. Chatelain, V. R. Morrison, B. L. M. Klarenaar, and B. J. Siwick, "*Coherent and Incoherent Electron-Phonon Coupling in Graphite Observed with Radio-Frequency Compressed Ultrafast Electron Diffraction*," *Physical Review Letters*, vol. **113**, no. 235502, (2014).

[126] S. L. Cousin, *Towards the Generation of Isolated Attosecond Pulses in the Water Window.* PhD Thesis, (2016).

[127] M. Nisoli, S. De Silvestri, and O. Svelto, "*Generation of high energy 10 fs pulses by a new pulse compression technique*," *Applied Physics Letters*, vol. **68**, no. 2793, (1996).

[128] B. E. Schmidt, A. D. Shiner, P. Lassonde, J. Kieffer, P. B. Corkum, D. M. Villeneuve, and F. Légaré, "*CEP stable 1.6 cycle laser pulses at 1.8 μm*," *Optics Express*, vol. **19**, no. 7, (2011).

[129] D. J. Kane and R. Trebino, "*Characterization of arbitrary femtosecond pulses using frequency-resolved optical gating*," *IEEE Journal of Quantum Electronics*, vol. **29**, pp. 571–579, (1993).

[130] B. Buades, *Attosecond X-ray absorption fine-structure spectroscopy in condensed matter.* PhD Thesis, (2018).

[131] S. M. Teichmann, *Ponderomotively scaled high harmonic generation for attoscience in the water window.* PhD Thesis, (2015).

[132] X. Zhao, S. Wang, W. Yu, H. Wei, and C. D. Lin, "*Metrology of time-domain soft X-ray attosecond pulses and re-evaluation of pulse durations of three recent experiments*," *arXiv:1905.09526*, (2019).

[133] M. Newville, "*Fundamentals of XAFS*," *Reviews in Mineralogy and Geochemistry*, vol. **78**, pp. 33–74, (2014).

[134] D. E. Sayerst, E. A. Sterntf, and F. Lytle, "*New Technique for Investigating Noncrystalline Structures: Fourier Analysis of the Extended X-Ray—Absorption Fine Structure*," *Physical Review Letters*, vol. **27**, pp. 1204–1207, (1971).

[135] G. Hähner, "*Near edge X-ray absorption fine structure spectroscopy as a tool to probe electronic and structural properties of thin organic films and liquids*," *Chemical Society Review*, vol. **35**, p. 1244–1255, (2006).

[136] A. Einstein, "*On a Heuristic Point of View about the Creation and Conversion of Light*," *Annalen der Physik*, vol. **17**, no. 132, (1905).

[137] K. Sauer, J. Yano, and V. K. Yachandra, "*X-ray spectroscopy of the photosynthetic oxygen-evolving complex*," *Coordination Chemistry Reviews*, vol. **252**, p. 318–335, (2008).

[138] H. Ade and H. Stoll, "*Near-edge X-ray absorption fine-structure microscopy of organic and magnetic materials*," *Nature Materials*, vol. **8**, p. 281–290, (2009).

[139] B. K. Teo and D. C. Joy, *EXAFS Spectroscopy.* Springer, (1981).

[140] G. P. Williams, "*A general review of synchrotron radiation, its uses and special technologies*," *Vacuum*, vol. **32**, no. 6, pp. 333–345, (1982).

[141] D. H. Bilderback, P. Elleaume, and E. Weckert, "*Review of third and next generation synchrotron light sources*," *Journal of Physics b: Atomic, Molecular and Optical Physics*, vol. **38**, no. 9, (2005).

[142] R. W. Schoenlein, S. Chattopadhyay, H. H. W. Chong, T. E. Glover, P. A. Heimann, C. V. Shank, A. A. Zholents, and M. S. Zolotorev, "*Generation of femtosecond pulses of synchrotron radiation*," *Science*, vol. **287**, pp. 2237–2240, (2000).

[143] P. G. O'Shea and H. P. Freund, "*Free-Electron Lasers: Status and Applications*," *Science*, vol. **292**, no. 5523, pp. 1853–1858, (2001).

[144] M. Harmand, R. Coffee, M. R. Bionta, M. Chollet, D. French, D. Zhu, D. M. Fritz, H. T. Lemke, N. Medvedev, B. Ziaja, S. Toleikis, and M. Cammarata, "*Achieving few-femtosecond time-sorting at hard X-ray free-electron lasers*," *Nature Photonics*, vol. **7**, pp. 215–218, (2013).

[145] N. Hartmann, G. Hartmann, R. Heider, M. S. Wagner, M. Ilchen, J. Buck, A. O. Lindahl, C. Benko, J. Grünert, J. Krzywinski, J. Liu, A. A. Lutman, T. Marinelli, A. Maxwell, A. A. Miahnahri, S. P. Moeller, M. Planas, J. Robinson, A. K. Kazansky, N. M. Kabachnik, J. Viefhaus, T. Feurer, R. Kienberger, R. N. Coffee, and W. Helml, "*Attosecond time–energy structure of X-ray free-electron laser pulses*," *Nature Photonics*, vol. **12**, pp. 215–220, (2018).

[146] O. Y. Gorobtsov, G. Mercurio, F. Capotondi, P. Skopintsev, S. Lazarev, I. A. Zaluzhnyy, M. B. Danailov, M. Dell'Angela, M. Manfredda, E. Pedersoli, L. Giannessi, M. Kiskinova, K. C. Prince, W. Wurth, and I. A. Vartanyants, "*Seeded X-ray free-electron laser generating radiation with laser statistical properties*," *Nature Communications*, vol. **9**, no. 4498, (2018).

[147] I. Nama, C. Minb, C. Kim, H. Yang, G. Kim, H. Heo, S. Kwon, S. H. Park, and H. Kang, "*Soft X-ray harmonic lasing self-seeded free electron laser at Pohang Accelerator Laboratory X-ray free electron laser*," *Applied Physics Letters*, vol. **112**, no. 213506, (2018).

[148] M. I., K. Witte, D. Grötzsch, M. Neitzel, S. Günther, J. Baumann, R. Jung, H. Stiel, B. Kanngiesser, and W. Sandner, "*High average power, highly brilliant laser-produced plasma source for soft X-ray spectroscopy*," *Review of Scientific Instruments*, vol. **86**(3), no. 035116, (2015).

[149] Lawrence Berkeley National Laboratory, "Center for x-ray optics." `http://henke.lbl.gov/`.

[150] B. Buades, D. Moonshiram, T. P. H. Sidiropoulos, I. León, P. Schmidt, I. Pi, N. Di Palo, S. L. Cousin, A. Picón, F. Koppens, and J. Jens Biegert,

"*Dispersive soft x-ray absorption fine-structure spectroscopy in graphite with an attosecond pulse*," *Optica*, vol. **5**, no. 5, pp. 502–506, (2018). doi: `10.1364/OPTICA.5.000502`.

[151] B. Ravel and M. Newville, "*ATHENA, ARTEMIS, HEPHAESTUS: data analysis for X-ray absorption spectroscopy using IFEFFIT*," *Journal of Synchrotron Radiation*, vol. **12**, pp. 537–541, (2005).

[152] J. J. Rehr, J. J. Kas, F. D. Vila, M. P. Prange, and K. Jorissen, "*Parameter-free calculations of X-ray spectra with FEFF9*," *Physical Chemistry Chemical Physics*, vol. **12**, no. 5503, (2010).

[153] R. A. Rosenberg, P. J. Love, and V. Rehn, "*Polarization-dependent C(K) near-edge x-ray-absorption fine structure of graphite*," *Physical Review B*, vol. **33**, (1986).

[154] R. Ahuja, P. A. Brühwiler, J. M. Wills, B. Johansson, N. Mårtensson, and O. Eriksson, "*Theoretical and experimental study of the graphite 1s x-ray absorption edges*," *Physical Review B*, vol. **54**, no. 14396, (1996).

[155] G. Comelli, J. Stöhr, W. Jark, and B. B. Pate, "*Extended x-ray-absorption fine-structure studies of diamond and graphite*," *Physical Review B*, vol. **37**, pp. 4383–4389, (1988).

[156] F. Sette, G. K. Wertheim, Y. Ma, G. Meigs, S. Modesti, and C. T. Chen, "*Lifetime and screening of the C 1s photoemission in graphite*," *Physical Review B*, vol. **41**, no. 14, (1990).

[157] P. A. Brühwiler, A. J. Maxwell, P. Rudolf, C. D. Gutleben, B. Wästberg, and N. Martensson, "*C 1s Autoionization Study of Electron Hopping Rates in Solid* C_{60}," *Physical Review Letters*, vol. **71**, no. 22, (1993).

[158] O. Bunau and Y. Joly, "*Self-consistent aspects of x-ray absorption calculations*," *Journal of Physics: Condensed Matter*, vol. **21**, no. 34, (2009).

[159] A. B. Djurišić and E. H. Li, "*Optical properties of graphite*," *Journal of Applied Physics*, vol. **85**, no. 7404, (1999).

[160] M. Uemoto, Y. Kuwabara, S. A. Sato, and K. Yabana, "*Nonlinear polarization evolution using time-dependent density functional theory*," *ACS Nano*, vol. **150**, no. 094101, (2019).

[161] M. Reduzzi, J. Hummert, A. Dubrouil, F. Calegari, M. Nisoli, F. Frassetto, L. Poletto, S. Chen, M. Wu, M. B. Gaarde, K. Schafer, and G. Sansone, "*Polarization control of absorption of virtual dressed states in helium*," *Physical Review A*, vol. **92**, no. 033408, (2015).

[162] A. Chew, N. Douguet, C. Cariker, J. Li, E. Lindroth, X. Ren, Y. Yin, L. Argenti, W. T. Hill III, and Z. Chang, "*Attosecond transient absorption spectrum of argon at the* $L_{2,3}$ *edge*," *Physical Review A*, vol. **97**, no. 031407(R), (2018).

[163] J. C. Gierz, I. Petersen, M. Mitrano, C. Cacho, I. C. E. Turcu, E. Springate, A. Stöhr, A. Köhler, U. Starke, and A. Cavalleri, "*Snapshots of non-equilibrium Dirac carrier distributions in graphene*," *Nature materials*, vol. **12**, (2013).

[164] T. Numai, *Fundamentals of Semiconductor Lasers.* Springer, (2015).

[165] S. Pagliara, G. Galimberti, S. Mor, M. Montagnese, G. Ferrini, M. S. Grandi, P. Galinetto, and F. Parmigiani, "*Photoinduced* $\pi - \pi^*$ *Band Gap Renormalization in Graphite*," *Journal of American Chemical Society*, vol. **133**, p. 6318–6322, (2011).

[166] L. Waldecker, R. Bertoni, R. Ernstorfer, and J. Vorberger, "*Electron-Phonon Coupling and Energy Flow in a Simple Metal beyond the Two-Temperature Approximation*," *Physical Review X*, vol. **6**, no. 021003, (2016).

[167] T. Vasileiadis, L. Waldecker, D. Foster, A. Da Silva, D. Zahn, R. Bertoni, R. E. Palmer, and R. Ernstorfer, "*Ultrafast Heat Flow in Heterostructures of Au Nanoclusters on Thin Films: Atomic Disorder Induced by Hot Electrons*," *ACS Nano*, vol. **12**, no. 8, pp. 7710–7720, (2018).

[168] G. R. Stewart, "*Measurement of low-temperature specific heat*," *Review of Scientific Instruments*, vol. **54**, no. 1, pp. 1–11, (1983).

[169] E. Pop, V. Varshney, and A. K. Roy, "*Thermal properties of graphene: Fundamentals and applications*," *MRS Bulletin*, vol. **37**, no. 12, pp. 1273–1281, (2012).

[170] W. A. Kutt, W. Albrecth, and H. Kurz, "*Generation of coherent phonons in condensed media*," *IEEE Journal of Quantum Electronics*, vol. **28**, no. 10, pp. 2434 – 2444, (1992).

[171] T. K. Cheng, J. Vidal, H. J. Zeiger, G. Dresselhaus, M. S. Dresselhaus, and E. P. Ippen, "*Mechanism for displacive excitation of coherent phonons in Sb, Bi, Te, and* Ti_2O_3," *Applied Physics Letters*, vol. **59**, no. 1923, (1991).

[172] Y. Liu, A. Frenkel, G. A. Garrett, J. F. Whitaker, S. Fahy, C. Uher, and R. Merlin, "*Impulsive Light Scattering by Coherent Phonons in* $LaAlO_3$*: Disorder and Boundary Effects*," *Physical Review Letters*, vol. **75**, no. 334, (1995).

[173] L. Dhar, J. A. Rogers, and K. A. Nelson, "*Time-resolved vibrational spectroscopy in the impulsive limit*," *Chemical Reviews*, vol. **94**, no. 1, pp. 157–193, (1994).

[174] M. Hase, M. Kitajima, A. M. Constantinescu, and H. Petek, "*The birth of a quasiparticle in silicon observed in time–frequency space*," *Nature*, vol. **426**, pp. 51–54, (2003).

[175] S. Hunsche, K. Wienecke, T. Dekorsy, and H. Kurz, "*Impulsive Softening of Coherent Phonons in Tellurium*," *Physical Review Letters*, vol. **75**, no. 9, (1995).

[176] M. Hase, M. Kitajima, S. Nakashima, and K. Mizoguchi, "*Dynamics of Coherent Anharmonic Phonons in Bismuth Using High Density Photoexcitation*," *Physical Review Letters*, vol. **88**, no. 6, (2002).

[177] E. S. Zijlstra, L. L. Tatarinova, and M. E. García, "*Laser-induced phonon-phonon interactions in bismuth*," *Physical Review B*, vol. **74**, no. 220301(R), (2006).

[178] M. Harb, R. Ernstorfer, C. T. Hebeisen, G. Sciaini, W. Peng, T. Dartigalongue, M. A. Eriksson, M. G. Lagally, S. G. Kruglik, and R. J. D. Miller, "*Electronically Driven Structure Changes of Si Captured by Femtosecond Electron Diffraction*," *Physical Review Letters*, vol. **100**, no. 155504, (2008).

[179] L. Waldecker, R. Bertoni, H. Hübener, T. Brumme, T. Vasileiadis, D. Zahn, A. Rubio, and R. Ernstorfer, "*Momentum-Resolved View of Electron-Phonon Coupling in Multilayer* WSe_2," *Physical Review Letters*, vol. **119**, no. 036803, (2017).

[180] M. E. Garcia, T. Dumitrica, and H. O. Jeschke, "*Coherent lattice vibration of interlayer shearing mode of graphite*," *Applied Physics A*, vol. **79**, p. 855–857, (2004).

[181] L. Waldecker, T. Vasileiadis, R. Bertoni, R. Ernstorfer, T. Zier, F. H. Valencia, M. E. Garcia, and E. S. Zijlstra, "*Coherent and incoherent structural dynamics in laser-excited antimony*," *Physical Review B*, vol. **95**, no. 054302, (2017).

[182] B. D. Bruner, M. Krüger, O. Pedatzur, G. Orenstein, D. Azoury, and N. Dudovich, "*Robust enhancement of high harmonic generation via attosecond control of ionization*," *Optics Express*, vol. **26**, no. 7, pp. 9310–9322, (2018).

[183] T. Kroh, C. Jin, P. Krogen, P. D. Keathley, A.-L. Calendron, J. P. Siqueira, H. Liang, E. L. Falcão-Filho, C. D. Lin, F. X. Kärtner, and K.-H. Hong, "*Enhanced high-harmonic generation up to the soft X-ray region driven by mid-infrared pulses mixed with their third harmonic*," *Optics Express*, vol. **26**, no. 13, pp. 16955–16969, (2018).

[184] P. Hosseini, A. Ermolov, F. Tani, D. Novoa, and P. S. J. Russell, "*UV Soliton Dynamics and Raman-Enhanced Supercontinuum Generation in Photonic Crystal Fiber*," *ACS Photonics*, vol. **5**, no. 6, pp. 2426–2430, (2018).

Abbreviations

3TM	Three-Temperature Model
ARPES	Angular-Resolved PhotoEmission Spectroscopy
AH	Auger Heating
APT	Attosecond Pulse Train
BBO	Beta Barium Borate
CB	Conduction Band
CCD	Charged-Coupled Device
CEP	Carrier-to-Envelope Phase
CPA	Chirped-Pulse Amplification
DECP	Displacive Excitation of Coherent Phonon
DFT	Density-Functional Theory
DOS	Density Of States
DT	Differential Transmission
EPC	Electron-Phonon Coupling
FEL	Free-Electron Laser
FROG	Frequency-Resolved Optical Gating
FROGCRAB	FROG for Complete Reconstruction of Attosecond Bursts
FWHM	Full-Width-Half-Maximum
EXAFS	Extended X-ray Absorption Fine Structure
FD	Fermi-Dirac
HCF	Hollow-Core Fiber
HOPG	Highly-Oriented Pyrolithic Graphite
HHG	High-Harmonic Generation
HHS	High-Harmonic Spectroscopy
IAP	Isolated Attosecond Pulses
ID	Inner Diameter
II	Impact Ionization
IR	InfraRed
ISRS	Impulsive Stimulated Raman Scattering

OPA	Optical Parametric Amplification
PCGPA	Principal Component Generalized Projection Algorithm
PROOF	Phase Retrieval by Omega Oscillation Filtering
RABBITT	Reconstruction of Attosecond Beating By Interference of Two-photon Transitions
SCOP	Strongly-Coupled Optical Phonon
SFG	Sum-Frequency Generation
SHG	Second-Harmonic Generation
SPM	Self-Phase Modulation
STFT	Short-Time Fourier Transform
SWIR	Short-Wavelength InfraRed
SXR	Soft X-Ray
TA	Transient Absorption
TD-DFT	Time-Dependent DFT
Ti:Sa	Titanium:Sapphire
TOF	Time-Of-Flight
UED	Ultrafast Electron Diffraction
VB	Valence Band
XAFS	X-ray Absorption Fine Structure
XANES	X-ray Absorption of Near Edge Structure
XUV	EXtreme Ultra-Violet
YAG	Yttrium - Aluminum - Garnet

Publications

Here is the list of publications related to the work carried out during my Ph.D. project.

- Seth L. Cousin, **Nicola Di Palo**, Bárbara Buades, Stephan M. Teichmann, Maurizio Reduzzi, Michele Devetta, Anatoli Kheifets, Giuseppe Sansone and Jens Biegert, "*Attosecond Streaking in the Water Window: A New Regime of Attosecond Pulse Characterization*", Physical Review X **7**, 041030 (2017)

- Bárbara Buades, Dooshaye Moonshiram, Themistoklis P. H. Sidiropoulos, Iker León, Peter Schmidt, Irina Pi, **Nicola Di Palo**, Seth L. Cousin, Antonio Picón, Frank Koppens, and Jens Biegert, "*Dispersive soft x-ray absorption fine-structure spectroscopy in graphite with an attosecond pulse*", Optica **5**, 5, 502-506 (2018)

- Bárbara Buades, Antonio Picón, Iker León, **Nicola Di Palo**, Seth L. Cousin, Caterina Cocchi, Eric Pellegrin, Javier Herrero Martin, Samuel Mañas-Valero, Eugenio Coronado, Thomas Danz, Claudia Draxl, Mitsuharu Uemoto, Kazuhiro Yabana, Martin Schultze, Simon Wall, Jens Biegert, "*Attosecond-resolved petahertz carrier motion in semi-metallic* TiS_2", arXiv:1808.06493, under review

- **Nicola Di Palo** et al., in preparation (This publication will contain the main results of time-resolved XAFS in graphite, reported in Chap. 4 of this thesis)

Author's contributions

The aim of this section is to highlight the author's contributions with respect to the different works presented in this thesis. The laser system providing CEP-stable, few-cycle infrared pulses was built by Dr. Seth L. Cousin (SC) and Dr. Michael Hemmer under the supervision of Prof. Dr. Jens Biegert (JB). The actual setup for the Attosecond Beamline is a slight modification of the original scheme designed by JB and realized by BesTec. The Mirror and the Experimental chambers preserve the original design, while the Spectrograph was rebuild by SC with the help of the author and Dr. Bárbara Buades (BB). The Generation and Differential Pumping chamber are instead a new design realized by Biplob Nandy and JB and then installed by the author and Dr. Themistoklis P. H. Sidiropoulos (TS).

The source characterization in terms of flux and stability as well as the study of the spectral tunability have been realized by the author with the help of TS, Dr. Daniel Rivas (DR) and Stefano Severino (SS). The collinear pump-probe setup was realized by SC and used for the Attosecond Streaking experiment. This experiment was carried out by SC with the help of BB and the author. The data analysis and interpretation contained in the final publication were performed by SC and the author together. The non-collinear setup, both for the $1.85\,\mu$m and $0.8\,\mu$m cases, were realized and characterized by the author with the help of TS, DR and SS.

The experimental data for the XAFS study of graphite were collected by BB with the help of Dr. Iker Leon, Irina Pi and the author. The data analysis providing information on both the electronic and the lattice structure was carried out by BB, Prof. Antonio Picón, TS and Dr. Dooshaye Moonshiram, while the sample was fabricated by Dr. Peter Schmidt. The samples used for the time-resolved XAFS campaign presented in this thesis were instead fabricated by Dr. Thomas Danz and characterized by XAFS analysis by the author with the help of SS, TS and DR. The XAFS measurements taken at ALBA synchrotron source were collected by Dr. Eric Pellegrin, Dr. Pierluigi Gargiani and Dr. Manuel Valdivares. For the numerical modeling of the XAFS spectra, the DFT calculations of the band structure and DOS were performed by JB, while the FDMNES simulations have been realized by TS with the help of the author and JB.

The experimental campaign for time-resolved XAFS in graphite presented in chap. 4 was led by the author with the help of TS, SS, DR and Dr. Maurizio Reduzzi. The general processing of the experimental data was done by the author and TS. The STFT results for the sub-cycle carrier dynamics were obtained by TS with the help of the author, while the DFT simulations were provided by Dr. Mitsuharu Uemoto and Prof. Kazuhiro Yabana. The analysis for the carrier multiplication, for the carrier lifetime and for the Fermi-Dirac fit was performed by the author with the help of TS. The three-temperature model was provided by Dr. Thomas Vasileiadis and Prof. Dr. Ralph Ernstorfer. The analysis of the coherent and incoherent excitation of phonons was realized by the author, supported by TS and JB (calculation of phonon band structure). The Fourier analysis to identify the different vibrational modes was performed by the author.